

NUMERICAL INVESTIGATION OF MICRO AND MACRO MECHANICAL BEHAVIOUR OF GRANULAR MEDIA VIA A DISCRETE ELEMENT APPROACH

Dissertation

zur Erlangung des akademischen Grades

**doctor rerum naturalium
(Dr. rer. nat.)**

Von **M.Sc. Pradip Kumar Roul**
geb. am 01.05.1978 in Balasore, India

genehmigt durch die Fakultät für Mathematik
der Otto-von-Guricke-Universität, Magdeburg

Gutachter:

Prof. Dr. Klaus Kassner
Prof. Dr. Gerald Warnecke

Eingereicht am: 26.05.2009
Verteidigung am: 10.07.2009

Zusammenfassung

Diese Arbeit ist ein Beitrag zum Verständnis der mechanischen Eigenschaften nichtkohäsiver granularer Materialien im statischen Grenzfall. Wir simulieren die Dynamik von Schüttgütern wie etwa Sand. Am mechanisch relaxierten Zustand der simulierten Sandhaufen messen wir numerisch Eigenschaften auf der Mikroskala. Dann führen wir Mittelungen durch, um die Werte von Feldgrößen zu erhalten, die in einer zu findenden makroskopischen Kontinuumsbeschreibung relevant sein mögen. Dabei wenden wir eine effiziente Modellierungstechnik an, die sogenannte Diskrete-Elemente-Methode (DEM). Insbesondere zeigen wir, dass es nicht nur möglich ist, elastische Spannungen im Sandhaufen zu bestimmen, sondern auch Verschiebungsfelder. Letzteres gelingt durch überlegten Einsatz eines adiabatischen Relaxationsprozesses, in dem die Gravitation, über die man in der Numerik ja frei verfügen kann, langsam variiert wird. Auf diese Weise steht nach der Simulation der vollständige Satz von Feldvariablen der Elastizitätstheorie zur Verfügung. Es ist zu betonen, dass Verschiebungs- und Deformationsfelder für Sandhaufen vorher in der Literatur nicht betrachtet wurden.

Konvergierte Werte makroskopischer Felder werden durch Mittelung über ein repräsentatives Volumenelement (RVE) berechnet, dessen Größe zu bestimmen war. Wir finden, dass für alle Felder ein RVE ausreichend ist, das 100-200 Teilchen enthält. Spannungstensoren werden sowohl für symmetrische als auch für asymmetrische Sandhaufen in zweidimensionalen Systemen untersucht. Dabei lassen wir die Teilchen entweder aus einer punktförmigen Quelle fallen oder aus einer Linienquelle, deren Länge sich im Lauf der Zeit verkürzt. Die aus den Simulationen erhaltenen gemittelten Spannungsverteilungen reproduzieren das experimentell beobachtete Druckminimum für aus einer Punktquelle aufgeschüttete Sandhaufen, während wir (ebenfalls in Übereinstimmung mit dem Experiment) kein vergleichbares Minimum für mit einer Linienquelle erzeugte Sandhaufen beobachten. Wir bestimmen die Massendichte in Sandhaufen, die entweder aus einer Punkt- oder Linienquelle geschüttet wurden und finden, dass die Dichte unter einem Haufen, der aus einer Punktquelle stammt, nicht homogen ist. Überraschenderweise *nimmt* die Dichte *zu*, wo der Druck *minimal* wird. Andererseits ist die Dichte unter einem aus einer Linienquelle stammenden Haufen homogen verteilt.

Im Weiteren werden effektive Materialeigenschaften von Sandhaufen aus konvexen polygonalen Teilchen durch numerische Simulation untersucht, wobei generell die zwei obengenannten Typen von Sandhaufen mit unterschiedlicher Konstruktionsgeschichte betrachtet werden. Die gemittelten Spannungs- und Deformationsfelder werden ebenso bestimmt (letztere durch Variation der Gravitation um 10%) wie der *Fabric*-Tensor (Strukturtensor) und das lokale Trägheitstensorfeld. Ziel dieser Simulationen war die Gewinnung detaillierter Informationen zur Gesamtheit der makroskopischen Materialeigenschaften granularer Medien, was unser Verständnis von Transport- und Prozessproblemen zu verbessern hilft, die in korpuskularen Materialien auftreten. Wir zeigen, wie die Konstruktionsgeschichte von Sandhaufen ihre Spannungs- und Deformationsverteilung sowie die Verteilung der lokalen Volumenanteile beeinflusst; wir zeigen auch, wie die Spannungsverteilung von der Formverteilung der Partikel abhängt. Die Absenkung in der Druckverteilung wird deutlich ausgeprägter, wenn der Sandhaufen

aus einer Mischung elliptischer Teilchen besteht als wenn er sich aus fast kreisrunden Partikeln zusammensetzt. Wir bestimmen den Deformationstensor auf mehrere verschiedene Weisen und vergleichen drei *Best-Fit*-Methoden aus der Literatur mit direkter numerischer Differentiation. Im Zentrum eines Sandhaufens liefern drei der vier Verfahren übereinstimmende Ergebnisse, an seinem Rand sind die *Best-Fit*-Methoden wie erwartet numerisch genauer als die numerische Differentiation.

Der Strukturtensor wird für Sandschüttungen aus einer Punktquelle bestimmt. Wir finden, dass die Kontaktdichte der Teilchen in Richtung auf die Mitte und die unteren Bereiche des Sandhaufens hin zunimmt, wohingegen sie in der Nähe seiner Oberfläche gering ist. Die Spur des Strukturensors ist für einen Sandhaufen aus monodispersen Teilchen gleich dem Produkt aus der mittleren Koordinationszahl und dem Volumenanteil, während eine solche einfache Faktorisierung für polydisperse Teilchenmischungen nicht gegeben ist.

Wir bestimmen die elastischen Konstanten im Innern eines Sandhaufens numerisch, wobei wir die Gültigkeit des Hooke'schen Gesetzes für die Beziehung zwischen inkrementellen Spannungs- und Deformationsänderungen annehmen. Wir etablieren dann eine Korrelation zwischen den elastischen Materialkonstanten und dem Strukturtensor. Der makroskopische Elastizitätsmodul des Sandhaufens ist eine Größenordnung kleiner als der für die Kräftebestimmung verwendete der individuellen Teilchen, was nahelegt, dass das Konzept elastischer Eigenschaften des Aggregats auch im theoretischen Grenzfall starrer Teilchen seine Gültigkeit nicht verliert. Wir finden, dass der Kompressionsmodul zum Zentrum des Haufens hin anwächst und in Richtung auf seine freie Oberfläche hin abnimmt, dass also sein innerer Bereich härter ist als das Gebiet nahe der Oberfläche. Wir stellen fest, dass der Kompressionsmodul des Sandhaufens eine lineare Funktion der Spur des Strukturensors ist. Wir bestimmen die Beziehung zwischen Invarianten des inkrementellen Spannungstensors und des inkrementellen Deformationstensors und beobachten, dass das Verhalten nichtlinear ist, was bedeutet, dass linearem elastischem Verhalten in der Nähe des Zentrums des Haufens nichtlineares in der Nähe seiner Oberfläche gegenübersteht. Letzteres kündigt den Übergang zu plastischem Verhalten in den Außenregionen des Sandhaufens an, eine schon in der Literatur von Cantelaube und Mitarbeitern postulierte Situation.

Ein Vergleich der Simulationsdaten mit einfachen analytischen Theorien, unter anderem dem Modell der orientierten Spannungs-Linearität (OSL) und einem elastoplastischen Kontinuumsmodell zeigt, dass diese Theorien bestimmte Mängel aufweisen. Die beim OSL-Modell von Cates et al. zur Schließung des elastomechanischen Gleichungssystems vorgeschlagenen Beziehungen führen entweder nicht zu einer guten Anpassung an die numerischen Daten oder sind unmotiviert. Vergleichbare und bessere Anpassung erreicht man mit dem elastoplastischen Modell von Cantelaube et al., allerdings sollte hier eine Anpassung gar nicht nötig sein, denn die Theorie enthält keine freien Parameter mehr.

Die zweite Klasse von Systemen, die in dieser Arbeit (neben Sandhaufen) betrachtet wird, sind statische rechteckige Schichten granularer Schüttungen. Wir bestimmen ihre mechanische Antwort auf eine kleine externe Last, die auf die Oberfläche des Systems einwirkt. Dies erlaubt Rückschlüsse auf den Typ der makroskopischen Gleichungen, die das mechanische Verhalten des Systems regeln. Gemittelte Spannungs- und Deformations-Antwort-Funktionen auf eine lokale Störkraft werden für eine Anzahl von

Bedingungen bestimmt, darunter verschiedene Packungsanordnungen und statische Reibungskoeffizienten. Die Abhängigkeit der Form der vertikalen Normalspannungsantwort von der Ordnung der granularen Packung wird sichtbar gemacht. Monodisperse Packungen runder Teilchen weisen einen Doppel-*Peak* unter dem Angriffspunkt der externen Kraft auf; ein solches Verhalten folgt aus hyperbolischen Kontinuumsgleichungen mit Spannungsförtpflanzung entlang bevorzugter Bahnen. Für bidisperse Packungen treten auch Doppelspitzen auf, diese sind allerdings deutlich weniger ausgeprägt, während es nur einen einzelnen *Peak* für Packungen aus irregulären pentagonalen Teilchen mit ihrer höheren Unordnung gibt. Ein qualitativer Vergleich dieses Antwortverhaltens mit experimentellen Resultaten von Junfei Geng et al. an photoelastischem Material belegt die gute Übereinstimmung der Simulationen mit diesen Experimenten. Ferner vergleichen wir die analytische Lösung für die vertikale Spannungskomponente eines isotropen elastischen halbunendlichen Mediums in zwei Dimensionen (dessen Kontinuumsgleichungen natürlich elliptisch sind) mit unseren numerischen Spannungsantworten für die Fälle einer glatten und einer rauen Unterlage. Wir finden vergleichbares Antwortverhalten für alle drei Fälle, hinreichend ungeordnete Systeme scheinen also elliptischen Gleichungen zu gehorchen.

Abstract

This work is a contribution to the understanding of mechanical properties of non-cohesive granular materials in the static limit. We simulate properties of the mechanically relaxed state of sand piles and perform numerical averages to obtain the values of field quantities pertinent to a continuum description adopting an efficient modelling technique the so-called discrete element method (DEM). In particular, we show that it is possible to obtain not only stresses but also displacements in the heap, by judicious use of an adiabatic relaxation procedure, in which gravity is slowly changed. Hence the full set of variables of the theory of elasticity is available. We emphasize that the displacement (strain) fields inside sand piles have not been previously considered in the literature. Averaging is made reproducible by introducing a representative volume element (RVE), the size of which we determine by careful measurements. Stress tensors are studied for both symmetric and asymmetric sand piles in two-dimensional systems, where the particles are dropped from a point source. The averaged stress distributions obtained from simulations reproduces the experimentally observed pressure minimum for sand piles poured from a point source, whereas, we do not observe a similar minimum for sand piles poured from a line source. We have also obtained densities in a sand pile constructed either from a point source or a line source. We find that the density distribution is not homogeneous under a pile that is constructed from a point source. A surprising finding is the behaviour of the material density in this kind of heap, which increases where the pressure is at a minimum. On the other hand, the density is distributed uniformly under a pile constructed from a line source.

Furthermore, the effective material properties of sand piles of soft convex polygonal particles are investigated by numerical simulation. Two types of sand piles are constructed by two different procedures. The averaged stress and strain, the latter via imposing a 10% reduction of gravity, as well as the fabric and inertia tensor have been obtained throughout the sand pile, in order to gain more detailed knowledge on overall macroscopic material properties of granular materials, which will help improve our understanding of transport and processing problems appearing in particulate materials. We show how the construction history of the piles affects their strain distributions, volume fractions, and the stress distributions; we also show how the latter is affected by the shape distribution of the grains. The “dip” in the pressure distribution becomes significantly more pronounced for a pile consisting of mixture of elliptic particles than a pile consisting of mixture of round particles. Strain tensor is determined by adopting three different versions of best-fit methods and a simple differentiation method by numerical investigation for both types of sand piles. The results of four different versions of strains obtained from DEM simulations are compared to each other.

The fabric tensor is determined for a pile poured from a point source. We find that the contact density increases towards the centre and towards the bottom and decreases towards the surface of the pile. The fabric is linearly proportional to the product of the volume fraction and the mean coordination number for a pile consisting of mono-disperse mixture of particles. We determine the elastic constants throughout a sand pile numerically assuming Hooke’s law to be valid in relating incremental stress and strain

tensors to each other. We then establish a correlation between the elastic material coefficients and the fabric tensor. We find that the simulated sand pile is softer around one order of magnitude than the individual particles indicating that the sand pile can be elastic even in the limit of rigid particles. We see that the bulk modulus increases towards the centre and decreases towards the free surface of piles, indicating that the inner region of the pile is much harder than the region closer to the surface. We observe that the bulk modulus of the sand pile is a linear function of the trace of the fabric tensor. We determine the relationship between invariants of the incremental stress and the incremental strain tensor, observing that the behaviour is nonlinear which means that we have linear elastic behaviour near the centre of the pile and nonlinear behaviour announcing the transition to plastic behaviour near the surface of the pile, the same behaviour was assumed by Cantelaube et al.

Comparison of simulation data with simple analytical theories including orientated stress linearity (OSL) model and an elasto-plastic continuum model for the macroscopic mechanical behaviour of a sand pile shows that these theories have certain deficiencies. The OSL closure relations proposed by Cates et al. seem unable to make a good fit with the numerical stress distributions under a pile. However, we obtain comparable or better quality from fits to the elasto-plastic model by Cantelaube et al.

The second class of systems considered here are static rectangular layers of granular assemblies. We determine their response to an applied external overload at the top surface of the system in order to gain information on the type of macroscopic equations governing the mechanical behaviour. Averaged stress and strain response functions to a local force perturbation have been evaluated under a variety of conditions including various packing orders and different static friction. The dependence of the shape of the vertical normal stress response function on the packing order of the granular aggregate is exhibited. Mono-disperse packings of round particles show double peak shapes underneath the point where the external force is applied, a behaviour predicted for hyperbolic continuum equations. For bi-disperse packings, double peaks are also present, but much less pronounced, whereas there is only single peak present packings of irregular pentagonal particles. Stress responses are compared qualitatively with experimental results by Junfei Geng et al. of photo elastic material. Our simulation results show good agreement with these experiments. We compared the analytic vertical normal stress solution of an isotropic linearly elastic semi-infinite medium in 2D with our numerical stress responses for both smooth and rough bottoms. We observe that the vertical stress response is qualitatively similar for the three different systems, sufficiently disordered systems hence seem to satisfy elliptic equations.

Acknowledgements

Firstly, I would like to thank and express my sincere and deep gratitude to my advisor, Prof. Dr. Klaus Kassner for giving me opportunity to work on this challenging field at Otto Von Guericke University, Magdeburg. I am so grateful for his invaluable support, motivation, and encouraging new ideas during my research work, without his continuous guidance this PhD work would not have been finished.

I would like to thank Prof. Gerald Warnecke who is secondary supervisor of this research work for spending his valuable time in simulating discussions and effective cooperation, and giving me valuable suggestions on the computational results illustrated in this PhD work.

I express my sincere thanks to Prof. Dr. Stefan Luding for his effective cooperation, motivation and simulating discussions during my PhD work.

I would also like to thank Prof. Jürgen Tomas for his valuable suggestions and fruitful discussions on the simulation methods used in this research work.

I wish to thank Dr. Stephan Mertens and Dr. Schulenburg for providing me for his cooperation in computing service and technical assistance.

I am so grateful to my parents for their supports throughout my study carriers without their unconditional affection. The special thanks goes to my wife Sabita for giving me moral encouragement and her patience during my PhD studies.

I would like to acknowledge the German Research Foundation (DFG) for providing financial support through the research program Graduiertenkolleg 828: Micro-Macro-interactions in structured media and particle systems.

Last but not the least, I would like to say my friendly thanks to all my colleagues who directly or indirectly helped me in my work.

Pradip Kumar Roul

Contents

Introduction	1
1 Granular materials	7
1.1 Fundamental characteristics of granular materials	7
1.2 Major mechanical properties of granular materials	9
1.2.1 Density distribution	9
1.2.2 Pressure distribution under a sand pile	12
1.2.3 Force distribution in granular media	16
1.3 Motivation	18
2 The simulation method	23
2.1 Why computer simulation are needed for granular materials	23
2.2 Different methods to simulate granular media	24
2.2.1 Discrete element method	27
2.2.1.1 Event-driven method	30
2.2.1.2 Time-driven method	31
2.3 Integration scheme	32
2.3.1 Gear Predictor-Corrector method	34
2.4 Force calculation	38
2.4.1 Normal force	38
2.4.2 Tangential force	41
2.5 Collision detection	44
2.6 Determining macroscopic quantities	45
2.6.1 Calculation of stress fields	46
2.6.2 Determining strains	50
2.6.2.1 Cambou's best-fit strain	53
2.6.2.2 Cundall's best-fit strain	56
2.6.2.3 The best-fit strain of Liao et al.	58
2.6.2.4 Derivative method	60
2.6.3 Inertia tensor field for assemblies of polygonal particles	61
2.6.3.1 Inertia tensor for a single particle	61
2.6.3.2 Averaged inertia tensor field	64

2.6.4 Fabric tensor	65
2.6.4.1 The fabric tensor for one particle	65
2.6.4.2 Fabric tensor for single particle	67
2.7 Averaging procedure	67
3 Simulation results	71
3.1 Method of preparation of the sand pile	71
3.1.1 Sand piles from a point source	73
3.1.2 Sand piles from a line source	73
3.2 Microscopic force distribution	76
3.3 Pressure distribution under a sand pile	79
3.4 Volume fractions	82
3.5 Orientation of the particles in sand piles	84
3.6 Strain distribution under sand piles	86
3.6.1 Comparison of strain tensor	89
3.7 Properties of the fabric tensor	90
3.8 Distribution of stress and strain invariant	95
3.9 Coordination number for different changes in gravitation	96
3.10 Determination of elastic constants	97
3.11 Stress distribution for asymmetric sand pile	103
4 Comparison between simulation and analytic theory	109
4.1 Analytical approaches for sand piles	109
4.2 Basic law of mechanical equilibrium	111
4.3 Elasto-plastic continuum model	113
4.4 Orientated stress linearity model	121
5 Stress response of a static rectangular layer of a granular material	129
5.1 Simulation geometry	131
5.2 Contact force angle distribution	134
5.3 Simulation results of stress responses for different packings	135
5.4 Stress response for different values of the friction coefficient	137
5.5 Stress response for poly-disperse packing	141
5.6 Comparison between numerical stress responses and an analytic solution	143
5.7 Strain response for mono-disperse packings	145
5.8 Conclusions	145
6 Conclusions & outlook	147



Introduction

Granular materials are of fundamental importance and high interest to various branches of science and technology such as physics, applied mathematics and mechanics. In the last few years, extensive research has been devoted to the study of granular materials due to their importance for applications in various industries and because they pose fundamental analytical challenges [1-2]. Moreover, the understanding how granular materials response to an applied overload is an interesting and difficult scientific problem in recent years. Granular materials are commercially very important for application in pharmaceutical industry, agricultural, geotechnical industry, and energy production industry.

Currently, a large amount of money is spent on the transportation and processing associated with the storage and containment of granular materials. However, about 50% of the money is unnecessarily spent because of problems related to the transport of the material from one part of the factory to another part of the factory.

Now, to have a look from another angle, it is often assumed that the side wall of a material container receives a constant force from the granular material inside. The common example of this issue is a model of a silo which is of great concern to various industries such as agricultural, pharmaceutical and mining industries, and all construction-based industries. However, this assumption is wrong, and in the general case, forces are non-uniformly propagated within the material, so they are also non-uniformly distributed at the wall of the silo. In some cases, if the force is much larger in some parts of the container than in other parts, the silo might collapse. For in order to avoid problems such as the collapse or breach of a silo, one can simply increase the thickness of the walls by a generously chosen safety margin, which would be unnecessary

if we had the knowledge how to design the silo in a proper way, especially taking into account the expected distribution of forces inside the silo. Therefore, the understanding of the basic physical principles behind the stress distribution in static granular materials is clearly important.

A simple example out of a collection of granular arrangements is the static sand pile. The formation of a sand pile is related to the fundamental behaviour of granular materials, including particle packing, segregation and pressure distribution. The practice of storing granular materials in the form of sand piles occurs in many industrial situations dealing with particulate materials. Examples include the pharmaceutical industry relying on the processing of powders and tablets, the agricultural industry, coal industry and the food processing industries where seeds, coal (grain) and foods are transported and manipulated. Moreover, the storing of the material in a pile may be useful in fertilizer and mining industries. Thus, the flow of granular materials through a funnel (to form a pile) is an important problem for many industrial processes.

In order to handle the processing of granular materials in a pile properly, it is important to understand its mechanical properties and effective material behavior. On the other hand, the study of deformation of granular materials either under external loading or unloading is also of practical importance for many industries. Although some progress has been made in this field during last ten years, these properties are still far from being exhaustively understood. Moreover, continuum models proposing constitutive relations to describe the flow and the deformation of granular materials have remained important, these constitutive relations are not able to completely describe the behaviour of granular materials.

In spite of their importance in applications, it is fair to say that there is as yet no fundamental understanding of granular materials. Such an understanding might manifest itself in a general continuum theory, applicable to the majority of granular assemblies, without the need of ad hoc assumptions for each new system considered. Even though continuum descriptions have been applied extensively to model granular materials, especially in the engineering community [3-4], neither are these based on a microscopic theory nor is their predictive power for new experiments on granulates impressive. In the physics community, continuum descriptions are based either on balance equations [5] or on symmetry considerations [6], i.e., on general principles that are not specific to the granular state, so these ideas may yield important constraints for a microscopic theory but cannot stand in its place. For static assemblies, phenomenological closure relations [1] as well as elasto-plastic models [2] have been used in macro scale calculations of the stress tensor, leading to different stress distributions in a sand pile.

The goal of this work is to numerically investigate the mechanical, physical properties and effective material behaviour of static two dimensional sand piles consisting of poly-disperse mixture of soft convex polygonal particles, using an efficient numerical method the so-called “discrete element method (DEM)”. In this work, we construct two types of sand piles by two different procedures. In order to compute the trajectory and rotational motion of each individual particles inside the sand pile we solve Newton’s and Euler’s

equations of motion involving the forces and the torques acting on each particles, using a fifth-order Gear predictor-corrector method. Magnitude, direction, and point of application of the microscopic forces are determined from the area and contact length of the overlap and from the relative velocities of two colliding particles. The calculation involves phenomenological elastic constants as well as model parameters for friction and viscous damping.

We determine primarily the microscopic tensorial quantities throughout the sand pile. Since microscopic tensorial quantities are not convenient to describe macroscopic properties of a sand pile we determine averages over many particles to obtain macroscopic field quantities to overcome this issue. Averages are performed over representative volume elements (RVE) that are then used to define macroscopic fields. The size of the RVE is determined from the requirement to obtain convergent results. The averaged volume fractions (densities) and stresses are determined numerically for piles with varying construction history of the piles; we also determine the latter for a pile constructed from a point source with different shapes of the grain. The results of stress tensor and densities obtained from simulations are compared with the existing experimental results [10, 11]. We note that, up to now, stresses have been measured experimentally, numerically and theoretically for symmetric sand piles. However, a review of literature shows that there has not been measured the stresses for an asymmetric sand pile. We focus on determining the stresses by numerical investigation for an asymmetric sand pile that constructed either from a point source or a line source. There are two macroscopic approaches [1, 2] in the literature based on analytical descriptions for describing the stress tensor under a sand pile the quality of which we check with our simulations.

The strain fields for a sand pile have not been considered in the literature. It is, therefore, the objective of this work to determine the strains, which will allow us for predicting the elastic material properties and elasto-plastic behaviour of a sand pile. In addition, we show how the vertical normal strain is influenced by the construction history of the piles. We use four different types of approaches including Cambou et al. [115], Liao et al. [116], Cundall et al. [76] and simple differentiation method to determine strains for both types of sand piles. Furthermore, we determine the relationship between invariants of the incremental stress and the incremental strain tensors for a small change in gravity.

Moreover, in order to study the internal structure of an assembly of grains, we determine numerically the fabric tensor inside the pile consisting of either mono-disperse mixture of particles or poly-disperse mixture of particles. We establish correlations between the fabric tensor and product of the volume fraction and mean coordination number, and between the fabric tensor and the measured elastic constants of the piles. A local inertia tensor of particles in the sand pile is introduced in order to determine an orientation field of the particles. The knowledge gained in studying the results of numerical simulations for sand piles is of major importance in understanding these handling and transporting issues.

The second class of granular systems considered in this work is concerned with the numerical investigation of stress and strain response to an applied external overload to a single grain (point force) at the top surface of the static rectangular layers of granular materials under a variety of packing orders, different static friction as well as different magnitude of the external overloads. The aim of this study is to decide the nature of the continuum equations for describing the macroscopic behaviour. The vertical normal stress responses to a point force of rectangular layers of granular materials with varying degrees of packing order obtained from our simulation are compared qualitatively with the existing experimental results of ref. [131]. Moreover, we perform a quantitative comparison between simulation data on the stress response at the bottom of the rectangular system and analytical results on stress response for a semi-infinite medium in the frame work of isotropic elasticity.

The thesis is organized in the following way:

After the introduction we start with Chapter 1 by presenting the fundamental characteristics of the granular materials. Then, we present a literature survey on the major mechanical properties of granular materials including pressure, packing density, and force distribution inside the sand pile, results obtained either by experimentally or numerically or theoretically from the literature. Then we discuss the motivation of the thesis work.

In Chapter 2, we are concerned with modelling and description of the behaviour of granular materials. Various numerical simulation methods and continuum mechanical methods are discussed for the simulation of granular materials. In our work, we used a discrete element method (DEM) simulation which essentially is a molecular dynamic (MD) simulation method modified to take into account the specificity of granular matter. Then we discuss in detail why this simulation method was chosen and how this method works in comparison to other simulation techniques. The basic structure and the algorithms of the DEM simulation are explained. Next, we discuss various numerical integration schemes in order to solve the equation of motion of the particles. In addition, we give a detailed description of the microscopic approach (force law), discussing in particular how the forces including both normal component and tangential components are calculated from the geometry of the overlap between two particles. Then we derive a formula for the macroscopic stress tensor as well as for the strain tensor, later using various best-fit approaches and general differentiation methods. How we deform the sand pile by reducing gravity focus on displacing the particle centre slightly, and why we use the incremental stress and strain tensors for the calculation of elastic material constants throughout the sand pile is then explained in detail. Next, we introduce a formula for the fabric tensor of polygonal particles and average over many particles, which will enable us to determine the internal texture of the sand pile. We then derive a formula for the inertia tensor of polygonal particles in the sand pile. How to derive various averaged macroscopic quantities from the microscopic quantities of the individual grains over a representative volume element (RVE) will be explained in detail.

In Chapter 3, results obtained from discrete element simulations for two-dimensional sand piles of soft convex polygonal particles are discussed. To begin with we show

results on the force distribution for different types of sand piles. Then we present DEM simulation results for averaged vertical normal stresses and averaged vertical normal strains at different heights inside a sand pile poured from a point source and from a line source. Furthermore, we compare the results of vertical normal stress tensor from sand piles consisting of roundish particles with those from sand piles consisting of elliptic particles. The averaged density was measured throughout the sand pile for both types of sand piles. Then the simulation results for the stress tensor and density distribution inside the sand piles are compared to the existing experimental results. In the next subsection of this chapter, strains are obtained by adopting various best fit methods and a differentiation method, to quantitatively compare the results between the different approaches. We then discuss the various properties of the fabric tensor of polygonal particles including the correlation between the trace of the averaged fabric tensor and the product of the volume fraction and mean coordination number for sand piles consisting of either mono-disperse or poly-disperse mixtures of the particles. Once we have the stress and strain tensors, we determine the elastic constants assuming Hooke's law. The simulation results for elastic constants of the sand piles that are poured from a point source are illustrated and we then establish a correlation between elastic constants and fabric tensor. In the next step, the simulation results for the orientation of particles inside a sand pile are presented. We also determine the correlations between the invariants of incremental stress tensors and incremental strain tensors. The chapter closes with a very interesting and exciting work done by evaluating numerically the stress tensor for asymmetric sand piles constructed with the two methods and comparing the numerical data with the existing analytical predictions.

Chapter 4 is devoted to analytical approaches for a stress distribution under a wedge-shaped pile. We first discuss two major continuum models including an elasto-plastic model proposed by Cantelaube et al. [2] and the orientated stress linearity (OSL) model by Wittmer et al. [1]. Then, in order to check the predictions of those theories, we compare our numerical simulation results of the stress tensor with their results.

In Chapter 5, we focus on the sensitivity of the stress response and the strain response to an applied external force at the top surface of rectangular systems of particles. The main aim of this study was to investigate numerically, how the granular materials respond to a point force. We first describe the simulation procedure, simulation parameters, and how the rectangular layer in two dimensional systems is constructed. Four different types of samples (rectangular systems) are constructed using mono-disperse particles, bi-disperse mixtures, pentagonal particles and poly-disperse mixtures of the particles. Then, we determine the angular distribution of all contact force for the different packings. In the next step, we present simulation results for stress response of the resulting rectangular system for various packing orders, including a qualitative comparison with experimental results. The stress response for the packing with different values of static friction and different values of applied external overload is discussed. Next, the simulation results on the stress response of a poly disperse system with either a smooth bottom or a rough bottom are presented and we then compare the numerical results with the existing experimental results. Then, we compare our numerical data on the stress response at the bottom of the system with analytical results on stress response for a semi-

infinite medium. Finally, the calculation of macroscopically averaged strain responses functions inside the granular aggregates consisting of mono-disperse particles is presented.

Chapter 6 presents the conclusions of the thesis and an outlook on future the work.

1

Granular materials

1.1 Fundamental characteristics of granular materials

Granular materials are ubiquitous in nature. They are systems consisting of a collection of a large number of macroscopic particles of variable size, shape and material. One classification scheme is based on the size of the particles, see Table 1. The lower size limit for granular particles in typical granular materials is about one micrometer. Below, the character of the force laws between the particle changes, adhesion may become much more important. The large-size limit goes well beyond the centimeter range on earth. In outer space, granular assemblies with much large particles exist. The ring of Saturn consists of dust, ice chunks, and lumps of rock with particle sizes ranging from the submillimeter to the meter scale.

Most of the time we handle granular materials in our every day life. Examples of such granular materials would include nuts, corn flakes, sugar, coffee powder, rice, small seed, powder grain and pills. Another examples are sand grains which are ubiquitous in our daily lives and play an important role in various industries such as mining, agriculture and civil engineering. Clearly they are also important for geological processes.

Granular material may exhibit different behaviour, sometimes resembling solids, in other cases liquids or gases. These behaviours depend on the average energy of the individual grains and the nature of the contact between the particles. If the average energy of the individual grains is very low and the grains are stationary relative to each other, then the material behaves like a solid. When energy is fed into the system such that the particles are not in constant contact to each other, the granular materials is said to be fluidized. If

the contacts between the grains become highly infrequent, then the assembly behaves like a gaseous state. The elementary units of granular materials are solid “mesoscopic” grains. Typical particle interactions in granular media include collisions and adhesive forces; occasionally, dusts get charged electrically, so there are electrostatic situations between particles in this case. This particle of long-range interactions has not been studied in much detail so far, here, we will restrict ourselves to short-range interactions as well. The only long-range force present in this study is gravitation, which is not an interaction between particles.

Size range	Individual grain
1.0 μm -10 μm	Super fine particle
10 μm -100 μm	Powder
100 μm -4.0 mm	Sand grain (Granule)
4 mm-60 mm	Gravel
60 mm-150 mm	Stone

Table 1: Types of granular material with different particle size range



Figure 1.1: Examples of non-spherical shapes of granular materials.

In granular media, we can define an intimate connection between the mechanical or physical properties on all three length scales such as microscopic, mesoscopic, and macroscopic scale. On the microscopic scale, the properties that characterize each individual grain of the material are their mass, velocity, shape, etc. On the mesoscopic scale, we consider the properties that characterize the multi-body nature of granulate, at least two particles. At this scale, we have to introduce the particle-particle interaction

forces and conservation laws. On the next scale, the macroscopic one, we consider the properties that characterize a bulk of particles of the material, examples include the stresses, strains, fabric, Young's modulus of elasticity, and bulk density of the material.

1.2 Major mechanical properties of granular materials

In this section, a short overview over the wide variety of observable phenomena for granular materials in the presence of friction is given. We handle different shapes of grain in our daily lives (spherical, non-spherical shape, elongated non-spherical), but in most practical situations, particles are mainly elongated non-spherical. Examples of such elongated non spherical shape of granulate would include rice, wheat, fertilizer and sand grain, etc. shown in Fig. 1.1. Following are the major properties of the granular materials which will be discussed briefly in the subsections

- Density distribution,
- Pressure distribution,
- Force distribution.

The properties of granular materials are strongly affected by the construction history of the aggregate and the characteristics of granulate, especially the size distribution and shape of the particles, which will be described in the following.

1.2.1 Density distribution

One of the major properties of granular material is the density distribution (packing density) which is defined as the local volume fraction of the granular material. The packing density is also very important in chemical industry, science, soil mechanics, concrete production etc. Moreover, measuring the volume fraction for a sand pile is important for us to compare our numerical simulation results of stress distribution with those of analytical stress distribution under a sand pile [1-2].

The bulk density of a granular material depends on the way the particles are packed. In some cases, the bulk density exhibits a homogeneous distribution under the heap, in others, it is inhomogeneous. Moreover, if the material is submitted to soft vibrations, the volume fraction, defined as the ratio of the volume of the particles to the total packing volume, increases.

The packing density is influenced by the shape, size distribution of the particles and construction history of granular materials. If a granular heap is constructed from the rainy

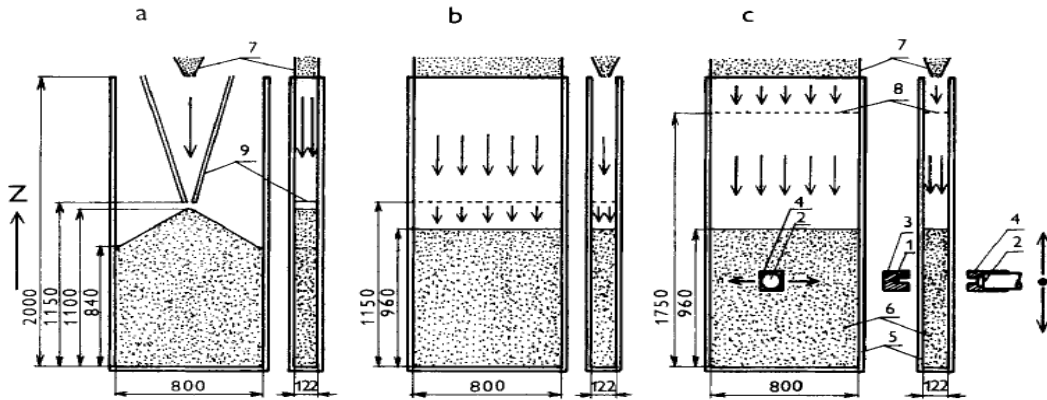


Figure 1.2: Filling methods of a packing of catalyst bed: a) point source; b) “rainy” filling with distributor in low position; c) “rainy” filling with distributor in high position [7].

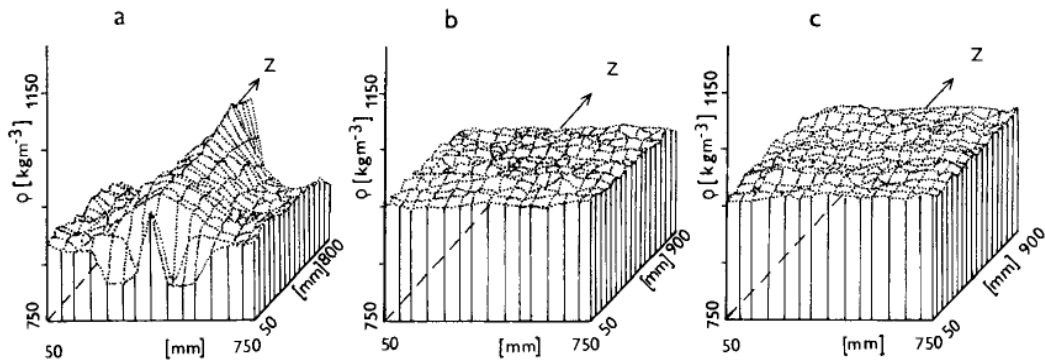


Figure 1.3: Density distribution in a packed bed for different pouring methods [7].

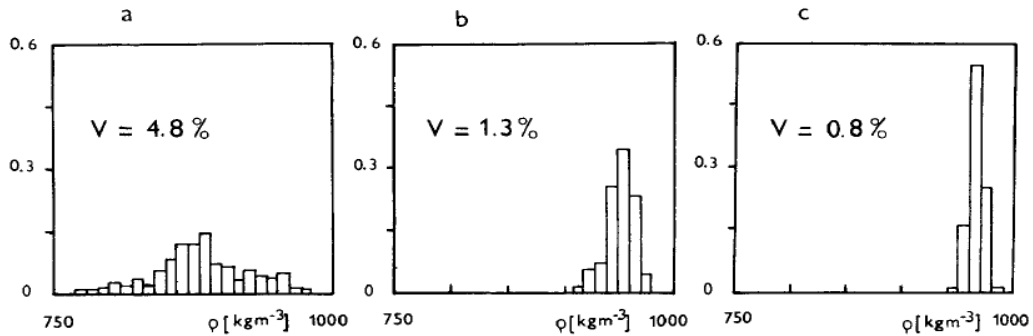


Figure 1.4: Histogram of density distribution of packed catalyst bed [7].

(uniform) filling method, there is a homogeneous density distribution at every location of the heap, if it is constructed from a point source then there is an in-homogeneous density distribution. The effect of the construction method on the bulk density distribution under a granular heap in two dimensions was verified experimentally in ref. [7]. In this experimental work, the bulk density of a catalyst bed was measured by radio gauging method, where the catalyst particles were poured into the system in three different ways as shown in Fig. 1.2. In the first method of the pouring processes, particles were poured from a certain height that formed a conical heap with a characteristic angle of repose. In the other two methods, so-called “raining filling” was realized with horizontal layers which were implemented with a spatial distributing grid, located either close to the bed surface or higher up. The density distribution results in two dimensions of catalyst bed are illustrated in Fig. 1.3 for the different construction histories of the granular aggregates and the histogram of the relative counts of these bulk densities are presented in Fig. 1.4. It can be observed from Fig. 1.4.a that there occur inhomogeneous density distribution with about 4.8% deviation in the point source method and it is about of 1.3% deviation as in Fig. 1.4.b for the rainy method with the distributor in a closer position, whereas the rainy method with a distributor in a higher position produces a relatively homogeneous distribution with only about 0.8% deviation as in Fig. 1.4.c.

In addition, packing density of poly-disperse granular material has been measured both experimentally and analytically using the solid suspension model proposed by De Garrard in Ref. [8] in order to verify the influence of shape and size distribution of the particles on the density distribution of the granular materials.

The first step of this study was to determine analytically the packing density of industrial material made of organic poly-disperse mixtures of particles using the solid suspension model. The size of the particles is uniformly distributed from 0.05 to 500 μm . The packing density for the industrial material was found 0.855. How the packing density is determined for the poly-disperse mixtures of granular materials using the analytical expression proposed by De Garrard has been explained in detail in ref. [8].

Moreover, experiments have been made on quasi mono-disperse materials. The aim of the experiments was to determine the experimental standard deviation of the packing density of the industrial material. Three simple quasi mono-disperse materials with different shapes and size of particles were used in these experiments as follows

- A. A packing containing glass spheres with a mean diameter of 500 μm .
- B. A packing containing glass spheres with a mean diameter of 50 μm .
- C. A packing containing acrylic spheres with a mean diameter of 500 μm .

In the experiment, the materials were deposited into the system with soft vertical vibration of the container. The size distribution of the particles of each material split into 8 to 12 classes for packing A to C.

From the analytical determination, it is noted that, the packing densities of 0.661, 0.674 and 0.670 were found, respectively for the packings A, B and C, whereas, $(66.1 \pm 1.9) \times 10^{-2}$, $(67.4 \pm 2.0) \times 10^{-2}$, $(67.0 \pm 1.9) \times 10^{-2}$ and $(85.5 \pm 3) \times 10^{-2}$ were found A,B,C and industrial material, respectively, from the experimental measurement of standard deviation of packing density.

1.2.2 Pressure distribution under a sand pile

One of the most interesting features of assemblies of grains in the static limit is the vertical normal stress distribution (pressure) under it. From the Janssen's analytical model in ref. [9], one could realize that, the pressure distribution in a silo filled with grains does not increase linearly with height, but saturates at a certain height, that means the pressure does not change anymore, once a certain distance from the surface of the filling is exceeded. A heuristic explanation of the physical mechanism producing such a phenomenon in a silo is that due to the internal friction of the aggregate of the granular material which leads to the arching phenomenon and due to the friction with the side walls, the latter support some part of the weight of the material. This will lead to a constant pressure below a certain depth in the silo. Related phenomena influence the pressure distribution in a sand pile, although we have no side walls of the system in this case.

When sand is piled up to build a heap, the pressure distribution under the final sand cone does not normally correspond to what one would expect from simple ideas about elasticity of a continuum. In some cases, pressure exhibits a large dip (local minimum) near the centre of the sand pile, in others, it either has a small minimum or no minimum at all, as a schematic diagram of some of the possible pressure distributions below the apex of a sand pile shows in Fig.1.5. The results depend strongly on the characteristics of the granulates, especially the size and shape distribution of the particles.

Moreover, with the same material, the construction history of the sand pile plays a crucial role in determining the distribution of stress under the sand pile. If the material is dropped from above a single position of the plane on which the pile is built (point source), there is a pressure minimum, if it is dropped layer-wise (line source), then there is no minimum. These results have first been found experimentally (see for example ref. [10]). The right top corner of Fig.1.6 shows a sand pile that has been constructed from a point source, whereas, the bottom sand pile was constructed from a line source. The pressure distribution of the corresponding sand pile measured from the centre to the right hand side of the pile is displayed in the left hand side of the same figure. The figure demonstrates the existence of a dip (local minimum) in the pressure profile at the centre for the case of a sand pile that was created from a point source, whereas there is no such

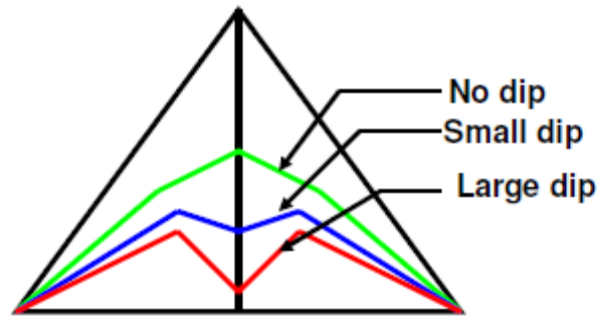


Figure 1.5: Schematic diagram of pressure distributions under a sand pile. Distributions of this type are expected when the inner and outer regions of the sand pile have different elastic behaviours.

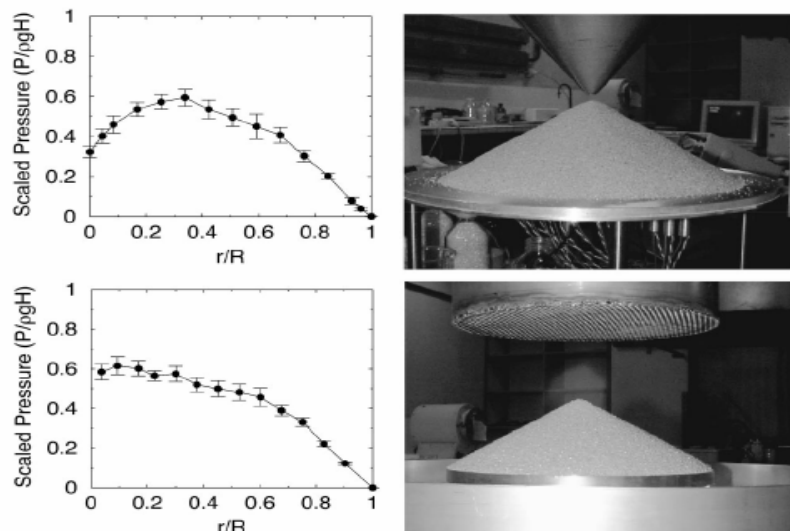


Figure 1.6: Experiments on sand pile, L.Vanel.et.al. [10].

minimum for the case of a sand pile that created from a line source. So we observe that two piles consisting of the same material may have different pressure distributions.

On the other hand, in some cases, the stress displays a large minimum below the apex of the sand pile and in others it has a small minimum, observed experimentally by I. Zuriguel and coworkers, in ref. [11]. The result depends upon the shape of the particles. If the sand piles contain a mixture of ellipsoidal particles, there is a large stress dip below the apex of the pile for a certain construction history of the pile, whereas when it contains a mixture of roundish particles, there is a much smaller dip, as is illustrated in Fig. 1.7.

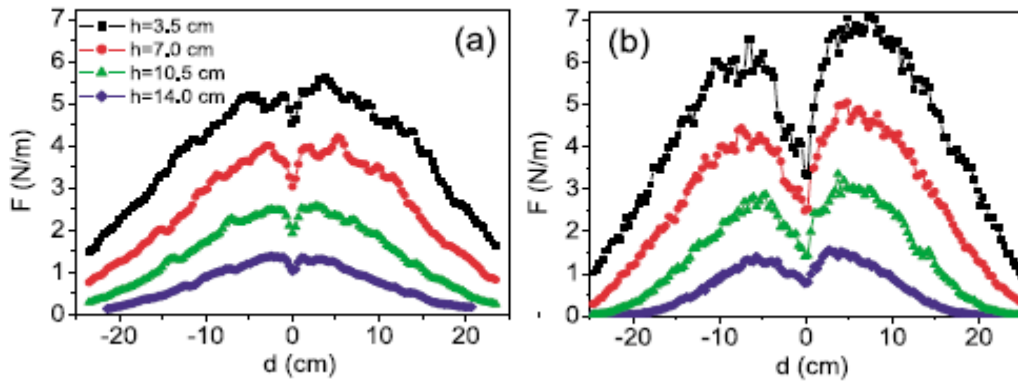


Figure 1.7: Experimental measurement of pressure distribution under a sand pile [11]. **Left:** shows the pressure distribution for a sand pile consisting of a mixture of disks, **Right:** shows the same for a sand pile consisting of mixture of elliptic particles.

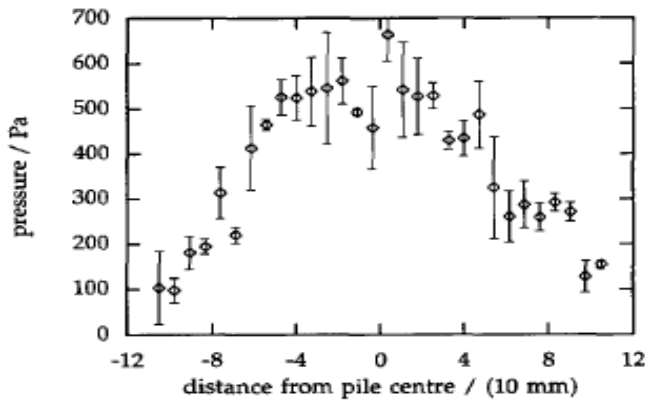


Figure 1.8: Experimental pressure distributions under a sand pile consisting of a mixture of large frosted smooth glass beads [12].

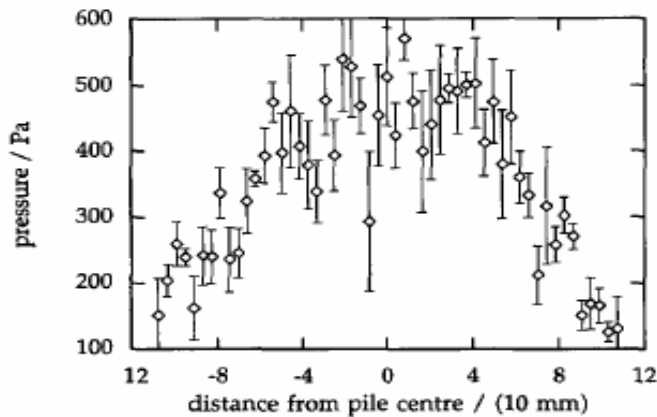


Figure 1.9 Experimental pressure distribution under a sand pile consisting of a mixture of large smooth glass beads [12].

Another mechanism is the roughness of the particles, that influences the pressure distribution under the sand pile. This has been observed in experimental measurements involving frosted (rough) glass beads in ref. [12] with size of 0.56 mm. A dip can be seen in the pressure profile as shown in Fig.1.8 obtained from the experiments with frosted glass beads, whereas, no dip occurs for a sand pile that contains a mixture of smooth glass beads with same particle size as one can see in Fig.1.9. The flow ability of the particles is supposed to be responsible for the existence of the dip, because reordering for frosted glass beads is more difficult than for the smooth glass beads.

Several years ago, the phenomenon indicated above produced a lot of excitement in the physics community involved in granular research and incited people to propose more or less fundamental theories.

A dip in pressure profile is not only seen in the experiments on sand piles, but also has been predicted in the continuum models tailored for that purpose. There exist many constitutive relations in the literature proposed by different researchers which may lead to a pressure dip in the centre of the heap. One of the interesting continuum approaches is the FPA (fixed principal axis) model obtained by Wittmer et al. [13], assuming a constitutive relation assuming that the major principal axis of the stress tensor of the granular heap is fixed at the time of the burial of a grain under the next layer of material and not affected by subsequent loading. This theoretical model provides an analytical stress tensor which is in decent agreement with the experimental data of three-dimensional sand piles, see ref. [14] and shows a pronounced pressure dip under the apex of the sand heap. Another theoretical model was obtained by F. Cantelaube et al. in ref. [15], who introduced an elasto-plastic continuum model that seems fully capable of exhibiting a pressure dip.

The phenomenon of the “dip under the heap” has fascinated physicists. On the other hand, among engineers there was a tendency to discard it as an isolated phenomenon without particular significance, for which many different explanations may be found, and which is probably due to different reasons in different experimental situations. One trivial explanation would be that the plate onto which the sand is poured bends downward during the process, which would immediately reduce the pressure in the centre, providing only that the sand does not follow this movement without resistance. While this explanation may hold for some experiments, there have been careful studies in the meantime with very thick ground plates in refs. [10, 12, 14, 16-17], for which such an effect can essentially be excluded and which still lead to a pressure minimum.

Also the pressure minimum can be seen in numerical simulations [18-26] of two dimensional sand wedges and three dimensional sand cones, including sand piles consisting of polygonal or spherical particles. There it can hardly be argued that it is due to a bending ground plate, as the numerical particles as well as the ground on which they fall do not change shape.

1.2.3 Force distribution in granular media

In granular media, the transmissions of forces occur from one particle to another only via contacts of the particles. Hence, the distribution of contacts will have an important influence on the distribution of forces within the assemblies of grains. The force transmission in granular media is important in many situations including silo design, foundation building as well as for the constructions of roads and dams. Therefore, the understanding of the basic physical principles behind the distribution of forces in stationary granular materials is very important.

Various models have been proposed by many researchers [27-36] to determine the structure of the force network and the probability distribution of forces inside of granular media. As it is stated in the literature [27-36], the behaviour of the probability distribution of normal forces inside a granular medium is not similar for all cases. There have been predictions of different types of normal force distribution inside the granular medium including an exponential, power law, Gaussian, and uniform distribution. For example, a theoretical scalar model called 'q model' was proposed by Liu et al. [27] and Coppersmith et al. [28], and Nguyen et al. [29], for determining the probability distribution of the contact normal force in granular materials. Coppersmith and coworkers [28] used the q model to determine the force inhomogeneities in stationary bead packs and predicted the probability distribution of forces decay at large forces for all most all contact distributions. They observed that the fluctuations in the distribution of force arise due to the variations in the contact angles and the constraints imposed by the force balance on each bead of the pile. Socolar [30] proposed a scalar model, the so-called α model, which is an improved version of q model, and found that for a two dimensional system of non-cohesive granular materials with periodic boundary condition, the force distribution is similar to the one obtained in the q model. However, Sexon et al. [31] proposed another scalar model studying intergrain forces in static and non-cohesive granular materials, and predicted the probability distribution for forces on individual grains to appear as Gaussian at all stages of compression and to show no evidence of an exponential tail, present in the q model.

Better understanding of the distribution of forces inside a granular material has been obtained not only using the theoretical scalar model, but also by using computer simulations [20, 32-34]. Radjai et al. [32] have studied the statistical distribution of contact forces inside a two dimensional packing of circular rigid disks with solid friction using contact dynamics simulations, and obtained the interesting result that the probability distribution of normal contact forces lower than their respective mean value decays as a power law and that of normal contact forces higher than their respective mean value decays exponentially. Additional simulation work has been done by Thornton and Antony in ref. [34] using discrete element method simulation on three-dimensional poly-disperse systems of elastic spheres with periodic boundary conditions. They found a similar behaviour of power law variation for forces less than half the value of mean value

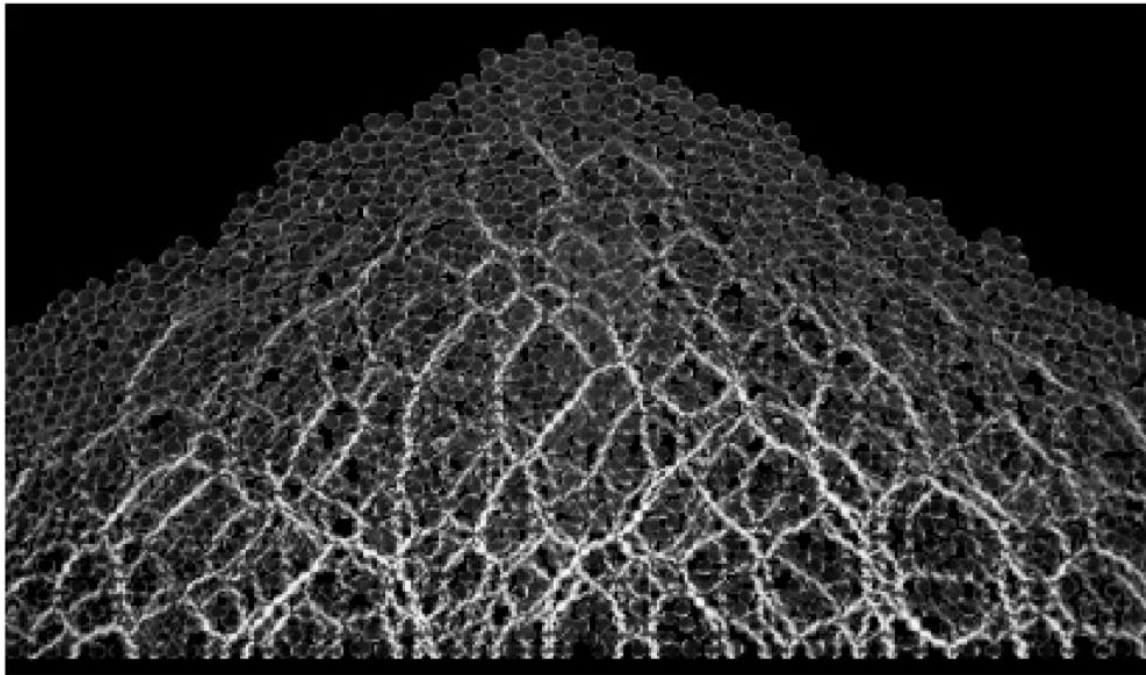
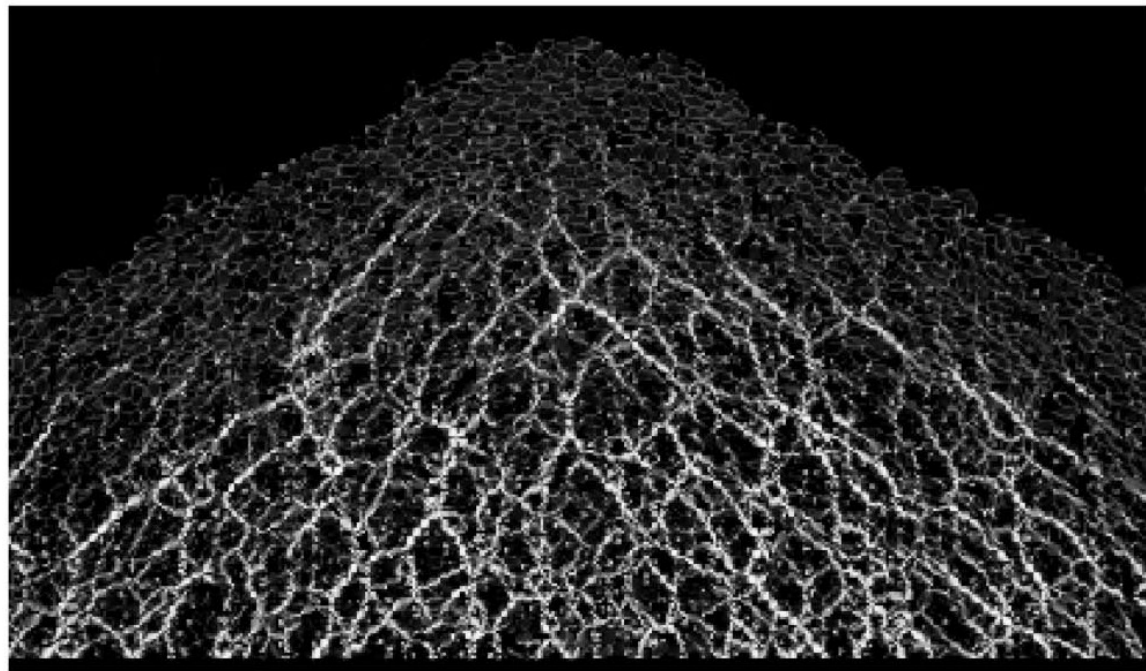
A.**B.**

Figure 1.10: Force network for sand piles [11]. (A) Mixture of disks. (B) Mixture of elliptic cylinders.

and an exponential decay for forces greater than the mean value. Luding in ref. [20] has carried out a molecular dynamic simulation on a two dimensional sand pile, determined the probability distribution for the vertical normal stress network at the bottom layer of the pile, he obtained a power law distribution for small stresses and exponential decay for large stresses.

Mueth et al. [35] performed experiments on three-dimensional random packings of mono-disperse glass beads under uni-axial compression. For this case, they found that the probability distribution of normal force is nearly uniform for forces below the mean value and decays exponentially for forces greater than the mean value of forces.

On the other hand, the structural properties of force chains and angular distribution of the force chain orientation in two dimensional sand piles was determined experimentally by I. Zuriguel et al. in ref. [11] and it was found that, the shape of the particles has a major influence on the packing of granular materials that leads to show different force chain structures in the sand piles. So two sand piles consisting of same materials may have different force distributions. They reported that the chain structure for piles consisting of disks are open and complex patterns evident for piles consisting of elliptic cylinders, as shown in Fig.1.10. It may be gathered from the figure, that more force chains appear for the case of elliptic cylinders than in the case of the disks.

1.3 Motivation

To motivate the study of this problem, we have discussed in this section, why the most simple-minded description of a granulate pile of non-cohesive particles as an elastic continuum may fail. The stress distribution under a sand pile may behave counterintuitively.

This counterintuitive behaviour may be traced back to the fact that the aggregate consists of particles that can be considered rigid to a good approximation and that do not stick together, i.e., the material is non-cohesive. The pile as a whole will nevertheless be able to show elastic or plastic response to external loads as the particles can rearrange under pressure to fill voids more completely, so there will be a finite macroscopic deformation resulting from a finite load. In fact, in our simulations, which will be explained in the next chapter, we give the particles a finite elastic modulus for reason of convenience, and we find when measuring the macroscopic modulus of the bulk quantities, that it is usually about a factor 10 smaller. Hence the assumption of rigid particles is not a bad one to begin with.

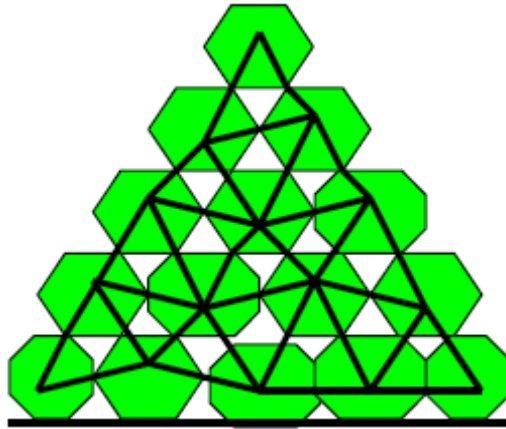


Figure 1.11: Schematic diagram of the contact network of the particle.



Figure 1.12: Contact network between particles that are connected with different numbers of bars. **A.** shows a (hypostatic) network that contains four bars with four nodes. **B.** shows for an (isostatic) network having five bars and four nodes. **C.** a (hyperstatic) network consisting six bars and four nodes.

Since the only effects that hold the pile together near its surface are friction and geometric constraints, the free surface of the heap has a tendency to flow, which means that in its vicinity plastic behaviour should be anticipated.

On the other hand, deep inside the pile, elastic behaviour is not necessarily to be expected, if mechanical aspects suggested by analogies from the field of structural rigidity are considered [37]. Once the pile has been constructed, one can connect particles that touch each other by straight lines establishing a so-called contact network. Forces

between the particles are mostly aligned with the links of this network as one can see in Fig.1.11. Of course, there are forces due to friction and geometrical constraints also perpendicular to a link but if the elastic modulus of the particle is large; these lateral forces tend to be smaller than the forces due to the compression of one particle by another.

The field of structural rigidity studies the behaviour of networks of rotatable bars connected with each other, and one idea applied to granular media was that the contact network can be considered as a network of such bars which can only sustain compressive loads. A network of rotatable bars is flexible (= hypostatic), isostatic or overconstrained (= hyperstatic), depending on whether the number of bars connecting vertices is smaller than, equal to, or larger than, the number needed to maintain stable equilibrium. Now if the network contains too few bars for a given number of nodes, it will be **flexible** and collapse under tiny loads. This is exemplified in Fig. 1.12.A, showing a network consisting of four nodes and four bars. If it is pushed from the top or the side, it will collapse. To stabilize it, a fifth bar has to be included, as shown in Fig. 1.12.B. A network having exactly the number of bars that is necessary for stability, i.e., for which removal of one bar makes part of it flexible, is called **isostatic**. If there are more bars than necessary for structural rigidity, the network is **overconstrained** as shown in Fig. 1.12.C. If the links between touching grains in a sand pile are considered as the “bars” of a network, then the non-cohesive nature of the granular constituents allows only bars under compression, which rules out the possibility of an overconstrained network. It is easy to understand that in overconstrained networks there must be positive self-stresses, that is stresses that pull on the bar. Such a situation is forbidden in a non-cohesive granular medium, leaving the sand pile to be either hypostatic or isostatic.

In the limit of infinite elastic constants of the particles, the self stresses can be shown to become more important than stresses due to external load (the self-stresses scale with the elastic constants, the external loads do not), so any stable sand pile having no cohesive forces must be isostatic. This means that a sand pile consisting of rigid particles should be very susceptible to external perturbations, since the application of a small perturbation, for example the removal of a few particle contacts should destroy its stability or the stability of a big part of it. The ability of the sand pile to react strongly to external perturbation has been linked with the idea that the equations describing a static sand pile might be hyperbolic instead of elliptic. Which is an issue that should be clarified.

If the elastic constants are large but finite, the sand pile may show some elastic properties but the effects of isostaticity should still make themselves felt. Hence the description of its mechanical behaviour may be nontrivial.

Arguments based on the different scaling behaviour of self stresses and imposed stresses [37] seemed to imply isostaticity for granular matter loaded only by its own weight. Then the average coordination number z of grains would have to correspond exactly to a critical value z^{crit} (6 in two dimensions for frictionless non-circular particles and 3 with friction). The mechanical equilibrium conditions of isostatic structures lead to hyperbolic field equations, whereas static elasticity is described by elliptic equations.

However, it has been pointed out that load and geometry are not independent [38] in sand piles, and the distinction should be between isostatic and non-isostatic *problems* rather than *structures* [38-39]. Solutions of isostatic problems with prescribed load may lead to hypostatic structures, describable by elliptic equations; hence the introduction of effective elastic coefficients may be meaningful [38].

In fact, while there are a number of continuum models producing the pressure minimum, there is no agreement yet on what is the correct macroscopic description. Numerical simulations may help to produce a data basis allowing to separate out those models that can not work; they may even provide hints on how to obtain a physically correct model.

Moreover, in order to investigate the matter, i.e. the shape distribution influence on the pressure distribution, the objective of our study is to investigate numerically the features of the basic phenomenon, taking into account that many granular materials such as rice, crops and sand consists of non-spherical particles. Our study is exclusively based on numerical experiments on assemblies of granular materials by implementing an efficient numerical technique, which will help us to investigate the mechanical properties, the effective material properties of granular materials with or without applying external overloads, and to make qualitative and quantitative comparison to the experimental data and those of analytical predictions of stress distributions.

2

The simulation method

2.1 Why computer simulations are needed for granular materials

Computer simulations have now been used for over fifteen years to study the behaviour of granular materials, due to the increase in computing power. The advantage of computer simulations is that they can provide the details of what is actually going on inside the granular system, this means, at every instant of time, the displacement, position, the point of contact and the contact forces of the individual particles are known, which allows us to analyze and visualize the behaviour inside the granular media.

In addition, it might be impossible or difficult to determine some quantities in experiments on granular systems while it is possible to determine such quantities in the computer simulation. One of the common examples is the evaluation of the strain tensor in experiments on granular heaps. In some cases, much money is spent for doing experiments on granular systems. Moreover, simulations allow repeatability of the granular system as exactly the same specimen can be retested any number of times under different boundary condition.

The main problem of the simulation is to develop techniques that are giving sufficiently accurate results, which may also be compared with those of real experiments and those of analytical theories, Simulation allows to determine both microscopic and macroscopic

quantities in granular systems which are of experimental and theoretical interest. Moreover, one can develop a continuum description after obtaining the macroscopic data from the computer simulation.

2.2 Different methods to simulate granular media

Granular materials exhibit a wide variety of behaviours, they may be deformed like a solid, are able to flow like a liquid, or may even be compressible as a gas. They are very interesting both as dynamical and statistical systems. There are various methods which may be used to model the behaviour of granular material. The methods to simulate the behaviour of granular material may be classified mainly by two approaches which are as follows:

- Continuum mechanic methods
- Particle based approaches

Continuum mechanics methods have been used extensively over the past few years to model the flow of granular materials. Using this method, one can formulate the governing equations for the stress and strain (velocity) fields by coupling the equations of conservation of mass and linear momentum with appropriate constitutive laws. There is general agreement that stress fields within the granular media can be described by coupling the equations of linear momentum with Coulomb-Mohr yield conditions. Within this approach, constitutive models (laws) are needed for modelling the behaviour of granular. In this method, the equations of motion are derived for a volume element (macroscopic level) and governing equations describing the constitutive behaviour of granular materials. Continuum mechanics can be applied successfully for modelling rapid granular flow problems. For the principles and reviews of continuum mechanics approaches see refs. [40-51].

However, continuum mechanics methods do not give any information about the positions, velocities and forces at the microscopic level of particles, which makes it difficult to determine the force network and velocity distribution inside the granular materials.

On the other hand, within this approach, it is recognized that the equations of continuum mechanics are used (as a basis for the creation of mathematical model) to investigate the behaviour of granular materials. However, suitable mathematical models are still lacking to describe the complex systems of various granular materials, because of the different shapes of the particles, the structure of the granular material, and energy dissipation due to the inelastic nature of collision between two particles and between wall and particle. In addition, this approach is very limited in its application to granular systems, only applicable for some particular materials and particular processes, see in ref. [51]. In some cases, it may be very difficult to solve the mathematical equations (the so-called

continuum equations) that appear in the model of the continuum mechanical method or these equations are subject to strong instabilities when linearized [52-53]. Continuum mechanics are most appropriate for simplest geometries (to solve continuum equations easily) and also for simpler shapes of particles (smooth), which not contain additional degrees of freedom, unlike, for example, rough or non-spherical particles.

Furthermore, sometimes, the results obtained by using this approach are not in very good agreement with the experimental results. For example, this has been shown by Savage in ref. [50]. He used the continuum mechanics approach to study the streaming motions in a bed of vibrationally fluidized dry granular materials and obtained results from his study, which differ by approximately one order of magnitude from the experimental results.

On the other hand, there exist various numerical simulation methods (based on a microscopic approach) such as the contact dynamics (CD) method, cellular automata (CA), and the discrete element method (DEM) to analyze the behaviour of individual particles within granular materials. With these approaches, one can determine the trajectory of each particle by calculating the interaction between colliding particles and solving Newton's equations of motion for individual particles.

Contact dynamics (CD) is a very efficient numerical method to simulate a granular system consisting of perfectly rigid particles, originally suggested in Ref [54]. It is based on the idea that the particle interaction occurs via the contact points of particles. This means, the colliding particles are touching but not overlapping because they are infinitely rigid. Consequently, the repulsive normal force is zero for two particles not in contact with each other, whereas, when two particles are in contact, it can take any value necessary to prevent an overlap of the interacting particles. This method was used by many researchers and its detailed description is presented in refs. [55-58]. This method is mostly useful for static or almost static situations, i.e. for slow dynamics, especially for rigid particles, not for soft particles. It has problems with the granular or inelastic collapse. This method is unrealistic for our work, because it is difficult to realize for polygonal particles.

One of the simplest methods to describe and simulate the behaviour of complex granular systems is the cellular automaton (CA) method. It is a lattice-based model and the system is composed of adjacent cells which are either empty or occupied by the particles of the material, usually cells are organized as a regular hexagonal, triangular or rectangular lattice. All cells update their states at the same time, using a transition rule which takes into account the current state of a fixed set of neighbours and usually also of the cell itself. In this scheme, the rule may be deterministic or probabilistic, as the interactions that can occur between particles moving around a lattice connecting adjacent cell centres. The rules themselves may include mass and momentum conservation (albeit) in a simple, discrete manner.

This method has been used not only in research fields dealing with flow of fluid and gas problems [59-61], but also to simulate the behaviour of granular materials during piling, vibration, and segregation in refs. [59] [62-75]. Moreover, it also has been used to

simulate rapid flow in silos [69-72] and to determine flow patterns of non-cohesive granular materials in a model of silo [73]. The advantage of the cellular automaton method is the small amount of computational time needed to describe the behaviour of granular system consisting of large number of particles. However, the disadvantage of the approach is that the models are purely kinematics wherein flow dynamics is not taken into account.

Apart from this, the particles interact in very restricted ways that are described by using very simple rules. Cellular automata are not a suitable approach for determining realistic forces, and we are really interested in the force field that cannot be calculated by using this scheme. Therefore, the cellular automaton method is not a good choice to be used for our work.

In this work, we used the most realistic numerical simulation method amongst these techniques, the discrete element method (DEM) to study the behaviour of granular materials. In the following section, the principles of this method for a granular system consisting of a (possibly) poly-disperse mixture of soft convex polygonal particles are explained.

2.2.1 Discrete element method

The discrete element method (DEM) is a modeling technique for analyzing complex systems of individual particles and is used to simulate efficiently both quasi-static and dynamical behaviour of a large granular assembly. It has become a powerful numerical approach for analyzing non-homogeneous and discontinuous materials. It was originally proposed by Cundall and Strack [76] for rock mechanics and later widely applied to granular materials, especially in particle flow simulation. Amongst various modeling techniques, DEM is the most realistic one for dynamical situations, because it explicitly takes into account the forces involved in the formation of assemblies of grains and in our case, also a realistic geometry of the particles. The method can be used to determine quantities that are difficult to obtain experimentally.

In this work, we used a two-dimensional discrete element method to compute the trajectory and rotational motion of each particle. It involves a molecular dynamics simulation with complex particles and force laws, including dissipation. The main difference between the discrete element method and preceding molecular dynamics methods lies in the particle interaction laws. Molecular dynamics simulations of atoms and molecules involve interactions with force laws that may be long range on the atomic scale, discrete element simulations involves inelastic interactions between particles and short range force laws, unless electrostatic forces are taken into accounts. In DEM approaches, the equations of motion (differential equations) describing the trajectories of particles are integrated numerically using a step by step integration procedure, often with a fixed time step. Essentially, one solves Newton's and Euler's equations of motion involving the forces and the torques acting on each particle. The basic structure of the DEM algorithm consists of a loop that contains the three steps:

- collision detection (at time t),
- force computation (at time t),
- solution of the equations of motion (integration process) (integrating up to time $t + \Delta t$).

Since the retained kinematics includes translation and rotation, the acting fields are forces and torques. In assemblies of grains, the forces applied on the individual particle i are classified into two types namely, interaction forces (particle-particle interaction force) and external forces. In the case of a dry non-cohesive granular system, the particle-particle interaction force can be described by the vectorial sum of a repulsive force due to impenetrability of particles (normal force), friction force (static and dynamic solid friction), and damping force (dissipative normal force). The external force is created by gravity.

Hence, the interaction force and external force can be written as

$$\mathbf{F}_i = m_i \mathbf{g} \quad (2.1)$$

$$\mathbf{F}_{ij} = \mathbf{F}_{ij}^{diss,n} + \mathbf{F}_{ij}^{cont,n} + \mathbf{F}_{ij}^{cont,t} \quad (2.2)$$

where $\mathbf{F}_{ij}^{diss,n}$ =dissipative force,

$\mathbf{F}_{ij}^{cont,n}$ = normal component of contact force, and

$\mathbf{F}_{ij}^{cont,t}$ = tangential component of contact force.

The normal forces are calculated from the overlap area of the particles, whereas, the tangential force is calculated using a Coulomb type friction coefficient between particles. The dissipative normal force is calculated from the velocity during the time of overlap of particles using a phenomenological damping constant. How these forces are calculated in detail, will be explained in the following section.

In principle, there exists another type of forces, namely cohesive forces which we don't consider in our force calculation since we simulate only dry granulates, which are typically non-cohesive.

In general, particle motion is composed of a translational and rotational component. In two dimensions, the momentum balance provides two equations per particle, the angular momentum balance one, because there is only one angle of rotation. Then we have Newton's and Euler's equation of motion, given by

$$\begin{aligned} m_i \ddot{\mathbf{r}}_i &= \mathbf{F}_i + \sum_{j=1}^{n(i)} \mathbf{F}_{ij} \\ I_i \ddot{\phi}_i &= L_i + \sum_{j=1}^{n(i)} L_{ij}. \end{aligned} \quad (2.3)$$

Here, the subscript i runs over all the particles, $n(i)$ is the number of contact points of the particle i , and the subscript j runs over all the contacts of the particle i with other particles. That, is forces and torques are exchanged between two particles only, if they touch, hence we have short range forces, namely contact forces. \mathbf{F}_i is the force acting on each particle i due to external fields, in our case this is only gravitation. \mathbf{F}_{ij} is the sum of the normal contact force and tangential contact force as well as the dissipative force produced by the particle touching particle i in contact j .

It is evident that

$$\mathbf{F}_{ij} = -\mathbf{F}_{ji}. \quad (2.4)$$

Three or multi-particle contact forces are ignored, the event of three particles having a common overlap area practically does not occur in our simulations.

Since the direction of the force will not point to the centre of mass of a particle in general, the force will produce a torque L_{ij} on particle i about that centre. This will lead to an angular acceleration $\ddot{\phi}_i$; I_i is the moment of inertia of particle i about its centre of mass. So particle rotations are fully taken into account in our simulation.

The torques L_{ij} are determined as the vector product of the force \mathbf{F}_{ij} and the vector \mathbf{r}_i from the centre of mass of the particle i to the contact point of the two overlapping particles

$$\mathbf{L}_{ij} = \mathbf{r}_i \times \mathbf{F}_{ij}. \quad (2.5)$$

Since we work in two dimensions, all torques point in the same direction orthonormal to the considered plane. In the second part of equation (2.3), the term L_i is the external torque acting on the particle i . However, in our work there are no external torques that act on the particle, because gravity is the only interaction force, and we consider torques about the centres of mass of the particles. By definition of the centre of mass, gravity does not exert a torque about it.

Therefore, we have $L_i = 0$.

Now, the equation of motion (2.3) can be rewritten as

$$\begin{aligned} m_i \ddot{\mathbf{r}} &= m_i \mathbf{g} + \sum_{j=1}^{n(i)} \mathbf{F}_{ij} \\ I_i \ddot{\phi}_i &= \sum_{j=1}^{n(i)} L_{ij}. \end{aligned} \quad (2.6)$$

These two equations are driving the motion of the granular medium. How this force is calculated, will be explained in Section 2.4. The shown equations (2.6) are solved with an explicit-implicit algorithm, usually with a fixed time step by the fifth-order Gear predictor-corrector method. In the following section, we give a short description of the Gear predictor-corrector scheme.

DEM can be classified into two groups:

- Event driven method (ED),
- Time driven method (TD).

2.2.1.1 Event-driven method

An event-driven (ED) simulation is based on the idea that each individual particle of a granular medium exhibits ballistic motion as long as it is not in contact with other particles. Ballistic motion is easily computed analytically, so the state of the particles needs to be updated numerically only at the times of collisions. The method was developed by D. Lubachevsky in 1991 [77]. In this approach, all collisions between particles are supposed to be binary i.e. multiparticle collisions cannot occur, perfectly rigid spherical particles are used, and the time for the collision (contact) between two particles is implicitly zero (infinitely small). Since the time of contact is very short, this method is sometimes referred to as hard sphere model. In a real system each contact takes a finite time so that multiparticle contacts are possible (but rare). ED was used in refs. [77-83]. Dissipation occurs only on collision and energy dissipation during a collision is defined via the coefficient of restitution. The positions and velocities of the particles are determined after every binary collision.

The algorithm of the ED method is very simple. In order to get the new status, we start at the time t : In the first step, one must determine the time of next collision t_c for each particle, to find the minimum, the second step is compute the positions and velocities of all particles for the time interval $\Delta t = t_c - t$, which can be calculated analytically with:

$$\mathbf{r}_i(t_c) = -\frac{1}{2}\mathbf{g}\Delta t^2 + \mathbf{v}_i(t)\Delta t + \mathbf{r}_i(t), \quad (2.7)$$

$$\mathbf{v}_i(t_c) = -\mathbf{g}\Delta t + \mathbf{v}_i(t), \quad (2.8)$$

where $\mathbf{r}_i(t)$ and $\mathbf{v}_i(t)$ are the coordinates and velocities of particle i at time t , and then in the third step one has to determine the collision \mathbf{v}'_{ij} of the particles i and j from the velocity and the position with a relation of the form

$$\mathbf{v}'_{ij}(t_c) = \mathbf{F}(\mathbf{r}_i(t_c), \mathbf{r}_j(t_c), \mathbf{v}_i(t_c), \mathbf{v}_j(t_c)). \quad (2.9)$$

The expression (2.9) will now allow for obtaining the collision at time $t = t_c$ and the cycle begins again from the first step until the simulation is accomplished.

The collision is described by a collision operator, which is determined from the positions and velocities of the colliding particles after the collision. The detailed derivation of the collision operator is discussed in refs. [84-85].

However, the ED method runs into difficulties when the time between collisions becomes too small, typically in systems with strong dissipation, and the so-called ‘‘inelastic collapse’’ occurs [86, 87, 126] i.e., the collision rate diverges for a few particles in the system, it means the energy goes to zero in finite time.

The ED method is particularly suitable for the simulation of granular ‘shear flow’ problems in which the duration of contact between two particles is short. Camball et al. [88-93] have extensively used the ED method to simulate two-dimensional shear flow problems. In addition, it is also suitable to simulate granular gases [86-87]. The event driven method is successfully applied in vibrated granular systems with rigid spherical particles [94-95].

2.2.1.2 Time-driven method

In this numerical simulation work, the time-driven (TD) method was used to simulate granular materials, and it is also called time-driven discrete element method, time step method. When the duration of contact between real particles is larger than the time of the free path of particles, then a time driven method is a better option to be used. This method is very efficient in order to examine successfully both static and dynamical dense granular systems.

One can obtain the state of the particle at each time step by time integration of Newton’s and Euler’s equation of motion (2.6) for translation and rotation of each grain in the assembly of grains. This necessitates to keep track of all the forces and moments acting on each grain. The equation of motion of particles in equation (2.6) is solved with a predictor-corrector method with a fixed time step Δt . During the simulation, the current state of all grains at the time t is updated after a fixed time step Δt , which is smaller than the smallest time of impact.

In an event-driven (ED) simulation as discussed in the previous section, the duration of contact of two particles is ideally zero, which may lead to a diverging energy dissipation rate in the system, whereas the duration of the contact of two particles is finite in a time driven discrete element simulation. Energy dissipation rates remain finite. Another advantage of the time-driven DEM is that polygonal particles can be used for the simulation, whereas the event-driven method is efficient only for circular or spherical particles.

While particles have to be rigid in event-driven methods to exploit their advantage which consists in avoiding lengthy force calculation, they must be soft in time-driven simulations to enable the use of sufficiently long time steps.

The choice of a time step is necessary for a realistic simulation. The time step for the time integration of the particle position, velocity, orientation and angular velocity depends on the contact time of two colliding particles. In order to increase the program efficiency, the time step must be large enough, because if one chooses a very small time step, this unnecessarily increases time consumption for the simulation to be accomplished. On the other hand, the time step must be small enough, otherwise the numerical error becomes too large.

In this work, the predictor corrector scheme needs about 10 time steps in order to describe a collision correctly. The typical time step chosen in this work to have a good resolution of collisions was

$$\Delta t = \frac{1}{10} \sqrt{\frac{m}{Y}} \cdot \pi. \quad (2.10)$$

Here, m is the mass of the lightest particle and Y is the Young's modulus of simulated particle.

2.3 Integration scheme

During the integration process, the most time consuming part is the calculation of forces between two interacting particles. Different types of integration schemes like Euler scheme, Verlet scheme, velocity-Verlet scheme, third-order Predictor-Corrector scheme, and fifth-order Predictor-Corrector scheme can be used to solve the equations of motion of the particles (2.6).

Amongst all schemes presented above, the simplest algorithm which may be used to solve the equations of motion is the Euler scheme and the method is called an explicit method. This method was used by Taguchi [96]. In this scheme, at time t , the acceleration for particle i at position x_i is calculated from the following relation

$$\mathbf{a}_i(t) = \frac{\mathbf{F}_i(x_i(t))}{m_i}, \quad (2.11)$$

where \mathbf{F}_i is the force acting on the particle i with mass m_i .

The particle position and velocity are then calculated at the next time step $(t + \Delta t)$ using the first order Taylor expansion of $\mathbf{x}_i(t + \Delta t)$ and $\mathbf{v}_i(t + \Delta t)$, which are given by

$$\mathbf{x}_i(t + \Delta t) = \mathbf{x}_i(t) + \mathbf{v}_i(t) \Delta t, \quad (2.12)$$

$$\mathbf{v}_i(t + \Delta t) = \mathbf{v}_i(t) + \mathbf{a}_i(t) \Delta t, \quad (2.13)$$

where $\mathbf{v}_i(t)$ and $\mathbf{a}_i(t)$, respectively, denote the velocity and acceleration of the particle i at time t .

However, the Euler scheme is usually a quite inefficient method to solve the equation of motion because one needs to assume a very small time step of the integration in order to achieve accuracy and (mostly) stability; this will lead a decrease of the speed of the simulation. This scheme has an error of order $O(\Delta t)$.

A better method than the Euler method is the Verlet method [97]. This method uses a Taylor series expansion up to second order of the position $\mathbf{x}_i(t + \Delta t)$ of the particle, in order to obtain the positions and velocities, given by

$$\mathbf{x}_i(t + \Delta t) = \mathbf{x}_i(t) + \mathbf{v}_i(t) \Delta t + \frac{1}{2} \Delta t^2 \mathbf{a}_i(t), \quad (2.14)$$

$$\mathbf{x}_i(t - \Delta t) = \mathbf{x}_i(t) - \mathbf{v}_i(t) \Delta t + \frac{1}{2} \Delta t^2 \mathbf{a}_i(t). \quad (2.15)$$

Then, subsequent addition of these two equations (2.14) and (2.15) which allows providing the new position $\mathbf{x}_i(t + \Delta t)$ at time $(t + \Delta t)$ in terms of the current and preceding times t and $t - \Delta t$

$$\mathbf{x}_i(t + \Delta t) = 2\mathbf{x}_i(t) - \mathbf{x}_i(t - \Delta t) + \mathbf{a}_i(t) \Delta t^2. \quad (2.16)$$

The velocity is obtained by subtraction of equations (2.14) and (2.15), which gives the following expression

$$\mathbf{v}_i(t) = \frac{\mathbf{x}_i(t + \Delta t) - \mathbf{x}_i(t - \Delta t)}{2\Delta t}. \quad (2.17)$$

In this integration scheme, one can easily calculate the error from equation (2.16) for the position as it is of the order $O(\Delta t^4)$, whereas, the error for the calculation of velocities can be obtained from the equation (2.17). It is of order $O(\Delta t^2)$, which is less accurate.

The global error is $O(\Delta t^2)$, the Verlet scheme is a second-order scheme. Because of the less accurate estimate of velocity this scheme is not very efficient to solve the equation of motion.

There is another improved version called as velocity-Verlet scheme to overcome this problem of the original version of the Verlet scheme. The method is based on the idea to store positions, velocities, and accelerations at the same time t , and this will lead to minimize the round-off error. It has been proposed by Swope et al. [98]. The velocity-Verlet algorithm was used by Aoki et al. [99] (in their simulation study of vibrated beds of granules) for integrating the equation of motion. The position and velocity are determined in the velocity-Verlet scheme via

$$\mathbf{x}_i(t + \Delta t) = \mathbf{x}_i(t) + \mathbf{v}_i(t)\Delta t + \frac{1}{2}\Delta t^2\mathbf{a}_i(t), \quad (2.18)$$

$$\mathbf{v}_i(t + \Delta t) = \mathbf{v}_i(t) + \frac{1}{2}\left(\mathbf{a}_i(t) + \frac{1}{2}\mathbf{a}_i(t + \Delta t)\right)\Delta t. \quad (2.19)$$

In this scheme, the error is only of the order $O(\Delta t^5)$. The scheme is described in detail by Allen and Tildesley [30].

Among other integration schemes which we described above, the fifth order Gear predictor-corrector is one of the most popular schemes. In this study, we use a fifth-order Gear-predictor corrector to solve the equation of motion (2.6), which is described briefly in the following section.

2.3.1 Gear Predictor-Corrector method

The Gear predictor-corrector method is a multistep numerical method which allows to obtain the numerical solutions of ordinary differential equations with a given initial condition. According to Gear [100], there are actually three separate steps occurring in a predictor-corrector method which we call prediction, evaluation (approximation) and correction. In our work, we use in the first step of this method, a predictor method to predict the position and velocity of the particles at a given time step. Then, in the second step, we calculate the particle forces as an approximation value using the information obtained in the first step, and finally in the third step, we use a corrector method for correcting the position and velocity of the particles.

The fifth order Gear predictor-corrector scheme was used by H. G. Matuttis [101], Jysoo Lee [102], and A. Schinner [103].

We first use the predictor step for predicting the position, velocities, acceleration, and higher order of time derivatives up to fifth order of accuracy. The predicted position

$\mathbf{x}^p(t + \Delta t)$, velocity $d\mathbf{x}^p(t + \Delta t)/dt$ and higher order time derivatives of position $d^n \mathbf{x}^p(t + \Delta t)/dt^n$ which were derived by using **Taylor Expansion Series** up to fifth order, and expressed by the following expression,

$$\begin{aligned}\mathbf{x}^p(t + \Delta t) &= \mathbf{x}(t) + \Delta t \frac{d\mathbf{x}(t)}{dt} + \frac{\Delta t^2}{2} \frac{d^2\mathbf{x}(t)}{dt^2} + \frac{\Delta t^3}{6} \frac{d^3\mathbf{x}(t)}{dt^3} + \frac{\Delta t^4}{24} \frac{d^4\mathbf{x}(t)}{dt^4} + \frac{\Delta t^5}{120} \frac{d^5\mathbf{x}(t)}{dt^5} \\ \frac{d\mathbf{x}^p(t + \Delta t)}{dt} &= \frac{d\mathbf{x}(t)}{dt} + \Delta t \frac{d^2\mathbf{x}(t)}{dt^2} + \frac{\Delta t^2}{2} \frac{d^3\mathbf{x}(t)}{dt^3} + \frac{\Delta t^3}{6} \frac{d^4\mathbf{x}(t)}{dt^4} + \frac{\Delta t^4}{24} \frac{d^5\mathbf{x}(t)}{dt^5} \\ \frac{d^2\mathbf{x}^p(t + \Delta t)}{dt^2} &= \frac{d^2\mathbf{x}(t)}{dt^2} + \Delta t \frac{d^3\mathbf{x}(t)}{dt^3} + \frac{\Delta t^2}{2} \frac{d^4\mathbf{x}(t)}{dt^4} + \frac{\Delta t^3}{6} \frac{d^5\mathbf{x}(t)}{dt^5} \\ \frac{d^3\mathbf{x}^p(t + \Delta t)}{dt^3} &= \frac{d^3\mathbf{x}(t)}{dt^3} + \Delta t \frac{d^4\mathbf{x}(t)}{dt^4} + \frac{\Delta t^2}{2} \frac{d^5\mathbf{x}(t)}{dt^5} \\ \frac{d^4\mathbf{x}^p(t + \Delta t)}{dt^4} &= \frac{d^4\mathbf{x}(t)}{dt^4} + \Delta t \frac{d^5\mathbf{x}(t)}{dt^5} \\ \frac{d^5\mathbf{x}^p(t + \Delta t)}{dt^5} &= \frac{d^5\mathbf{x}(t)}{dt^5}\end{aligned}\tag{2.20}$$

where $\mathbf{x}(t)$ is the position of the particle at the time step t ,

$\frac{d\mathbf{x}(t)}{dt} = \mathbf{v}(t)$ is the velocity of the particle at the time step t , and

$\frac{d^2\mathbf{x}(t)}{dt^2} = \mathbf{a}(t)$ is the acceleration of the particle at the time step t .

We abbreviate the derivative term in the set of equations (2.20) as follows

$$x_n(t) = \frac{\Delta t^n}{n!} \frac{d^n \mathbf{x}(t)}{dt^n}, \text{ with } x_0(t) = \mathbf{x}(t), n=0, 1, 2, 3, 4, 5.\tag{2.21}$$

Substituting into the set of equations (2.22), yields

$$\begin{aligned}
\mathbf{x}_0^p(t + \Delta t) &= \mathbf{x}_0(t) + \mathbf{x}_1(t) + \mathbf{x}_2(t) + \mathbf{x}_3(t) + \mathbf{x}_4(t) + \mathbf{x}_5(t) \\
\mathbf{x}_1^p(t + \Delta t) &= \mathbf{x}_1(t) + 2\mathbf{x}_2(t) + 3\mathbf{x}_3(t) + 4\mathbf{x}_4(t) + 5\mathbf{x}_5(t) \\
\mathbf{x}_2^p(t + \Delta t) &= \mathbf{x}_2(t) + 3\mathbf{x}_3(t) + 6\mathbf{x}_4(t) + 10\mathbf{x}_5(t) \\
\mathbf{x}_3^p(t + \Delta t) &= \mathbf{x}_3(t) + 4\mathbf{x}_4(t) + 10\mathbf{x}_5(t) \\
\mathbf{x}_4^p(t + \Delta t) &= \mathbf{x}_4(t) + 5\mathbf{x}_5(t) \\
\mathbf{x}_5^p(t + \Delta t) &= \mathbf{x}_5(t)
\end{aligned} \tag{2.22}$$

The above set of equation can be rewritten in the matrix form given by

$$\begin{pmatrix} \mathbf{x}_0^p(t + \Delta t) \\ \mathbf{x}_1^p(t + \Delta t) \\ \mathbf{x}_2^p(t + \Delta t) \\ \mathbf{x}_3^p(t + \Delta t) \\ \mathbf{x}_4^p(t + \Delta t) \\ \mathbf{x}_5^p(t + \Delta t) \end{pmatrix} = \begin{pmatrix} 1 & 1 & 1 & 1 & 1 & 1 \\ 0 & 1 & 2 & 3 & 4 & 5 \\ 0 & 0 & 1 & 3 & 6 & 10 \\ 0 & 0 & 0 & 1 & 4 & 10 \\ 0 & 0 & 0 & 0 & 1 & 5 \\ 0 & 0 & 0 & 0 & 0 & 1 \end{pmatrix} \begin{pmatrix} \mathbf{x}_0(t) \\ \mathbf{x}_1(t) \\ \mathbf{x}_2(t) \\ \mathbf{x}_3(t) \\ \mathbf{x}_4(t) \\ \mathbf{x}_5(t) \end{pmatrix} \tag{2.23}$$

Once the position, velocity, acceleration and higher order time derivatives are predicted, then in the second step, we evaluate the particle forces at time step $t + \Delta t$ according to the latest value of positions and velocities of particles and hence, now we have the accelerations, given by

$$\mathbf{a}^c(t + \Delta t) = \frac{\mathbf{F}^p(\mathbf{x}^p(t + \Delta t), \mathbf{v}^p(t + \Delta t))}{m}, \tag{2.24}$$

where m is the mass of the particle.

Then in the third step, the positions, velocities, accelerations and higher-order time derivatives are corrected using the new accelerations. These corrected expressions can be

compared with the predicted expression from expression (2.22), to estimate the size of the error in the prediction step

$$\Delta \mathbf{a}(t + \Delta t) = \mathbf{a}^c(t + \Delta t) - \mathbf{a}^p(t + \Delta t). \quad (2.25)$$

It is to be noted that the correction step is dependent on the order of the differential equation which has to be solved.

The error in the equation (2.25) and the results of the predictor step, are fed into the corrector step, given by

$$\begin{pmatrix} \mathbf{x}_0^c(t + \Delta t) \\ \mathbf{x}_1^c(t + \Delta t) \\ \mathbf{x}_2^c(t + \Delta t) \\ \mathbf{x}_3^c(t + \Delta t) \\ \mathbf{x}_4^c(t + \Delta t) \\ \mathbf{x}_5^c(t + \Delta t) \end{pmatrix} = \begin{pmatrix} \mathbf{x}_0^p(t + \Delta t) \\ \mathbf{x}_1^p(t + \Delta t) \\ \mathbf{x}_2^p(t + \Delta t) \\ \mathbf{x}_3^p(t + \Delta t) \\ \mathbf{x}_4^p(t + \Delta t) \\ \mathbf{x}_5^p(t + \Delta t) \end{pmatrix} + \begin{pmatrix} c_0 \\ c_1 \\ c_2 \\ c_3 \\ c_4 \\ c_5 \end{pmatrix} \Delta \mathbf{a}(t + \Delta t). \quad (2.26)$$

The corrected terms on the left hand side of the equation (2.26), are now better approximations to the true positions, velocities, acceleration and higher order time derivatives. The values of the Gear Predictor-Corrector coefficients c_i depend upon the order of differential equation which has to be solved and desired accuracy of the trajectories of the particles.

For a second order differential equation of the form

$$\frac{d^2 \mathbf{x}}{dt^2} = f\left(\mathbf{x}, \frac{d\mathbf{x}}{dt}\right), \quad (2.27)$$

the values of the Gear corrector coefficients c_i are

$$c_0 = \frac{3}{16}, \quad c_1 = \frac{251}{360}, \quad c_2 = 1, \quad c_3 = \frac{11}{18}, \quad c_4 = \frac{1}{6}, \quad c_5 = \frac{1}{60}. \quad (2.28)$$

2.4 Force calculation

In this study, we use soft but shape-invariant particles: two particles in contact with each other are allowed to interpenetrate partially. Using rigid particles rigorously would require different methods such as contact dynamics or event-driven dynamics, which however would necessitate the consideration of simpler particle shapes such as circles. In principle, if using soft particles, one should allow them to deform on contact. The reason this is not done is that it would be inefficient to solve the elastic equations for each collision between pairs of soft particles meaning an impractically large computational effort for the solution of elastic equations, and a partial differential equation would have to be solved for each pair of particles in contact. Instead, the size, direction and point of application of the force are calculated from the geometric characteristics overlap area and contact length using the relative velocity of the two particles. The repulsive force between two particles is increased when the area of overlap becomes larger. Therefore, in a real simulation, the overlap always remains small in comparison with the particle extension.

The dynamics of the granular system can be obtained by numerically integrating the equations of motion for all particles simultaneously with appropriate initial conditions. The detailed formulation of the normal and tangential forces depends on the grain model [104]. In the following section, these forces are described in more detail. We start with the most important force which is the repulsive normal force, and advance to the more difficult tangential force in Subsection 2.4.2.

2.4.1 Normal force

Normal forces are supposed to act in the normal direction of the particle contacts. Fig.2.1 displays a pair of overlapping particles namely i and j . Each force acts at a contact point between two particles. In general, the direction of the force will not point towards the centre of mass of the particle.

The normal force F_{\perp} can be decomposed into two parts, namely the repulsive normal force R_{\perp} (i.e., elastic part) and the dissipative normal force D_{\perp}^* , i.e. it can be written as

$$F_{\perp} = R_{\perp} + D_{\perp}^*. \quad (2.29)$$

The point of contact denoted as s_{ij} in which the contact forces are applied, is determined as the centre of the line of contact, joining the two intersection points p_1 and p_2 of the polygons. Here r_i and r_j are the vectors from the centre of mass of the respective particles to the centre of the contact line.

In a way, the most important force is the repulsive normal force which is taken proportional to an effective interpenetration depth d_{eff} , defined as the area A of the overlap between the two particles divided by the contact length l . This force is also proportional to the Young's modulus of elasticity E .

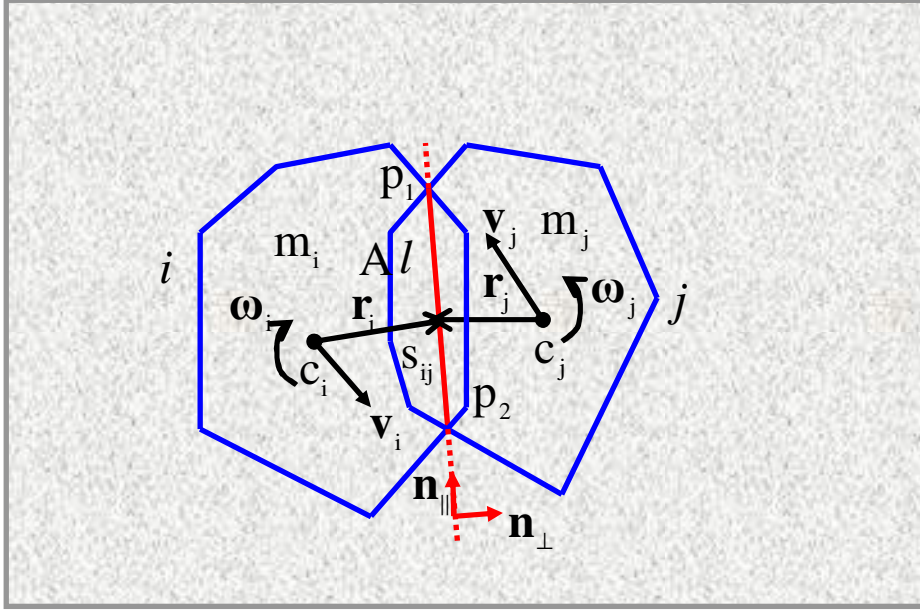


Figure 2.1: Illustration of the geometry used in the calculation of the forces acting on particle i in contact with particle j .

Therefore, the repulsive normal force R_{\perp} can be written as

$$R_{\perp} = E d_{eff} = E \frac{A}{l}. \quad (2.30)$$

The contact length l is defined using on the distances between the centres of mass and the force points r_i and r_j as

$$l = \frac{r_i r_j}{r_i + r_j}. \quad (2.31)$$

Young's modulus in 2D has the units N/m. We use a fixed value of Young's modulus $E = 10^7 \text{ N/m}$ for each particle.

In the case of circular particles, this law for the normal forces reduces to the Hertz [105] contact law (valid for spheres)

$R_{\perp} \propto Ed^{3/2}$, where d is the overlap distance.

Besides this most key feature of assemblies of granular particles, the repulsive normal force, another important feature is the dissipation of energy which occurs due to the inter-particle collisions i.e., the kinetic energy is transferred into internal degrees of freedom of a particle and finally into heat. The formulation of the dissipative part of the force depends on the mechanism of damping. The simplest mechanism is visco-elastic damping, which we will focus on. Since we are interested to simulate static arrangements of particles, it is useful to use viscous damping in order to reach the steady state quickly.

The dissipative normal force D_{\perp}^* is proportional to the effective interpenetration velocity, with a damping constant γ which gives the strength of the damping. The damping constant can be treated as a material property directly linked to the normal coefficient of restitution.

So the dissipative normal force can be written as

$$D_{\perp}^* = \gamma \dot{d}_{eff} \sqrt{Em_{\perp}}. \quad (2.32)$$

In the case of a purely elastic collision, the damping constant would be $\gamma = 0$.

The effective mass m_{\perp} of the two particles is calculated from

$$m_{\perp} = \frac{m_i m_j}{m_i + m_j}, \quad (2.33)$$

and the effective interpenetration velocity is given by

$$\dot{d}_{eff} = \frac{\Delta A}{\Delta t} / l, \quad (2.34)$$

where $\frac{\Delta A}{\Delta t}$ is the change of contact area per time.

Actually, the dissipative normal force D_{\perp}^* is taken as the damping force D_{\perp} only as long as its combination with R_{\perp} does not lead to an attraction of the particles (which could happen during the time when the distance between the particle increases after a collision and \dot{d}_{eff} becomes negative). If that would happen D_{\perp}^* is cut off at the value $-R_{\perp}$, that means one has to make sure that the damping can not become larger than the repulsive normal force in the case of separating particles, otherwise we might have unphysical oscillations of the separating particles. Therefore, the damping force in the normal direction D_{\perp} is given by

$$D_{\perp} = \begin{cases} D_{\perp}^* & \text{for approach} \\ \max(D_{\perp}^*; -R_{\perp}) & \text{for separation.} \end{cases} \quad (2.35)$$

2.4.2 Tangential force

We need to model friction which leads to a tangential force along the contact line. This is done following the ideas of Cundall and Strack. However, it is more difficult to write a model for the tangential force, as here the phenomena of the tangential deformation and both static and dynamic friction have to be modelled. This frictional force prevents a sand pile from deliquescing to a puddle, even though this would be a more favorable state of potential energy.

The relative tangential velocity V_{\parallel} of two particles is obtained according to

$$\mathbf{V}_{\parallel} = \left((\mathbf{v}_i - \mathbf{v}_j + \mathbf{r}_i \times \boldsymbol{\omega}_i - \mathbf{r}_j \times \boldsymbol{\omega}_j) \cdot \mathbf{n}_{\parallel} \right) \mathbf{n}_{\parallel}, \quad (2.36)$$

where \mathbf{v}_i and \mathbf{v}_j are the velocities of the particles i and j and $\boldsymbol{\omega}_i$ and $\boldsymbol{\omega}_j$ denote their angular velocities.

In general, as per Coulomb [106], the tangential friction force F_{\parallel} (Coulomb friction force) should be as follows:

$$F_{\parallel}^{static} \leq \mu_s F_{\perp} \quad \text{if } v_{\parallel} = 0, \quad (2.37)$$

$$F_{\parallel}^{dynamic} = \mu_d F_{\perp} \quad \text{if } v_{\parallel} \neq 0, \quad (2.38)$$

where μ_s and μ_d are the coefficients of static and dynamic friction, respectively. The coefficient of static friction and sliding (dynamic) friction are assumed to be equal, $\mu_s = \mu_d = \mu$, for simplicity.

Coulomb friction forces have a definite relationship with the normal force only for sliding contacts. As long as the relative tangential velocity of the particles is zero during contact of two particles, the coulomb friction force takes a value between zero and its maximal value $\mu F_{\perp}(t)$.

A behaviour similar to this desired one is mimicked in the simulation by assigning a spring to each newly established contact. This spring is stretched during the subsequent relative motion of the two particles and exerts an increasing force, until the Coulomb friction is fully activated. Afterwards, the spring does not extend further, it is just moved along with the particles, and the friction coefficient takes its value for sliding friction

We determine the tangential force in the following way, using

1. the relative tangential velocity V_{\parallel} .
2. the square root of a reduced mass m_{\parallel} , mass which includes the moments of inertia of the particles (because the tangential force tends to rotate particles), given by

$$m_{\parallel} = \frac{1}{\frac{1}{m_i} + \frac{1}{m_j} + \frac{r_i^2}{I_i} + \frac{r_j^2}{I_j}},$$

where m_i and I_i are respectively, the mass and moment of inertia of the particle i .

3. and the square root of the ‘‘tangential’’ Young’s modulus = $\frac{2}{7}E$.

So at the beginning of the collision, the tangential force is zero, and it then is adapted after each time step according to

$$F_{\parallel}(t + \Delta t) = \pm \min \left[\left| F_{\parallel}(t) + v_{\parallel} \Delta t \frac{2}{7} E + v_{\parallel} \sqrt{\frac{2}{7} E m_{\parallel}} \right| ; |\mu F_{\perp}(t)| \right]. \quad (2.39)$$

Herein, a viscous term (the square root term) has been added to inhibit unphysical tangential oscillations. The sign \pm is determined by the sign of the first term inside absolute value bars.

It should be noted that these methods of force calculation are very similar to those used in other groups doing discrete element simulations. There may be differences in details of the implementations, but it is generally believed in the physics community that these

details should not be important, because the dynamic and static behaviour falls into only a few different universality classes, largely independent of the microscopic implementation of interactions.

In the case of granular media, this idea of universality leads to the paradigm that for dynamical simulations even the shape of the particles does not play any role, if one makes sure by poly-disperse granulates that there is sufficient disorder. For statics, it may be important that the shape is noncircular, but all else that matters is that there are enough geometric constraints to render the simulation comparable with reality, the detailed realization of shape diversity of the particles should not matter. Moreover, it is important to have some realization of friction, otherwise one will not obtain the correct angle of repose, but whether this is implemented via Cundall-Strack springs or some other clever device (which microscopically does not precisely reproduce Coulomb's law), should be unimportant. Of course, these guiding ideas of universality have to be checked again and again, because it is not impossible to hit a hitherto unknown universality class by accident.

2.5 Collision detection

Many particles in real life like the constituents of sand, gravel etc. are not spherical in shape. In two dimensions, they can be approximated by polygons. In general, the computational time depends on the shape and number of the particles to be simulated. Polygonal simulations can take up to ten times more computer time than their circular particles counterparts. Since we calculate the force between two particles from the overlap, we have to determine all collisions in our simulation. On the other hand, simulating with a large number of polygonal particles one has to wait a long time for the simulation to be accomplished.

Discrete element simulations are often time consuming, so a lot of computational power is needed for the calculation of the forces between the colliding particles during the simulation. Of course, advantage is taken of the short-range nature of the force by calculating only non-vanishing forces, i.e., forces between particles that are really in contact with each other. This necessitates a fast way to determine the contacts. The fast determination of all contacts in a polygonal system is a difficult matter. In order to achieve the fast contact determination in a time that is proportional to the number of particles (not to its square) independent of the complexity, i.e., number of corners of the particles, one has to adopt an efficient algorithm.

There exist a number of algorithms in the literature to simulate granular materials. Potapov and Campbell [107] described a method for the discrete element simulation of a certain class of non-round particles. In this model, the boundaries of particles are composed from segments of circles. These particles can approximate regular polygons well; however, it may be difficult to simulate irregular shapes of particles. Moreover, while this model is fully capable of efficiently simulating nearly mono-disperse polygonal particles with an equal number of corners, it may be difficult to expand this algorithm to poly-disperse mixtures of particles.

An attractive and flexible approach was proposed by Alexander Schinner [108] to speed up discrete element simulations of arbitrary mixtures of particles of any shape and number of corners almost without restriction, which allows one to determine neighborhood relations in poly-disperse mixtures of particles of arbitrary shape, either discs, ellipses or polygons. Algorithms from virtual reality and computational geometry were adopted to reduce computing time. These use bounding boxes and Voronoi regions to determine the overlaps of particles. In this model, particles and walls are represented by convex polygons.

A. Schinner used a combination of two algorithms for collision detection. The first algorithm is called bounding-box algorithm (using an incremental sort and update algorithm) and the second is called closest-feature algorithm. The complexity of these two algorithms is independent of the particle size, shape, and degree of poly-dispersity.

It is to be recognized that, if a simulation contains N particles then a straight forward implementation would require N^2 tests to check all possible pairs of collisions, which will take a much longer time than necessary. Since the discrete element methods typically have short range interactions, most of the pairs of particles will not interact, so they will not contribute to the force calculation. In order to reduce the number of pairs of particles which have to be checked for collision, we used a bounding-box algorithm; this will decrease the computing time. It is based on the fact that if the bounding boxes of two particles do not overlap then the particles itself do not overlap. In a two dimensional system, the bounding box for a particle means the smallest rectangle whose sides are parallel to the coordinate axes, and which completely contains the particle.

The closest-feature algorithm is a fast method for determining the smallest distance of two convex polygons in constant time, independent of the number of the edges. In this algorithm, neighborhood relationships of a polygon are represented by a combination of so-called features i.e. the edges and vertices of the polygon and the associated Voronoi regions. If the distance between the features of two convex polygonal particles is zero, then it is clear that the corresponding particles either touch or overlap; then we have to determine the overlap area between them to be able to calculate the normal repulsive force. Let us consider two polygonal particles, namely A and B . One can compute the distance d_{AB} between them which is the shortest Euclidean distance with this relation

$$d_{AB} = \inf_{P_A \in A, P_B \in B} |P_A - P_B|. \quad (2.40)$$

Here, P_A and P_B are an arbitrary pair of points between two features of the polygons A and B . The pair of nearest points P_A and P_B can be calculated using Voronoi regions.

The detailed description of Voronoi region, bounding boxes algorithm, closest feature algorithm, and parallelization technique are given in ref. [108].

2.6 Determining macroscopic quantities

In this section, we derive the mathematical formulas for various macroscopic tensorial field quantities including stress, strain, fabric, and inertia tensor for sand piles consisting of polygonal particles. First we determine the formula of those tensorial quantities for a single particle and we then average over many particles by introducing a representative volume element (RVE). The averaging procedure and the necessary size of the volume element we use in the calculation of macroscopic quantities will be explained in Section 2.6.5.

2.6.1 Calculation of stress fields

In order to describe the behaviour of granular materials under external loading one has to determine macroscopic state variables like the stress through a proper averaging of microscopic variables. For the stress tensor, the microscopic variables are the forces acting between the particles and the lines connecting the centres of particles with their contact points. The determination of stress tensors in granular materials has been discussed by many researchers in refs. [109-113].

Once we have the forces and their points of contact, it is easy to derive a formula for the average stress obtained in a homogeneous polygonal particle assuming that the forces given in the contact points act on the corresponding edge of the polygon.

We derive the stress tensor in the following way:

For a body in static equilibrium, the stress components at every point should satisfy the differential equation

$$\begin{aligned}\frac{\partial \sigma_{xx}}{\partial x} + \frac{\partial \sigma_{xy}}{\partial y} + F_x &= 0, \\ \frac{\partial \sigma_{xy}}{\partial x} + \frac{\partial \sigma_{yy}}{\partial y} + F_y &= 0,\end{aligned}\tag{2.41}$$

where F_x and F_y are the x and y components of the body forces per unit volume applied to the body.

In the case of $F_x=0$ and $F_y = g_i$, the stress equilibrium equations (2.41) become

$$\begin{aligned}\frac{\partial \sigma_{xx}}{\partial x} + \frac{\partial \sigma_{xy}}{\partial y} &= 0, \\ \frac{\partial \sigma_{xy}}{\partial x} + \frac{\partial \sigma_{yy}}{\partial y} &= -g_i.\end{aligned}\tag{2.42}$$

The above expression (2.42) can be written in the form of

$$\frac{\partial \sigma_{il}}{\partial x_l} = g_i, \quad i = x, y \quad [g_x = 0, g_y = -g]\tag{2.43}$$

with an implied summation over subscript l (Einstein summation convention).

For the computation of the average stress tensor of an individual particle, we multiply both sides of the equation (2.43) by the coordinate x_j and integrate over the “volume” V^p of the particle p .

$$\int_{V^p} x_j \frac{\partial \sigma_{il}}{\partial x_l} dV^p = \int_{V^p} x_j g_i dV^p, \quad (2.44)$$

The left hand side of equation (2.44) can be recast as follows:

$$\begin{aligned} \int_{V^p} x_j \frac{\partial \sigma_{il}}{\partial x_l} dV^p &= \int_{V^p} \frac{\partial(\sigma_{il} x_j)}{\partial x_l} dV^p - \int_{V^p} \sigma_{il} \frac{\partial x_j}{\partial x_l} dV^p \\ &= \int_{V^p} \frac{\partial(\sigma_{il} x_j)}{\partial x_l} dV^p - \int_{V^p} \sigma_{il} \delta_{jl} dV^p \\ \int_{V^p} x_j \frac{\partial \sigma_{il}}{\partial x_l} dV^p &= \int_{V^p} \frac{\partial(\sigma_{il} x_j)}{\partial x_l} dV^p - \int_{V^p} \sigma_{ij} dV^p. \end{aligned} \quad (2.45)$$

The right hand side of equation (2.44) is

$$\begin{aligned} \int_{V^p} x_j g dV^p &= g_i \int_{V^p} x_j dV^p \\ &= 0, \text{ since } \int_{V^p} x_j dV^p = 0, \text{ as } x_j \text{ is measured from the centre of mass.} \end{aligned} \quad (2.46)$$

Inserting equations (2.45) and (2.46) in (2.44) yields

$$\begin{aligned} \int_{V^p} \frac{\partial(\sigma_{il} x_j)}{\partial x_l} dV^p - \int_{V^p} \sigma_{ij} dV^p &= 0 \\ \Rightarrow \int_{V^p} \frac{\partial(\sigma_{il} x_j)}{\partial x_l} dV^p - V^p \langle \sigma_{ij}^p \rangle &= 0 \\ \Rightarrow \langle \sigma_{ij}^p \rangle &= \frac{1}{V^p} \int_{V^p} \frac{\partial(\sigma_{il} x_j)}{\partial x_l} dV^p. \end{aligned} \quad (2.47)$$

By applying the divergence theorem to equation (2.47), the volume integral can be transformed into a surface integral.

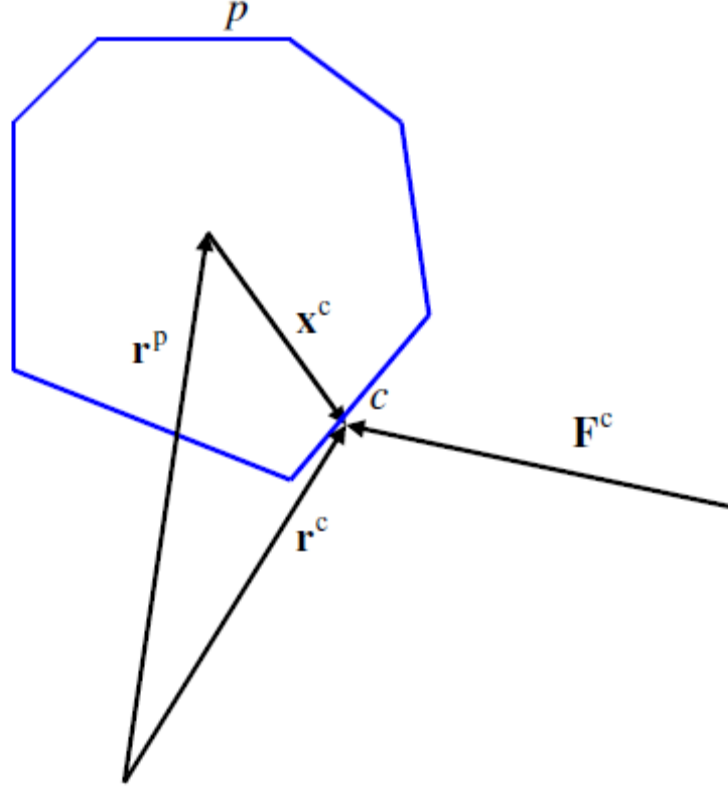


Figure 2.2: Schematic plot of a particle p with branch vector \mathbf{x}^c and the position vector \mathbf{r}^p . The branch vector \mathbf{x}^c points from the centre of mass of the particle p to contact point c .

This gives

$$\langle \sigma_{ij}^p \rangle = \frac{1}{V^p} \int_{S^p} x_j \sigma_{il} n_l dS^p. \quad (2.48)$$

$\sigma_{il} n_l = F_i$ is the traction along the surface element dS^p , a force per area, in 2D per length.

If the surface force on edge C is considered constant along the edge, we have

$$\sigma_{il} n_l \Delta S^C = F_i^c \text{ for that edge.}$$

Hence the right hand side of the equation (2.48) can be written as the sum over all contact forces.

$$\langle \sigma_{ij}^p \rangle = \frac{1}{V^p} \sum_{c=1}^{c^p} x_j^c F_i^c. \quad (2.49)$$

Since in the void space of the averaging volume element there is no stress, we just need to determine the average stress tensor over all particles whose centre of mass lies inside the averaging volume element V :

$$\langle \sigma_{ij} \rangle = \frac{1}{V} \sum_{p=1}^n V^p \langle \sigma_{ij}^p \rangle. \quad (2.50)$$

It turns out that numerically $\langle \sigma_{ij} \rangle = \langle \sigma_{ji} \rangle$ to a good approximation.

Inserting (2.49) in (2.50) we obtain a double sum given by the expression:

$$\langle \sigma_{ij} \rangle = \frac{1}{V} \sum_{p=1}^n \sum_{c=1}^{c^p} x_j^c F_i^c. \quad (2.51)$$

Equation (2.51) allows us to determine the averaged stress tensor over many polygonal particles in an averaging volume element V . We can now define the stress tensor (from (2.51)) as the dyadic product of the contact force F^c acting at the point c with the corresponding branch vector.

2.6.2 Determining strains

To a certain extent, even more interesting than to study the stress tensor is to determine the strain distribution under a sand pile. Since our study is concerned with the sand pile model, first we have to deform (relax) the sand pile in the proper way in order to obtain realistic results for the strain tensor within the sand pile. One might regard it as one of the essential questions in the field of granular heaps, how deformation under stress can be defined, aiming at the identification of a strain tensor and establishing a correlation between the stress and strain tensors in order to determine effective material properties

While the calculation of stresses is rather straightforward, this is not true for strains. In fact, even the definition of strain is problematic after assuming particles to be essentially rigid. For this reason, most macroscopic descriptions proposed in the last few years try to get by without using strain at all. Whether this approach can be successful in the long run remains to be seen. In any case, even if it may be difficult or impossible to determine strains in *experiments* on sand piles, this is not so in a *simulation*. As of now, no strains have been measured in experiments on sand piles, and continuum models assume that for sand piles displacement fields are not available. Therefore, several closure relations proposed for the equations describing sand piles [1-2] have been obtained without making use of the strain tensor.

Our original idea was to define strains with respect to a hypothetical reference state of zero gravity of a sand pile essential identical to the one at ambient gravity, except of course for slightly displaced particle centres. In this reference state, no particle rearrangements that modify neighbourhood relationships should be present in comparison with the actual state. The reference state would then be obtained from the ambient one by slowly reducing gravity. In principle, it is not necessary to go down to zero gravity, as long as the strains increase linearly with the gravity level. Instead, one may then extrapolate to zero from the knowledge of the positions of the particle centres of mass at two arbitrary different gravity levels. But it is necessary to let the sand pile approach a rest state after a reduction of gravity. Moreover, linearity has to be checked by looking at different gravity levels.

This method does not work as expected, since a reduction of gravity leads to a linear reduction only of normal stresses corresponding to the direction of gravity, i.e. σ_{yy} , but not σ_{xx} . The reason behind this is that σ_{xx} is essentially determined by horizontal static friction. Since the frictional contacts need not be fully mobilized, there is no strict proportionality between lateral forces and gravity, when we change gravity slowly, a fact leading to the destruction of the desired linearity property. In order to verify this phenomenon, first we created separately three different types of sand piles with different gravity levels (in m/s^2) of $g = 9.81$, $g = 5$ and $g = 20$ where the particles are poured from a point source, which means three sand piles constructed using the same simulation parameters except the value of gravity acceleration. We then measured numerically the

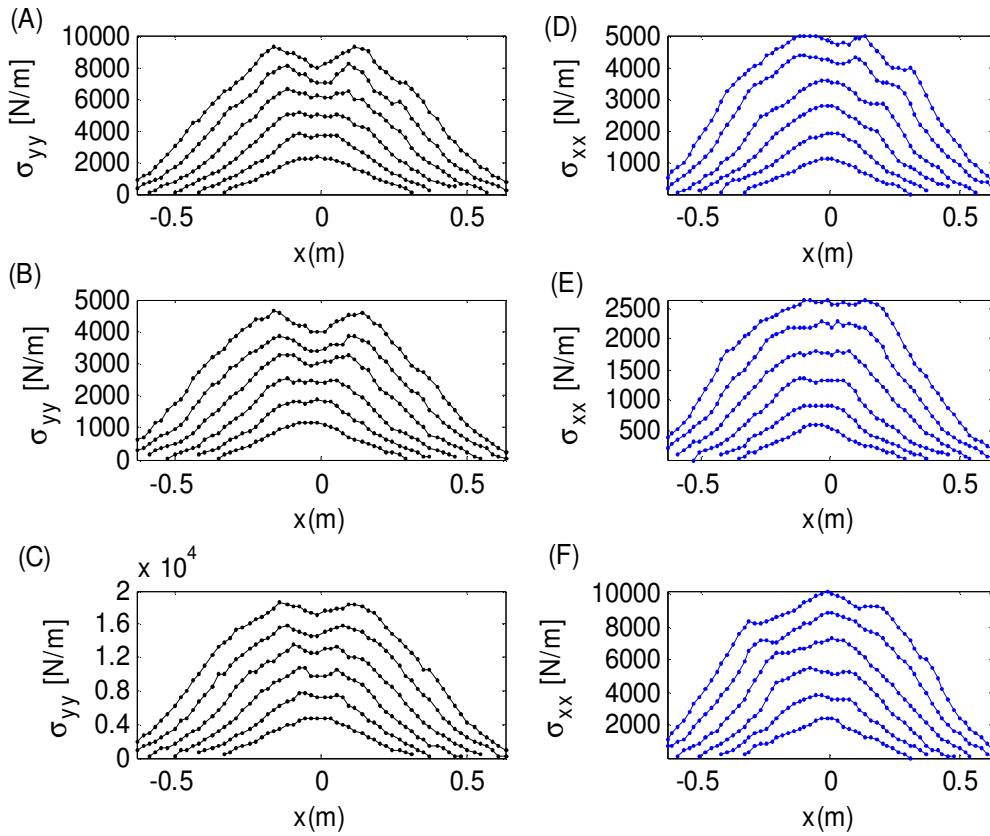


Figure: 2.3 Vertical (σ_{yy}) and horizontal (σ_{xx}) components of stress tensor at three different gravity levels of sand piles that were constructed separately by pouring particles from a point source with $g = 9.81$, $g = 5$, and $g = 20$. In panel (A) we give σ_{yy} at $g = 9.81$, in (B) σ_{yy} at $g = 5$, in (C) σ_{yy} at $g = 20$, in (D) σ_{xx} at $g = 9.81$, in (E) σ_{xx} at $g = 5$, in (F) σ_{xx} at $g = 20$.

vertical normal stress σ_{yy} and the horizontal normal stress σ_{xx} inside the resulting sand piles. They are illustrated in figure 2.3. On the left side of the figure, panels (A), (B) and (C), respectively, show the vertical normal stresses for the sand piles at $g = 9.81$, $g = 5$, and $g = 20$, and on the right side, panels (D), (E) and (F) show the corresponding horizontal normal stresses. It can be seen that in this case the vertical and horizontal normal stresses are proportional to the gravity level as expected. On the other hand, when

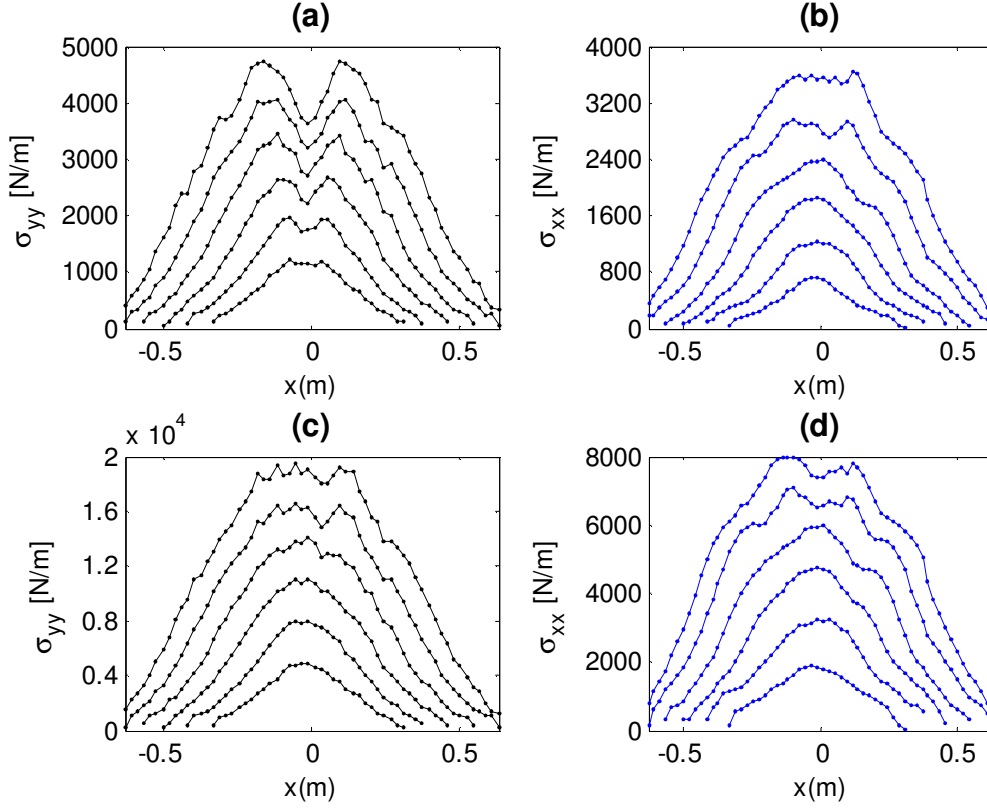


Figure: 2.4 Vertical (σ_{yy}) and horizontal (σ_{xx}) components of stress tensor at two gravity levels, first one obtained by reducing gravity from the actual state (ambient gravity level) to a state at $g = 5$, second one obtained by increasing gravity to $g = 20$. (a) σ_{yy} at $g = 5$, (b) σ_{yy} at $g = 20$, (c) σ_{xx} at $g = 5$, (d) σ_{xx} at $g = 20$. These are to be compared with panels (A) and (D) of Fig. 2.3.

we measure the stresses for a sand pile created at $g = 9.81$ after slowly changing gravity levels to $g = 5$ and $g = 20$, respectively, the vertical normal stress σ_{yy} remains proportional to gravity, but the horizontal normal stress σ_{xx} does not as the simulation result shown in figure 2.4 demonstrates. Note that the maximum of σ_{xx} changes by a factor of 2 only, that of σ_{yy} by a factor of 4, corresponding to the factor in g .

For sand piles created at different gravity levels, all three stress components ($\sigma_{yy}, \sigma_{xx}, \sigma_{xy}$) scale with gravity, indicating that the distribution of effective friction coefficients ($0 \leq \mu_{eff} \leq \mu$) and hence the degree of mobilization of contacts is the same. However, if we reduce gravity for a pile created at ambient gravity contacts not fully mobilized need not reduce their friction force and may become mobilized instead. So the

distribution of μ will shift towards higher values, σ_{xx} will be reduced by a smaller amount than proportionality would dictate. An increase of the gravity level will lead to a reduction in the degree of mobilization, shifting effective friction coefficient to smaller values.

Nevertheless, it is of course still possible to determine incremental strains, which are defined as the strain changes between the actual state and a state at a different gravity level. Using incremental stresses as well, we are then in a position to determine elastic coefficients.

We are aware of two ways given in the literature for determining an averaged strain in an assembly of grains, First the equivalent continua theories (Bagi [111], Satake [114]) and second the least-square fit theories (Cundall et al. [76], Cambou et al. [115], Liao et al. [116]). In the following section, the different versions of least-square fit strains are explained and used to determine the average strain tensor for assemblies of grains, in particular sand piles. Then the results have to be checked for consistency, i.e., we examine whether the different versions of least-square fit strains are in a good agreement with each other.

The best-fit strains are based on the idea that a translation gradient is obtained which gives the smallest deviation from the characteristic displacements of the assemblies of grains. The term characteristic displacement means the translation of the particle centre and the relative translation at the contacts. We determine the translation of the individual particle centre and relative translation of two particles at the contact by considering two different gravity levels of sand piles. One is the actual state of the sand pile at a gravity level of $g = 9.81$ and the second one is obtained by reducing gravity slowly by about 10% from the ambient gravity level of $g = 9.81$. We discuss in the following section three different kinds of least-square fit strains known as:

- The best-fit strains of Cambou et al.,
- Cundall's best-fit strain,
- The best-fit strains of Liao et al..

2.6.2.1 Cambou's best-fit strain

In our study, especially for the calculation of elastic material properties of sand piles, we used one of the simplest techniques, namely the best-fit strain of Cambou et al. [115] who consider the relative translation instead of the contact deformations and exclude the particle rotations from the analysis. The particle displacements are characterized in terms of the translations of the particle centers.

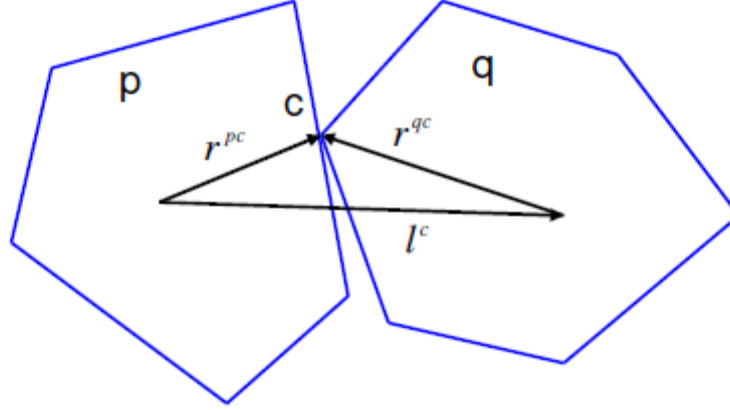


Figure 2.5: Schematic diagram of Cambou's branch vector l^c assigned to the contact c of two particles. Note that according to our preceding nomenclature r^{pc} and r^{qc} are the branch vectors.

Let us assume that two grains p and q have a contact c and du_j^p denote the translation of the centre of particle p . The relative translation of the pairs of grains p and q forming contact c is

$$d\Delta u_j^c = du_j^q - du_j^p. \quad (2.52)$$

The vectors r_i^{pc} and r_i^{qc} connect the corresponding particle centres to the contact point c and are what we called branch vectors so far. According to Cambou et al. the branch vector assigned to a contact is defined as

$l_i^c = r_i^{pc} - r_i^{qc}$, as illustrated in figure 2.5, i.e., it is simply the difference of the centre-of-mass vectors of the two particles sharing the contact c .

If every particle of the assembly of grains moves according to a (locally) uniform translation gradient tensor ε_{ji} , then the relative translation of the two particles would be

$$d\Delta u_i^c = \varepsilon_{ji} l_j^c. \quad (2.53)$$

However, usually this is not the case, and in a general case, we would have

$$d\Delta u_i^c \neq \varepsilon_{ji} l_j^c \quad (2.54)$$

for any possible uniform field ε_{ji} .

Therefore, we determine the tensor ε_{ji} for which the square sum of the deviations from (2.53) is smallest i.e, we minimize the following equation

$$Z = \sum_{c=1}^n (d\Delta u_j^c - \varepsilon_{ji} l_j^c)^2 \quad (2.55)$$

with respect to ε_{ji} , i.e., we set $\frac{\partial Z}{\partial \varepsilon_{kl}} = 0$ for every combination of subscripts k, l .

It should be noted that the sum in equation 2.55 is over all contacting pairs of particles in an averaging element. Equation (2.55) gives four equations in 2D which can be written in matrix form as follows

$$\begin{pmatrix} \sum_{c=1}^n l_1^c l_1^c & \sum_{c=1}^n l_2^c l_1^c \\ \sum_{c=1}^n l_1^c l_2^c & \sum_{c=1}^n l_2^c l_2^c \end{pmatrix} \begin{pmatrix} \varepsilon_{1i} \\ \varepsilon_{2i} \end{pmatrix} = \begin{pmatrix} \sum_{c=1}^n d\Delta u_i^c l_1^c \\ \sum_{c=1}^n d\Delta u_i^c l_2^c \end{pmatrix} \quad (2.56)$$

(i is 1 or 2).

Let z_{ij} denote the inverse of the coefficient matrix. In order to determine the ε_{11} and ε_{21} we substitute $i = 1$, for the calculation of ε_{12} and ε_{22} , $i = 2$.

The solution of (2.56) can be written in the general form

$$\varepsilon_{ij} = z_{ik} \sum_c d\Delta u_j^c l_k^c \quad (2.57)$$

$i, j, k = 1, 2$. (summation over k implied).

The tensor ε_{ij} in equation (2.57) is the best-fit translation gradient of Cambou et al.

The components of the strain tensor in two dimensions are as follows

$$\begin{aligned} \varepsilon_{xx}(x, y) &= \sum_c d\Delta u_x^c (z_{11} l_x^c + z_{12} l_y^c) \\ \varepsilon_{yy}(x, y) &= \sum_c d\Delta u_y^c (z_{21} l_x^c + z_{22} l_y^c) \\ \varepsilon_{xy}(x, y) &= \sum_c d\Delta u_y^c (z_{11} l_x^c + z_{12} l_y^c) \\ \varepsilon_{yx}(x, y) &= \sum_c d\Delta u_x^c (z_{21} l_x^c + z_{22} l_y^c) \end{aligned}$$

2.6.2.2 Cundall's best-fit strain

In this method, the strain tensor is also calculated by considering the translations of the particle centres, while particle rotations are not taken into consideration.

Let (x^p, y^p) be the coordinate of the initial position of the centre of mass of particle p in the actual state of a sand pile in a two dimensional system. The translation of the centre of particle p is denoted as (du_x^p, du_y^p) and N is the total number of particles within the averaging volume element. A particle is considered inside the volume element, if its centre of mass lies inside it.

The average of the component i of the position vectors of particle centres inside the averaging element is

$$x_i^0 = \frac{1}{N} \sum_p^N x_i^p, \quad (2.58)$$

and the average of the particle translations inside the averaging element is

$$du_i^0 = \frac{1}{N} \sum_p^N du_i^p. \quad (2.59)$$

The deviations of the individual particle positions can be calculated with:

$$\tilde{x}_i^p = x_i^p - x_i^0, \quad (2.60)$$

whereas, the relative translations of the individual particles with respect to the average translation are determined from:

$$d\tilde{u}_i^p = (du_i^p - du_i^0). \quad (2.61)$$

If each particle inside the averaging volume element moved exactly according to a uniform translation gradient tensor ε_{ij} , the relative translation of individual particle would be

$$d\tilde{u}_i^p = \varepsilon_{ji} \tilde{x}_j^p. \quad (2.62)$$

However, usually this is not the case, hence, we would not find any ε_{ij} satisfying (2.62), in short

$$d\tilde{u}_i^p - \varepsilon_{ji} \tilde{x}_j^p \neq 0 \quad (2.63)$$

for all uniform ε_{ji} .

Instead, we determine the tensor ε_{ij} for which the square sum of the deviations in (2.63) is smallest i.e, we minimize the following expression

$$Z = \sum_p \left(d\tilde{u}_i^p - \varepsilon_{ji} \tilde{x}_j^p \right)^2 \quad (2.64)$$

with respect to ε_{ji} , i.e. we set $\frac{\partial Z}{\partial \varepsilon_{kl}} = 0$ for every k, l .

Equation (2.64) provides four equations in 2D which can be expressed in a matrix form as follows

$$\begin{bmatrix} \sum_p \tilde{x}_1^p \tilde{x}_1^p & \sum_p \tilde{x}_1^p \tilde{x}_2^p \\ \sum_p \tilde{x}_2^p \tilde{x}_1^p & \sum_p \tilde{x}_2^p \tilde{x}_2^p \end{bmatrix} \begin{bmatrix} \varepsilon_{1i} \\ \varepsilon_{2i} \end{bmatrix} = \begin{bmatrix} \sum_p d\tilde{u}_i^p \tilde{x}_1^p \\ \sum_p d\tilde{u}_i^p \tilde{x}_2^p \end{bmatrix} \quad (2.65)$$

(i is 1 or 2).

Let w_{ij} denote the inverse of the coefficient matrix. In order to determine the components of strain tensor ε_{11} and ε_{21} we substitute $i=1$, whereas $i=2$ is substituted for the calculation of ε_{12} and ε_{22} .

The solution of (2.65) can be written in the general form

$$\varepsilon_{ij} = w_{ik} \sum_p d\tilde{u}_j^p \tilde{x}_k^p \quad (2.66)$$

$i, j, k = 1, 2$. (summation over k implied).

The tensor ε_{ij} in equation (2.66) is the best-fit translation gradient of Cundall et. al. The components of the strain tensor in two dimensions are as follows

$$\begin{aligned}\varepsilon_{xx}(x, y) &= \sum_p d\tilde{u}_x^p (w_{11}\tilde{x}^p + w_{12}\tilde{y}^p) \\ \varepsilon_{yy}(x, y) &= \sum_p d\tilde{u}_y^p (w_{21}\tilde{x}^p + w_{22}\tilde{y}^p) \\ \varepsilon_{xy}(x, y) &= \sum_p d\tilde{u}_y^p (w_{11}\tilde{x}^p + w_{12}\tilde{y}^p) \\ \varepsilon_{yx}(x, y) &= \sum_p d\tilde{u}_x^p (w_{21}\tilde{x}^p + w_{22}\tilde{y}^p)\end{aligned}$$

2.6.2.3 The best-fit strain of Liao et al.

This approach has been proposed by Liao et al. [116] and the definition is based on similar ideas to those of Cundall's best-fit strain and Cambou's best-fit strain, but instead of considering the particle translation, Liao et al. include both particle translation and rotation in the calculation of contact deformation.

Let us consider two particles p and q touching each other at the contact point c . The vectors r_i^{pc} and r_i^{qc} are the branch vectors joining from the particle centre to the contact point. Now, we can define the translation of pc and qc , given by

$$du_i^{pc} = du_i^p + \beta_{ijk} r_j^{pc} d\omega_k^p, \quad (2.67)$$

$$du_i^{qc} = du_i^q + \beta_{ijk} r_j^{qc} d\omega_k^q, \quad (2.68)$$

where du_i^p denotes the translation of the particle centre p , while $d\omega_i^p$ signifies rotation of the particle p about its centre. β_{ijk} is the permutation symbol.

The contact deformation dv_i^c at the contact c would be

$$dv_i^c = du_i^{qc} - du_i^{pc}. \quad (2.69)$$

In general, every particle does not move exactly according to a uniform translation gradient tensor, hence we have

$$dv_i^c - \varepsilon_{ji} l_j^c \neq 0 \quad (2.70)$$

for any uniform tensor field ε_{ij} . l_j^c is a vector joining two centres of the particle p and q , as shown in Fig. 2.5.

Similar to the case of the definition of Cundall and Cambou strain, we determine the tensor ε_{ij} for which the sum of the deviations square in (2.70) is the smallest.

Therefore, we minimize the following quantity with respect to ε_{ji} ,

$$Z = \sum_c (dv_i^c - \varepsilon_{ji} l_j^c)^2 \quad (2.71)$$

i.e. we set $\frac{\partial Z}{\partial \varepsilon_{kl}} = 0$ for every k, l .

Again we obtain four equations in 2D which can be written in a matrix form as follows

$$\begin{bmatrix} \sum_c l_1^c l_1^c & \sum_c l_2^c l_1^c \\ \sum_c l_1^c l_2^c & \sum_c l_2^c l_2^c \end{bmatrix} \begin{bmatrix} \varepsilon_{1i} \\ \varepsilon_{2i} \end{bmatrix} = \begin{bmatrix} \sum_c dv_i^c l_1^c \\ \sum_c dv_i^c l_2^c \end{bmatrix} \quad (2.72)$$

$i = 1, 2$.

The solution of (2.72) can be written in the general form

$$\varepsilon_{ij} = z_{ik} \sum_c dv_j^c l_k^c \quad (2.73)$$

$i, j, k = 1, 2$. (summation over k implied).

where z_{ij} denotes the inverse of the coefficient matrix on the left-hand side of (2.73).

The components of the strain tensor in two dimensions are as follows

$$\varepsilon_{xx}(x, y) = \sum_c dv_x^c (z_{11} l_x^c + z_{12} l_y^c)$$

$$\varepsilon_{yy}(x, y) = \sum_c dv_y^c (z_{21} l_x^c + z_{22} l_y^c)$$

$$\varepsilon_{xy}(x, y) = \sum_c dv_y^c (z_{11} l_x^c + z_{12} l_y^c)$$

$$\varepsilon_{yx}(x, y) = \sum_c dv_x^c (z_{21} l_x^c + z_{22} l_y^c)$$

2.6.2.4 Derivative method

In this section, we derive a formula for the strain tensor by using the derivative of the particle displacement, which means the particle rotations are not included for the calculation of the strain tensor. Given the particle displacements we can calculate the strain tensor. The displacement vector of a single particle reads

$$u_i = x_i - x'_i, \quad (2.74)$$

where x_i is the initial position of the centre of mass of particle i and x'_i is the final position of the centre of mass of the particle after applying an overload to the sample. Then, we take an average over individual displacements of the particles inside the volume element to determine a continuous displacement field as a function of the point position (x,y) .

$$u_i(x,y) = \frac{1}{n} \sum_{i=1}^n u_i. \quad (2.75)$$

The sum is over the particles in a averaging volume element centered at (x,y) . This procedure allows us to determine the components strain tensor at the point considered. The simplest approximation for the three components of the strain tensor in two dimensions (which are linear combinations of derivatives of the displacements) is as follows

$$\begin{aligned} u_{yy}(x,y) &= \frac{u_y(x,y+h_y) - u_y(x,y)}{h_y} \\ u_{xx}(x,y) &= \frac{u_x(x+h_x,y) - u_x(x,y)}{h_x} \\ u_{xy}(x,y) &= \frac{0.5(u_x(x,y+h_y) - u_x(x,y))}{h_y} + \frac{0.5(u_y(x+h_x,y) - u_y(x,y))}{h_x} \end{aligned} \quad (2.76)$$

where h_x and h_y are the distances between the centres of the neighbouring averaging volume element along the x and y directions and the current one, respectively.

2.6.3. Inertia tensor field for assemblies of polygonal particles

In this section, we derive a formula for the inertia tensor field of a granular system consisting of polygonal particles. We already have discussed in chapter one the shapes of the particles that affect the pressure distribution under a sand pile, therefore, one has to clarify the question of the orientation distribution of the particles inside sand piles with different degrees of poly-dispersity. Moreover, we have to check how the orientation distribution of the particles influences the decrease of the pressure in the centre of the heap. By defining a local inertia tensor field, we obtain a measure for the orientation of non circular particles.

2.6.3.1 Inertia tensor for a single particle

For a rigid body, one can define three independent components of the inertia tensor for two-dimensional systems with the following relation:

$$\left. \begin{aligned} \theta_{xx} &= \int y^2 da \\ \theta_{yy} &= \int x^2 da \\ \theta_{xy} &= -\int xy da \end{aligned} \right\} \quad (2.77)$$

where the integration is over the area of the particle and homogeneity of the mass distribution of the particle has been assumed.

From the Stokes theorem, we know

$$\int_A (\nabla \times u) \cdot d\mathbf{a} = \oint_{\partial A} u \cdot ds. \quad (2.78)$$

$$\begin{aligned} \text{In two dimensions, } u &= u_x(x, y)e_x + u_y(x, y)e_y \\ \Rightarrow \nabla \times u &= (\partial_x u_y - \partial_y u_x)e_z. \end{aligned} \quad (2.79)$$

Substitute $u_y(x, y) = xy^2$ and $u_x(x, y) = 0$ in equation (2.79), which yields

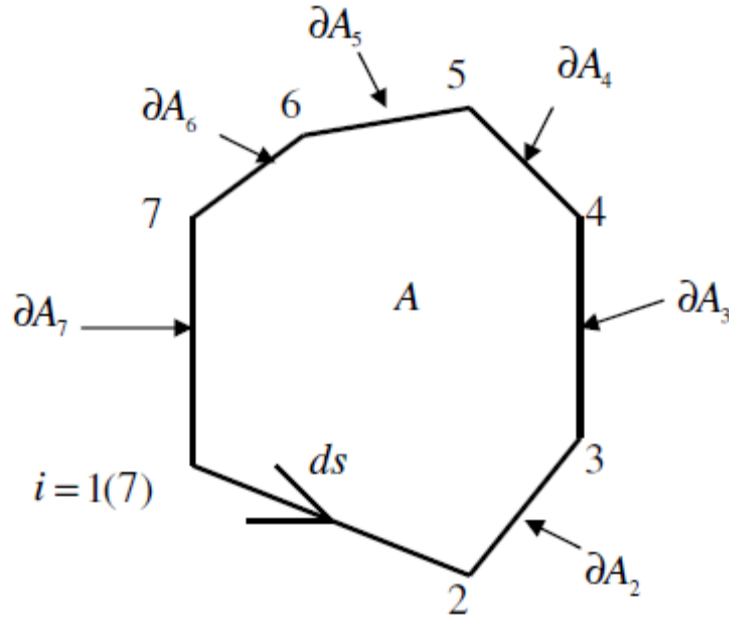


Figure 2.6: Schematic diagram of polygon with 7 corners.

$$\nabla \times u = y^2 \mathbf{e}_z. \quad (2.80)$$

Then, we can obtain θ_{xx} for

$$\theta_{xx} = \int_A y^2 da = \int_A y^2 \mathbf{e}_z d\mathbf{a} = \oint_{\partial A} xy^2 \mathbf{e}_y ds = \oint_{\partial A} xy^2 dy. \quad (2.81)$$

$$\begin{aligned} \theta_{xx} &= \sum_i \int_{\partial A_i} xy^2 dy \\ &= \sum_i \int_{\partial A_i} \frac{y - b_i}{m_i} y^2 dy. \end{aligned}$$

Since along ∂A_i as shown in the Fig. 2.6, $y = m_i x + b_i$,

$$\begin{aligned} m_i &= \frac{y_{i+1} - y_i}{x_{i+1} - x_i}, b_i = \frac{y_{i+1}x_i - y_i x_{i+1}}{-(x_{i+1} - x_i)} \\ &= \sum_i \frac{1}{m_i} \left(\frac{y^4}{4} - b_i \frac{y^3}{3} \right)_{y_i}^{y_{i+1}} = \sum_i \frac{1}{4m_i} (y_{i+1}^4 - y_i^4) - \frac{b_i}{3m_i} (y_{i+1}^3 - y_i^3) \end{aligned}$$

$$= \sum_i \frac{1}{12} (y_{i+1}x_i - x_{i+1}y_i) (y_{i+1}^2 + y_{i+1}y_i + y_i^2). \quad (2.82)$$

Alternatively, we may write

$$\theta_{xx} = \sum_i \frac{1}{12} (x_i - x_{i+1}) (y_{i+1}^2 + y_i^2) (y_i + y_{i+1}). \quad (2.83)$$

Similarly, we can derive the other two components of inertia tensor.

Setting $u_y(x, y) = \frac{x^3}{3}$ and $u_x(x, y) = 0$ in equation (2.79), we obtain

$$\nabla \times u = x^2 e_z. \quad (2.84)$$

Then, the second equation of the set of expression (2.77) becomes

$$\theta_{yy} = \int_A x^2 da = \int_A x^2 \mathbf{e}_z d\mathbf{a} = \oint_{\partial A} \frac{x^3}{3} \mathbf{e}_y ds = \oint_{\partial A} \frac{x^3}{3} dy. \quad (2.85)$$

$$\begin{aligned} \theta_{yy} &= \sum_i \oint_{\partial A_i} \frac{x^3}{3} dy \\ &= \sum_i \frac{1}{3} \oint_{\partial A_i} x^3 m_i dx = \sum_i \frac{1}{12} m_i (x^4)_{x_i}^{x_{i+1}} \\ &= \sum_i \frac{1}{12} m_i (x_{i+1}^4 - x_i^4) = \sum_i \frac{1}{12} m_i (x_{i+1} - x_i) (x_{i+1} + x_i) (x_{i+1}^2 + x_i^2) \\ &= \frac{1}{12} \sum_i (y_{i+1} - y_i) (x_{i+1} + x_i) (x_{i+1}^2 + x_i^2). \end{aligned} \quad (2.86)$$

Rewriting equation (2.86) a little, we obtain the analog of (2.82)

$$\theta_{yy} = \frac{1}{12} \sum_i (y_{i+1}x - y_i x_{i+1}) (x_i^2 + x_i x_{i+1} + x_{i+1}^2). \quad (2.87)$$

In order to determine θ_{xy} , we substitute $u_y(x, y) = -\frac{x^2 y}{2}$ and $u_x(x, y) = 0$ in equation (2.79), which gives

$$\nabla \times u = -xy e_z. \quad (2.88)$$

Then, the third equation of the set of expression (2.77) becomes

$$\theta_{xy} = \int_A -xy da = \int_A -xy \mathbf{e}_z \mathbf{d}\mathbf{a} = -\oint_{\partial A} \frac{1}{2} x^2 y \mathbf{e}_y ds = -\frac{1}{2} \oint_{\partial A} x^2 y dy. \quad (2.89)$$

$$\begin{aligned} \theta_{xy} &= -\frac{1}{2} \oint_{\partial A_i} x^2 y dy \\ &= -\frac{1}{2} \sum_i \oint_{\partial A_i} x^2 (m_i x + b_i) m_i dx = -\frac{1}{2} \sum_i m_i \oint_{\partial A_i} (m_i x^3 + b_i x^2) dx \\ &= -\frac{1}{2} \sum_i \left[\frac{1}{4} m_i^2 (x_{i+1}^4 - x_i^4) + \frac{m_i b_i}{3} (x_{i+1}^3 - x_i^3) \right] \\ &= \sum_i \left[\frac{1}{8} m_i (m_i (x_{i+1} - x_i)) (x_{i+1} + x_i) (x_{i+1}^2 + x_i^2) - \frac{b_i}{6} m_i (x_{i+1} - x_i) (x_{i+1}^2 + x_{i+1} x_i + x_i^2) \right] \\ &= \sum_i \left[-\frac{1}{8} (y_{i+1} - y_i) (m_i x_{i+1} + m_i x_i) (x_{i+1}^2 + x_i^2) - \frac{b_i}{6} (y_{i+1} - y_i) (x_{i+1}^2 + x_{i+1} x_i + x_i^2) \right] \\ &= \sum_i \left[-\frac{1}{8} (y_{i+1} - y_i) (m_i x_{i+1} + b_i + m_i x_i + b_i) (x_{i+1}^2 + x_i^2) + \frac{1}{4} (y_{i+1} - y_i) (b_i) (x_{i+1}^2 + x_i^2) \right. \\ &\quad \left. - \frac{b_i}{6} (y_{i+1} - y_i) (x_{i+1}^2 + x_{i+1} x_i + x_i^2) \right] \\ &= \sum_i \left[-\frac{1}{8} (y_{i+1} - y_i) (y_{i+1} + y_i) (x_{i+1}^2 + x_i^2) + \frac{1}{12} (y_{i+1} - y_i) \left(\frac{y_{i+1} x_i - y_i x_{i+1}}{x_i - x_{i+1}} \right) (x_{i+1} - x_i)^2 \right] \\ &= -\frac{1}{24} \sum_i [(x_i y_{i+1} + x_i y_i) + (x_i + x_{i+1})(y_i + y_{i+1})] (x_i y_{i+1} - x_{i+1} y_i). \quad (2.90) \end{aligned}$$

$$\theta_{xy} = -\frac{1}{24} \sum_i [(x_i y_{i+1} + x_{i+1} y_i) + (x_i + x_{i+1})(y_i + y_{i+1})] (x_i y_{i+1} - x_{i+1} y_i). \quad (2.91)$$

2.6.3.2 Averaged inertia tensor field

Equations (2.83), (2.87) and (2.91) allow us to determine the components of the inertia tensor of a particle p . Then it is easy to determine the formula for the average of this inertia tensor over many particles in a representative volume element. Let us denote by θ_{ij}^p the inertia tensor of the single particle p , we then determine the inertia tensor average $\langle \theta_{ij} \rangle$ in an averaging element with size of volume V via:

$$\langle \theta_{ij} \rangle = \frac{1}{V} \sum_{p=1}^n V^p \theta_{ij}^p. \quad (2.92)$$

2.6.4 Fabric tensor

The density distribution is not homogeneous under a sand pile poured from a point source. Therefore, it may be assumed that the internal texture of the pile is important. Furthermore, forces are propagated from one particle to the neighbour particles in an assembly of grains only via the contacts point of the particle. Thus, for the quasi-static mechanics of granular aggregates, it is useful necessary to have a description of the associated contact network of the inter-particle contacts.

A particular quantity besides the local inertia tensor field that describes the internal texture of the granular assembly is the so-called fabric tensor. Various definitions of the fabric tensor exist in the literature [117-124] including definitions for elliptical, spherical or polygonal particles. In our study, we consider non-spherical particles so we employ here a mathematical formulation for the fabric tensor, in which the branch vector itself is used to define a unit vector in the direction towards the contact, because here the simplest way of characterizing the packing network is via the branch vectors connecting the particle centres of mass with their contacts.

Once we have the contact points of the individual particles, we can calculate a fabric tensor for each particle, which yields an additive contribution to the overall fabric tensor. The latter then is a volume average over many particles. After defining the fabric tensor for one particle and for an aggregate of grains, we will demonstrate how it may be used to examine for isotropy of the granular structure of a material. The fabric tensor measures the contact number density in a given direction in the assembly. Therefore, it may be used to examine whether the grains of the material are placed in an isotropic way or whether there exists any directional ordering.

2.6.4.1 The fabric tensor for one particle

We derive here the mathematical formulation for the fabric tensor of a polygonal particle. The formula for the fabric tensor is given [117-118] by

$$F_{ij}^p = \sum_c n_i^c n_j^c, \quad (2.93)$$

where n_i^c is the i th component of the unit vector to contact point c of the considered particle p , as shown in Fig.2.7.

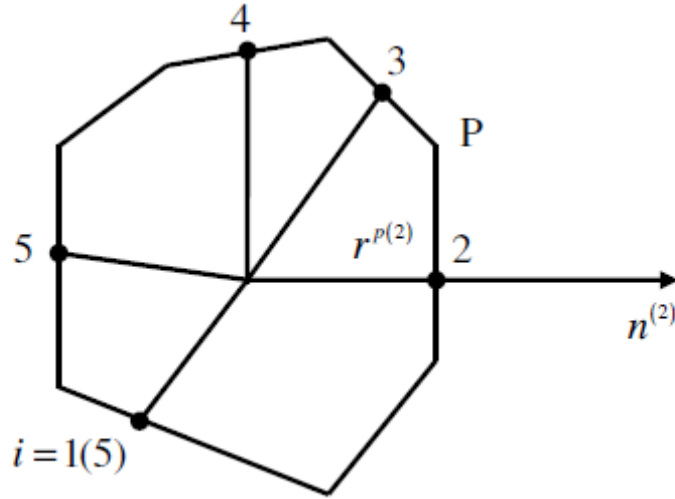


Figure 2.7: Schematic plot of a polygonal particle p with five contact points. The branch vector r^{pc} and the unit vector n^c are shown at contact point $c = 2$.

$$n_x^c = \frac{x_c - x_p}{\sqrt{(x_c - x_p)^2 + (y_c - y_p)^2}}, \quad (2.94)$$

$$n_y^c = \frac{y_c - y_p}{\sqrt{(x_c - x_p)^2 + (y_c - y_p)^2}},$$

where (x_c, y_c) and (x_p, y_p) are the contact point and the centre of mass, respectively, and the sum in (2.93) is over all the contacts of the particles.

The trace of the fabric tensor then determines the number of contacts of particle p

$$tr(F_{ij}^p) = \sum_c n_i^c n_j^c = C^p. \quad (2.95)$$

2.6.4.2 The fabric tensor for many particles

We take an average over many particles in a representative volume element (RVE) in order to determine the average fabric tensor that describes the contact network in a given volume V .

The averaged fabric tensor over many particles is given by

$$\langle F_{ij} \rangle_V = \frac{1}{V} \sum_p V^p F_{ij}^p, \quad (2.96)$$

where V is the volume of the RVE that contains the particles whose centre of mass lies inside it and V^p and F_{ij}^p respectively denote the volume and the fabric tensor of particle p .

2.7 Averaging procedure

One can obtain detailed information about measurable quantities such as forces, stresses, and displacements of an individual particle from the discrete element simulation. However, the behaviour of an individual particle is not significant for the behaviour of the whole system, as most of the measurable microscopic quantities in granular material vary strongly as a function of position.

In this regard, one common example is the stress tensor, which is not constant across grains (microscopic level), but usually it shows its largest values for particles with a large number of contacts. Moreover, the microscopic stress tensor would not be a convenient means to describe the macroscopic sand pile, as it fluctuates widely within a volume containing a few sand grains. In fact, it is zero in the voids between grains. Hence for a continuum description, we need to average microscopic stresses over suitable domains, which will reduce the relative fluctuations. In order to suppress the fluctuations, we need to perform averages over sufficiently many particles in an averaging volume element. But, the question is how many particles are actually required to determine the average macroscopic tensorial quantities, which means, one has to determine the number of particles (or appropriate size of the volume element) providing realistic results for the macroscopic stress tensor and also for other macroscopic tensorial quantities including fabric, strain, and volume fraction of the sand pile.

In our work, averages are performed by introducing a representative volume element (RVE) via the requirement that the average becomes size independent, if the volume is taken equal to this value or larger. The RVE averaging strategy is used by many engineers to obtain scalar and tensorial quantities, especially in problems that deal with particulate materials.

Averaging over different volumes gives different results, as long as the volume element is too small. As we increase the size of the volume element in the computation of the average, the latter converges to a certain value. A size of the volume element near but above the minimum needed for convergence gives the representative volume element to be used in evaluations of stress and other fields.

We have taken into account those particles whose centres of mass lie inside the averaging volume element to determine the macroscopic stress tensor. Sometimes, this method is referred to as the particle centre averaging technique. It is noted that the results of the macroscopic stress tensor were obtained by taking averages over many particles that correspond to the middle region of the sand pile. The simulation results for the individual components of the stress tensor against the number of particles are displayed in Fig. 2.8.

The number of particles shown in the graph corresponds to the size of the volume element. The blue curve connecting square symbols represents the vertical normal stress tensor, whereas the red and black curves represent the horizontal and shear stresses, respectively. It can be seen in the figure that all the components of the stress tensor are converged approximately at the same number of particles. We find that a size of the volume element containing 100-200 particles is sufficient to serve as RVE.

On the other hand, we determine the size of the RVE for the strain tensor as well as for the fabric tensor. Fig. 2.9 displays the RVE for the strain tensor and the one for the fabric tensor is illustrated in Fig. 2.10. We find from the figure that the size of the volume element is the same as for the stress tensor. We have not determined individually the size of RVE for the inertia tensor fields. It should be noted that the size of the volume element that we consider for the calculation of the stress, fabric and strains is same as for the inertia, elastic constants and volume fraction of the sand pile.

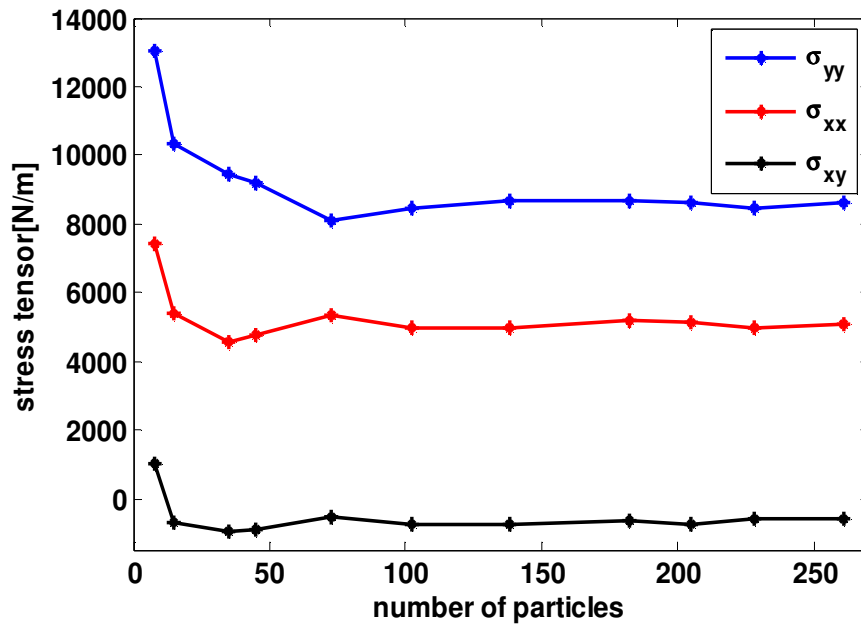


Figure 2.8: Representative volume element (RVE) for stress tensor. The volume element was located in the centre and near the bottom of the sand pile.

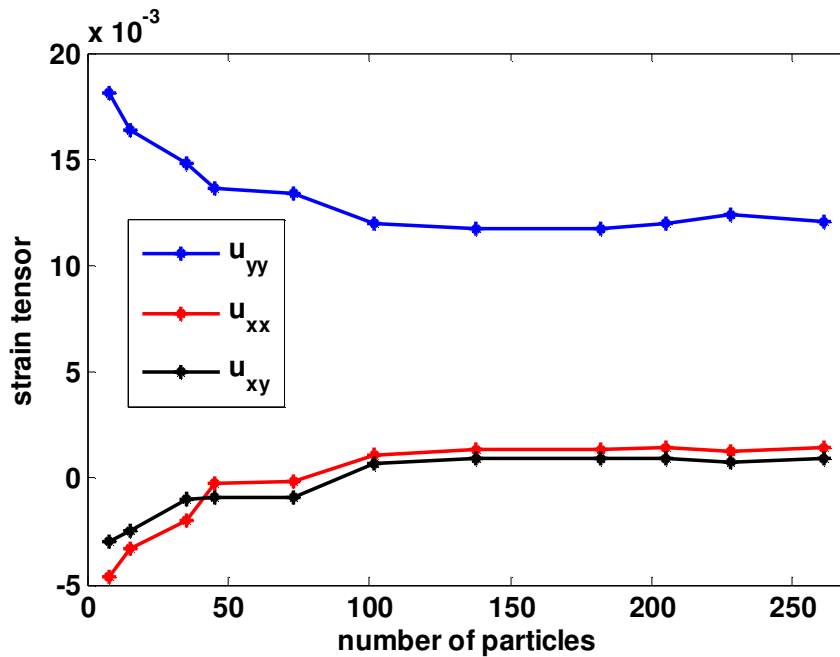


Figure 2.9: Representative volume element (RVE) for strain tensor.

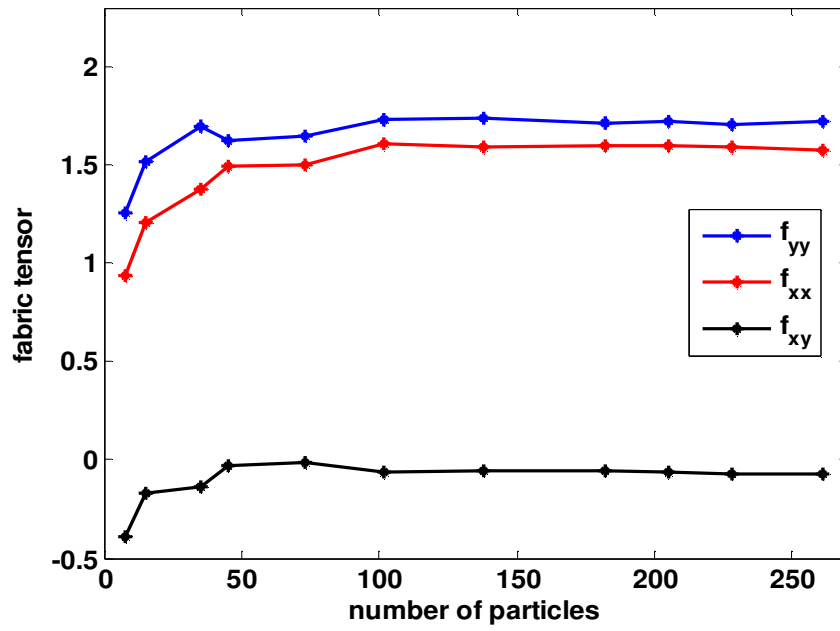


Figure 2.10: Representative volume element (RVE) for fabric tensor.

3

Simulation results

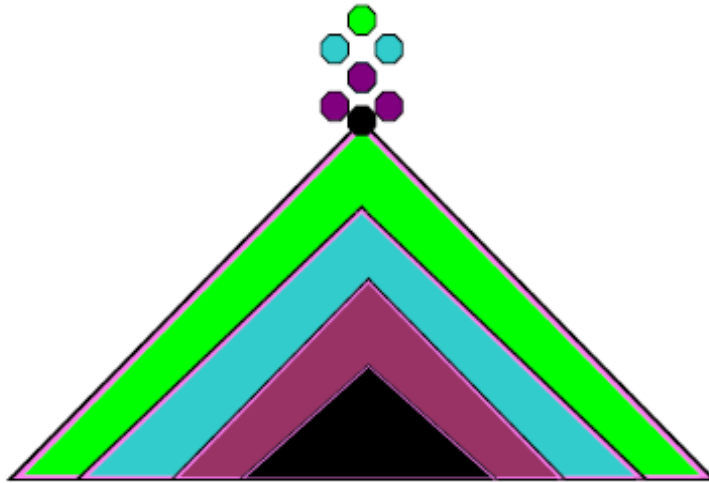
In this chapter, we present the numerical results on effective material properties of two dimensional sand piles of soft convex polygonal particles using the discrete element method (DEM). We focus primarily on discussing the simulation results of the microscopic force distribution, and then show how the shape of the particles and construction history of the piles affects the pressure distribution under a sand pile. In addition, other measurable macroscopic tensorial quantities including strain, fabric distributions, and orientation of the particles inside a sand heap obtained from simulations are discussed.

We first give in the following a short description how the sand pile is constructed from two different types of procedures. We then measure averaged stress and strain, the latter via imposing a 10% reduction of gravity, as well as the fabric tensor. Then, we compare the vertical normal strain tensor between sand piles qualitatively and show how the construction history of the piles affects their strain distribution. The simulation results of volume fraction of sand piles are compared qualitatively with the existing experimental results in the literature. In the next step, the elastic constants are measured assuming Hooke's law to be valid in relating incremental stress and strain tensors to each other. We then determine correlation between the measured elastic material constants and the trace of the fabric tensor, and between invariants of the incremental stress and strain tensors for a small change in gravity.

3.1 Method of preparation of the sand pile

One can construct a sand pile in many different ways. Here, we restrict ourselves to two different approaches. The first consists in pouring the material from a funnel with a small outlet, known as “point source”; and the second, pouring the material in a uniformly dis-

A.



B.

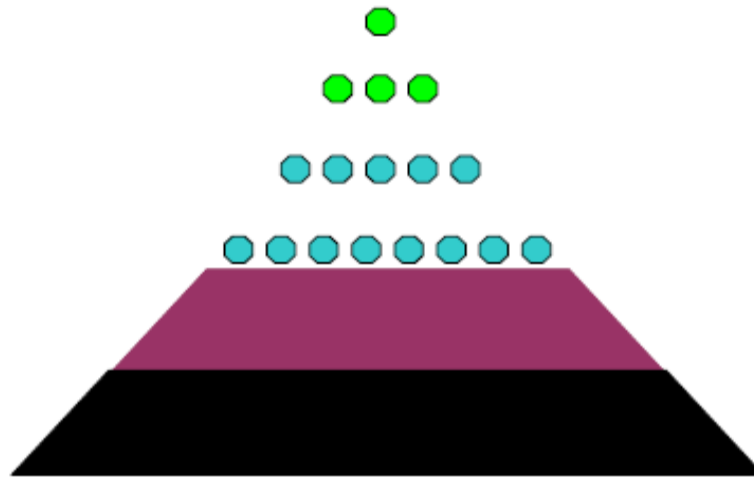


Figure 3.1.A-B: Schematic diagrams for possible construction procedures of the sand pile. **A.** Particles are dropped onto the apex of the pile, **B.** Particles are dropped in a uniform distribution on each layer of the pile.

tributed way, from a so-called “line source”. Note that the line source is reduced in length during the procedure so as to have a length equal to or slightly smaller than that of the top plateau of the pile at any instant of time. When a pile is constructed from a point source, the particles are dropped always onto the apex of the sand pile and roll down the slopes of the pile, as shown in Fig. 3.1.A. On the other hand, when a sand pile is constructed from a line source procedure, the particles are dropped in a layer wise manner, and

slowly from a height of slightly greater than one particle diameter onto the already present layer, as shown in Fig. 3.1.B.

In order to investigate the microscopic force structure and macroscopic distributions of quantities such as stress, strain, inertia and fabric under a sand pile, and to check how the construction history of the granular aggregates influences their pressure, and strains distribution, we perform numerical simulations in which sand piles are constructed from either a point source or a line source. In the followings we explain in detail how we construct two different types of sand piles from two different qualitative procedures.

3.1.1 Sand piles from a point source

We constructed a sand pile from several thousands of convex polygonal particles with varying shapes, sizes and edge numbers where the particles were dropped from a point source. The particles were dropped on to the system from 50 cm height with initial velocity of 0.2 m/s and the time for the generation of the new particle is 0.1s at the same position. We have constructed 14 sand piles using a point source. The individual simulations differ only by the initialization of the random number generator for the generation of particles. The number of polygon edges varies from six to eight for each simulation. The particle corners are placed randomly on an ellipse (RAND1), see in ref. [103]. The radius of the particles is 2.75 mm and degree of poly-dispersity of the particles is about 30%.

The average angle of repose for 14 sand piles was approximately 28° by taking the average over the left and right base angles. A snapshot of one of the simulated sand piles constructed from a point source is illustrated in Fig. 3.2. Different colour corresponds to particles dropped at different times. We used a flat bottom ground plate. The walls and the funnel are made of immobile specially shaped particles and the bottom ground plate is fixed in shape as well, hence effects that may spoil real-world experiments such as ground plate bending [125] or compression [20], when the grains are deposited are excluded. The characteristic properties of the ground plate, side walls and funnel are equal to the particles properties, which mean the Young's modulus of elasticity of the bottom ground wall is the same as for the particles, and the static friction coefficient between the bottom ground wall and the particles is the same as between the particles.

3.1.2 Sand piles from a line source

Next, we constructed sand piles from a line source that consisted of around 6500 particles. The dropping height of each new layer from the already present layer of the system is 8 mm and particles are dropped uniformly onto the already present layer. The size, shape of the particles and the time for the generation of the new particle we used for

constructing a sand pile from a line source are the same as that for the point source case. The corner number of each particle is 7, and the degree of poly-dispersity of the particle is 10%. The positions of corner are placed randomly on an ellipse (RAND1). The measured average angle of repose of 11 sand piles is about 27° . Fig. 3.3 displays one of the simulated sand piles that was constructed from a line source. The simulation parameters and their values used for the construction of sand piles are given in the following table.

Name of variable	Value
Static friction	0.54
Dynamic friction	0.54
Particle density	5000 kg/m^2
Young's modulus	10^7 N/m
Damping coefficient	0.75
Time step	$2 \times 10^{-6} \text{ s}$
Size of poly-dispersity (point source)	30%
Size of poly-dispersity (line source)	10%
Initial velocity of the particles	0.2 m/s
Particle radius	2.75 mm
Cohesion coefficient	0
Acceleration	9.81 m/s^2
Position of particle corner	RAND1
Number of corners(point source)	(6,8)
Number of corners(line source)	7

Table 2: Parameters used for the DEM simulation of the sand pile.

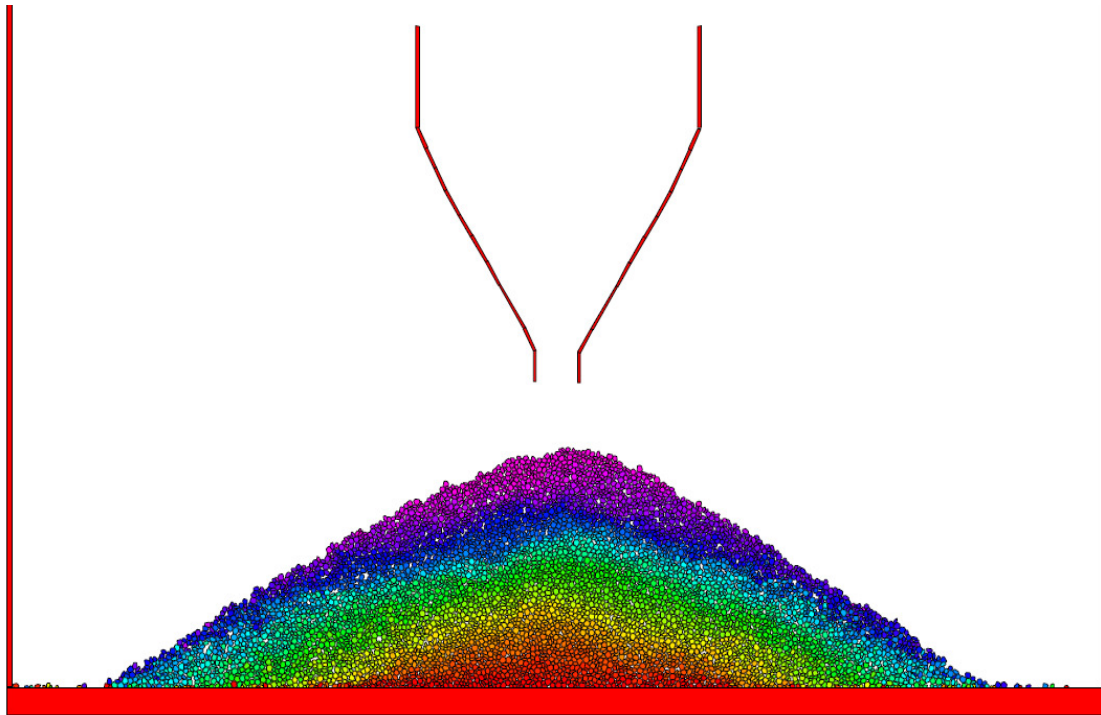


Figure 3.2: Snapshot for a simulated sand pile constructed from a point source with 30% poly-disperse mixture of particles.

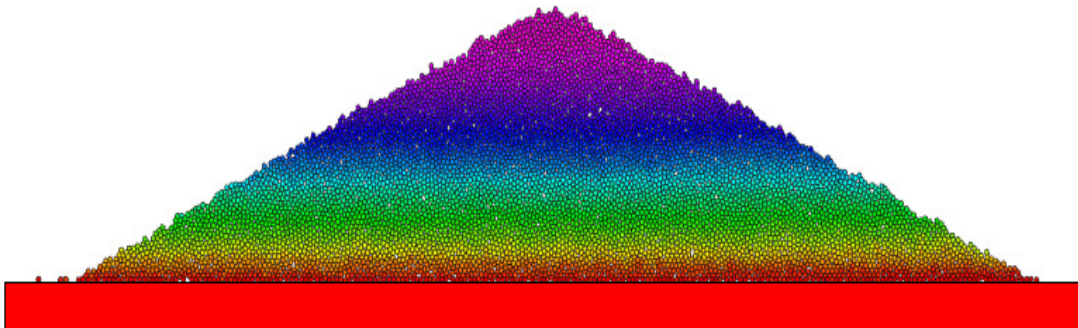


Figure 3.3: Snapshot for a simulated sand pile constructed from a line source with 10% poly-disperse mixture of particles.

3.2 Microscopic force distribution

We determine the force network inside a sand pile constructed from a line source. Fig. 3.4 displays the simulation results of the force network for a line source sand pile that contains a mixture of roundish particles. The line thickness represents the magnitude (strength) of the force. The darker and wider a line the stronger the force it represents. As can be seen in the figure, the force network varies as a function of the position in the pile. We observe that in the heap of granular assemblies, the stronger force chains appear at the middle region and weaker force chains near the free surface of the pile.

We then determine the force network of sand piles constructed from a point source consisting of a mixture of roundish particles. The result obtained from the simulation is illustrated in Fig. 3.5. It can be seen from the figure that there are no extremely strong force chains appearing in the central region, indicated as a red line, for a sand pile constructed from a point source.

Moreover, we compare the force network between sand piles that contain a mixture of round particles with sand piles consisting of a mixture of elliptic particles. Since our simulations are two-dimensional, we cannot simulate realistic particle shapes, but we try to mimic the difference between roughly spherical particles and ellipsoidal particles by working with almost circular particles on the one hand and nearly elliptic ones on the other hand. We have determined the force distribution for a pile of a mixture of elliptic particles with the simulation result represented in Fig. 3.6. Clearly, many more strong force chains can be seen for piles of elliptic particles than for round particles. The force chain structure appears open for piles of round particles and more complex for piles of elliptic particles.

The force networks obtained in our simulations are compared with the recent experimental results obtained by I. Zuriguel et al. [11]. The experiments were conceived for an essentially two-dimensional situation and the particles were made from photo elastic polymer material. The particles were cut from sheets of the polymer material using a high precision computer controlled water jet which enabled them to choose distinct shapes for the particles. Two shapes of particles, namely disks and elliptic cylinders were used for the construction of the sand pile. Qualitatively similar results were obtained for the force distribution under the piles from the experimental investigation, as shown in Fig. 1.10.

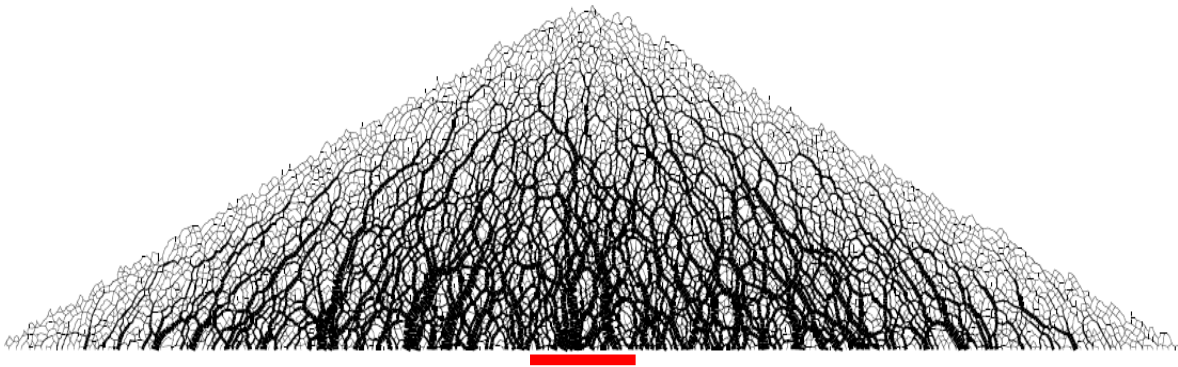


Figure 3.4: Simulation result giving the force network for a sand pile constructed from a line source with round particles.

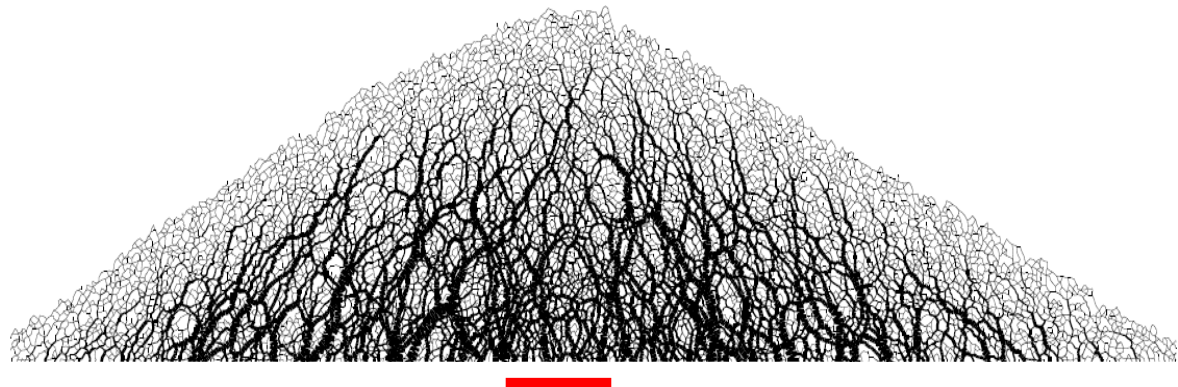


Figure 3.5: Simulation result giving the force network for a sand pile constructed from a point source with round particles.

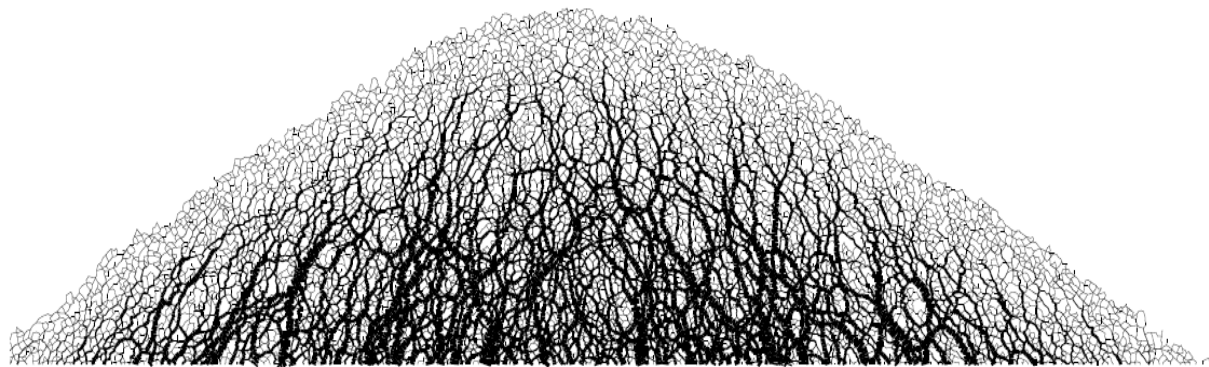


Figure 3.6: Simulation result giving the force network for a sand pile constructed from a point source with elliptic particles.

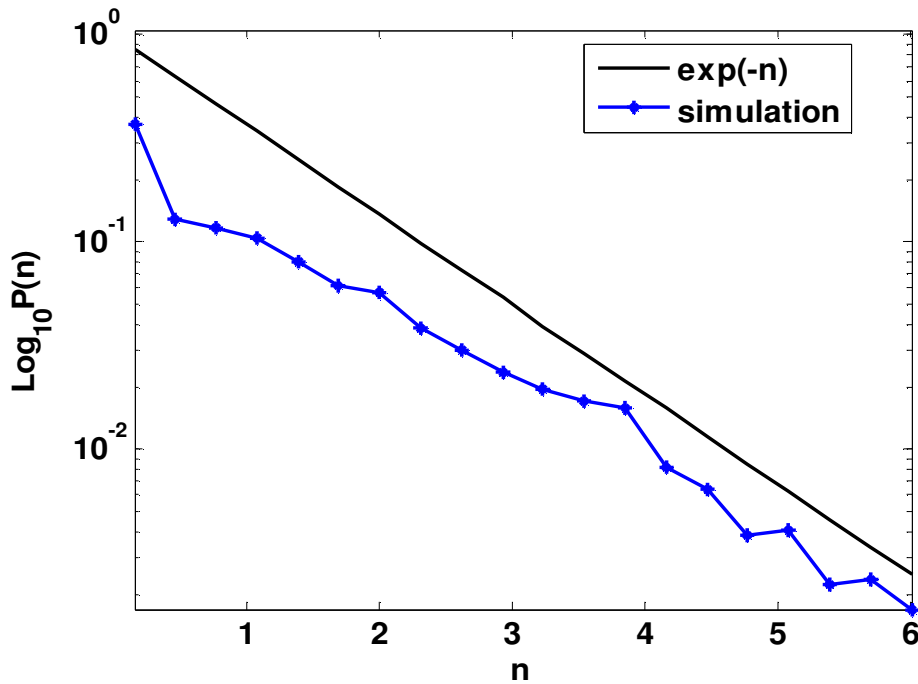


Figure 3.7: Numerical results of the probability distribution of the normalized vertical force at the bottom layer of the sand pile.

In order to see the behaviour of the forces inside the pile, we calculate the probability distribution P for vertical forces N for the particles at the lowermost layer of the sand pile built by pouring them from a point source. Vertical force is normalized by its mean value \bar{N} , which is denoted as $n = N/\bar{N}$. We represent in figure 3.7 the simulation results of the logarithm (base 10) of the probability distribution $P(n)$ of the normalized vertical force against the normalized force n itself. The figure shows that, for forces greater than the mean ($n > 1$), the probability distribution of vertical force decays exponentially (a similar behaviour was obtained for the ‘q model’ in the case of large forces) and that the distribution flattening out near the mean force ($n \approx 1$) whereas there is a slight increase in $P(n)$ as n decreases towards zero.

Qualitatively similar results were obtained for the probability distribution of the vertical normal stress near the bottom of sand piles in the absence of friction by Luding in ref. [20].

3.3 Pressure distribution under a sand pile

In this section, first, the simulation results of the averaged stress tensor for the sand piles constructed by two qualitatively different procedures are discussed. Then in the next step, we compare our numerical simulation results of stress distributions with the available experimental results.

The simulation results of the normalized vertical normal stress tensor of a single sand pile consisting of a mixture of round particles is illustrated in Fig. 3.8. The figure demonstrates that there are large fluctuations in the stress tensor for single sand pile. The stress tensor is normalized by the hydrostatic static pressure, ρgh , where the quantities ρ and h denote the density and the height of the sand pile, respectively, and g is the acceleration due to gravity.

The averaged stress tensor was evaluated throughout the sand pile; typically, we represent it via a plot of stress tensor components as a function of the lateral coordinate x of the pile for layers of given heights y_1, y_2, \dots, y_n . The averaged vertical normal stress tensor obtained from DEM simulations is displayed in Fig. 3.9 for sand piles that were constructed from a point source. The figure demonstrates that the vertical normal stress distribution changes with the vertical position in the sand pile. We find a pressure dip below the apex of the sand pile which appears not only at the bottom layer of the sand piles but also exists up to a certain height inside sand piles (but not above).

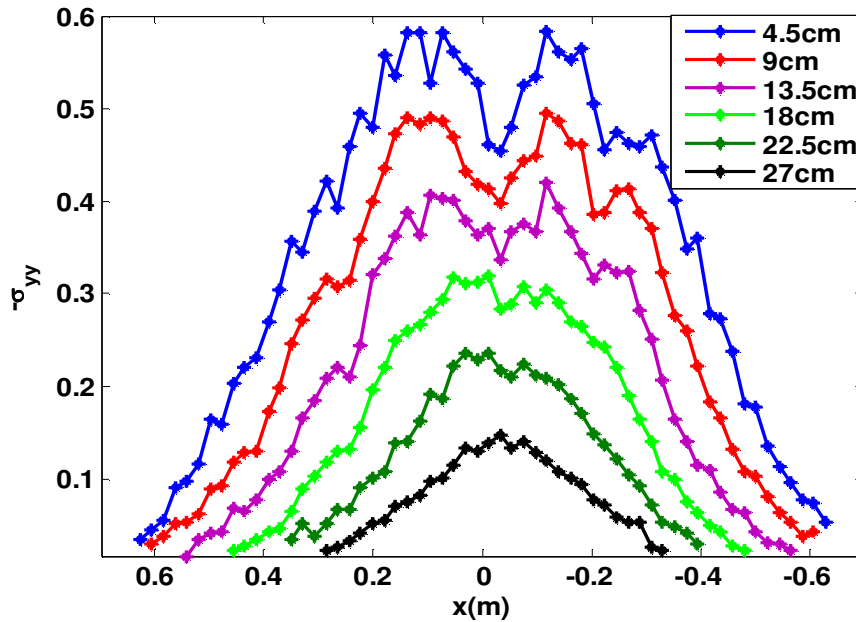


Figure 3.8: Simulation result for the normalized vertical (negative) normal stress tensor of a single sand pile at different heights inside the pile constructed from a point source (height of the sand pile is 33.5 cm).

On the other hand, the simulation results for the averaged negative vertical normal stress tensor of the sand pile constructed from a line source is shown in Fig. 3.10, which demonstrates that there is no stress dip below the apex of the sand pile and it has plateau like behaviour at the centre. We notice that, even if simulating the sand pile from a line source with large poly-dispersity mixture of the particles (around of 30%) no dip exists in the pressure profile.

Then, we compare numerical simulation results of stress distributions with the results obtained by experimental measurement [10] both for point source and line source sand piles. These comparisons exhibit that our numerical simulation results are qualitatively similar, but do not agree quantitatively, because the experiments have been done for three dimensional systems, and different materials were used for the construction of the sand piles.

In the next step, we determine the vertical normal stress for the sand pile constructed from a point source consisting of a mixture of elliptic particles, and it then has to be compared with the result of the stress tensor for a sand pile that contains a mixture of rou-

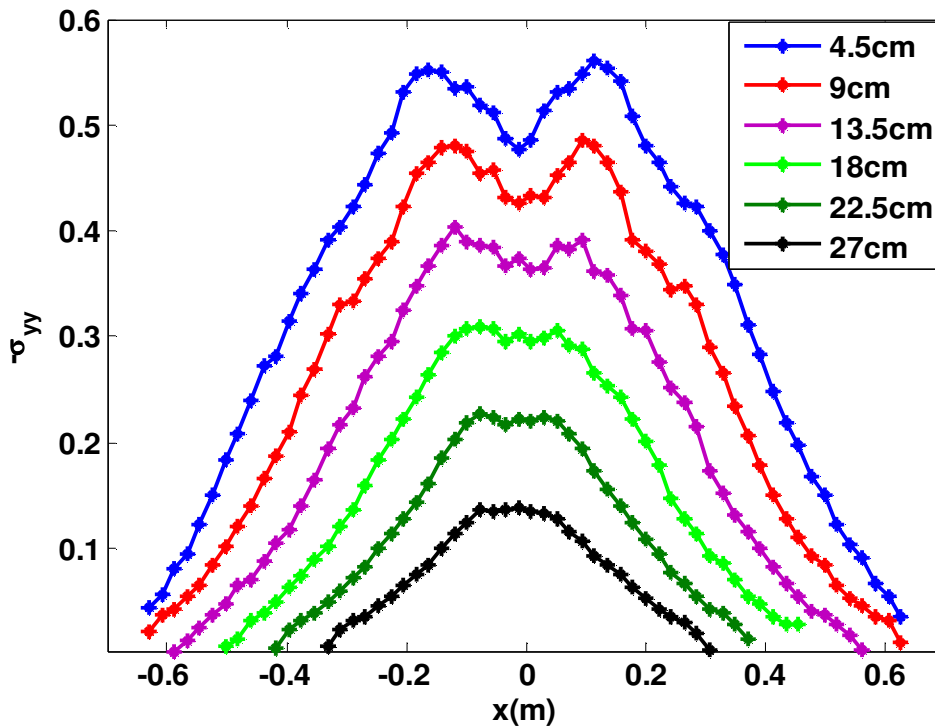


Figure 3.9: Normalized vertical (negative) normal stress tensor at different heights inside the sand pile constructed from a point source. Average over 14 sand piles and height of the pile is 33.5 cm.

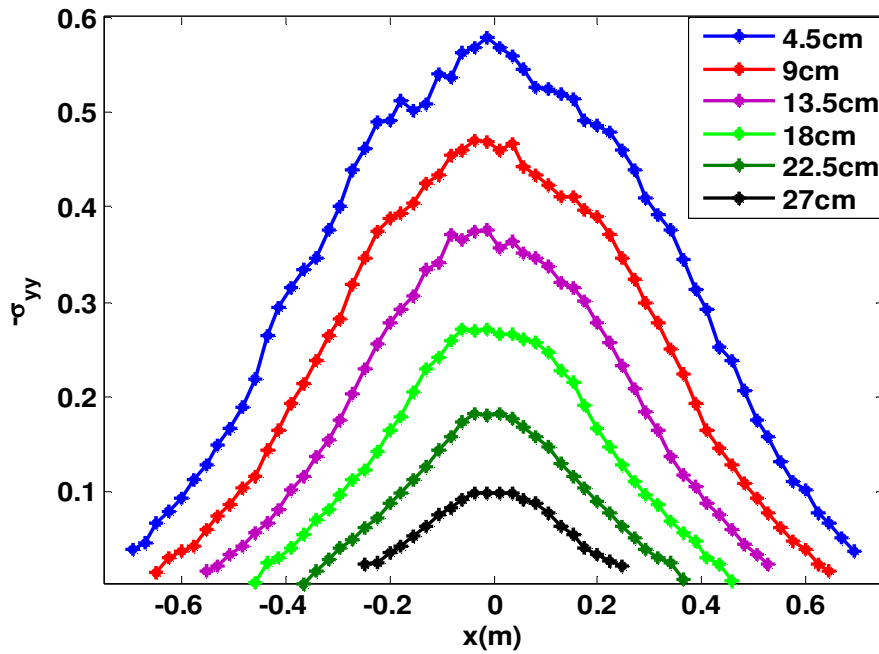


Figure 3.10: Normalized vertical (negative) normal stress tensor at different heights of the sand pile constructed from a line source. Average over 11 sand piles (height of the pile is 31.5cm).

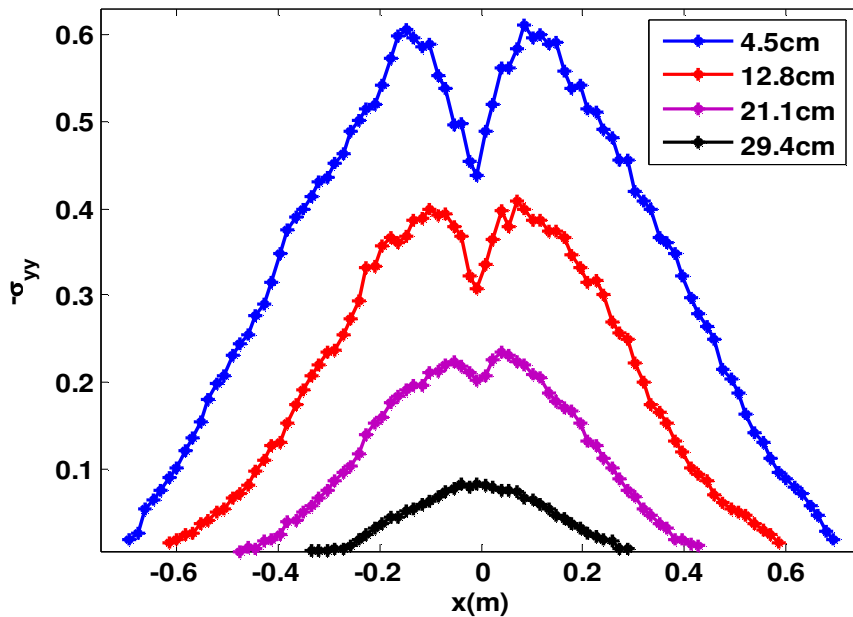


Figure 3.11: Distribution of the vertical normal stress tensor on horizontal cuts at different heights of the point source sand pile constructed from elliptic particles. Average of ten sand piles (height of the pile is 33.5cm).

nd particles. Here, roughly elliptic particles with a ratio of major and minor axis of 2 were used for the simulation. The number of particles and the degree of poly-dispersity we used for the piles of elliptic particles were the same as for the piles of round particles. In order to suppress the fluctuations of the result of stress tensor for single sand pile, we have taken average over 10 sand piles. The average angle of repose obtained for 10 piles was 31° for the mixture of elliptic particles.

Simulation results of the average negative vertical normal stress tensor for piles consisting of a mixture of elliptic particles are illustrated in Fig. 3.11, which shows that the stress dip is clearly much larger below the apex of the pile than for the mixture of round particles. On the other hand, a small dip can be seen below the apex of the pile that contains a mixture of round particles as represented in Fig. 3.9. Moreover, if we compare quantitatively the magnitude of the stress dip between the two sand piles at the bottom layer, the amplitude of the stress dip is around two times larger for elliptic particles. The reason for the existence of the large dip in the centre for a sand pile consisting of elliptic particles may be that the anisotropy of the contact network is larger in the central region for the mixture of elliptic particles than for the mixture of round particles. Next, we compare our simulation results with the existing experimental results done by I. Zuriguel et al. [11] using two shapes of the particles disks and elliptic cylinders. The numerical results are in good qualitative agreement with the experimental results.

3.4 Volume fractions

Here we determine the averaged density (volume fraction) throughout the sand pile and make quantitative comparisons between differently constructed sand piles. The volume fraction is defined as the ratio of the volume of particles and the total volume of the averaging element that contains the particles whose centres of mass lie inside it.

$$v = \frac{1}{V} \sum_{p \in V} V^p,$$

where V^p the volume of the particle p and V is the volume of the averaging element that contains the particles. For the sake of simplicity, we used the simplest averaging technique, the so-called the particle centre averaging, i.e. a particle is taken into account if the corresponding particle centre lies within the averaging volume element.

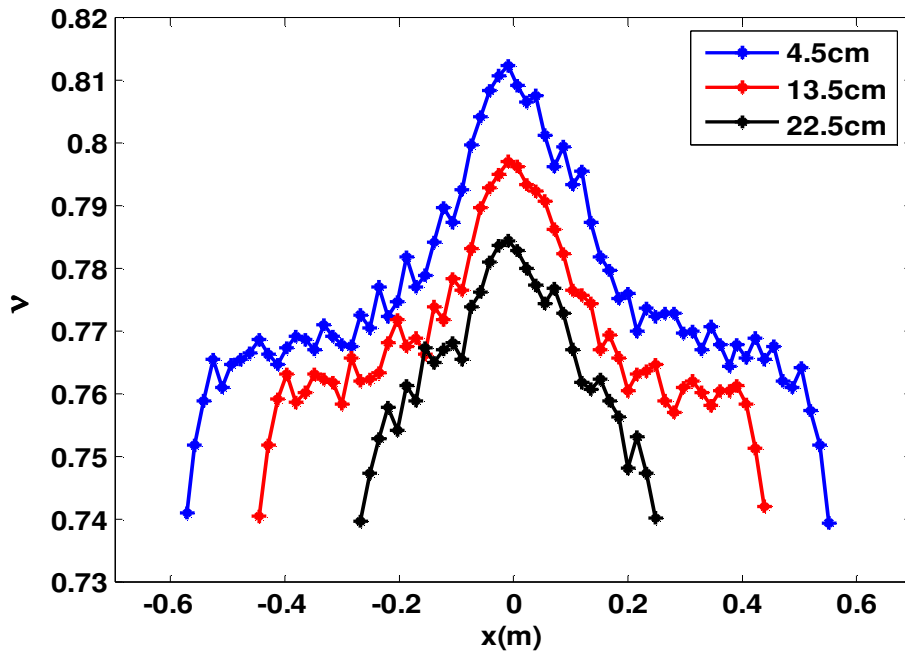


Figure 3.12: Simulation results of the volume fraction for a sand pile constructed from a point source. Average of nine sand piles (height of the pile is 33.5 cm).

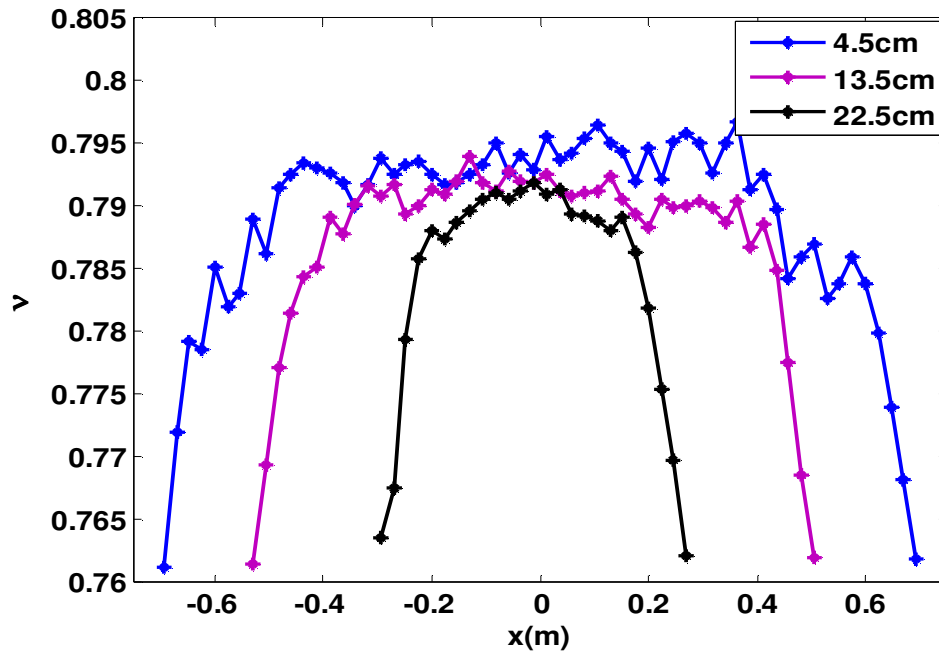


Figure 3.13: Simulation results of the volume fraction for a sand pile constructed from a line source. Average of nine sand piles (height of the pile is 31.5 cm).

The simulation results of averaged density at different heights inside a sand pile constructed from a point source are displaced in Fig. 3.12, whereas the same is represented in Fig. 3.13 for a line source sand pile. For the case of a point source, the density changes with relative heights inside a sand pile and the middle region of the sand pile shows a higher density than the rest of the sand pile. The middle region has a density that is approximately 8-10% higher than the density in the vicinity of the free surface of the sand pile. In contrast, the density is almost constant, close to 0.79 in the line source case, especially in the central region of the sand pile. There is a slightly inhomogeneous distribution in the vicinity of the surface of the sand pile.

We conclude from our numerical investigation of the average density for the sand pile that the construction history of the granular aggregates affects their density distribution, which agrees with the existing experimental conclusion [7] as discussed in details in chapter one.

It is a somewhat surprising result that for a sand pile constructed from a point source the density is maximum at the centre where the pressure is actually *minimum*. An increase of density with decreasing pressure is a signature of instability. A qualitative explanation of the pressure minimum would be a local collapse of the grain arrangement in the interior, leading to increased density and an ‘arch’ of particles above the collapsed part supporting the weight of the column of grains below the pile tip.

3.5 Orientation of the particles in sand piles

In order to obtain the orientation of the particles inside the sand pile, we determine the orientation of the principal axis of the averaged inertia tensor using equation 2.92. Some simulation results are illustrated in Fig. 3.14 for a sand pile constructed from a point source with a mixture of round particles whereas the same is represented in Fig. 3.15 for a sand pile that contains a mixture of elliptic particles. We have taken an average over six sand piles for the case of inertia tensor in order to suppress the fluctuations of single realization.

We note that, the orientations of main axis of the inertia tensor are not qualitatively similar for the two cases. For a sand pile consisting of elliptic particles, the orientation of the major principal axis is perfectly horizontal, which means that the elliptic particles are mainly orientated horizontally (preferred alignment is with long axis horizontal).

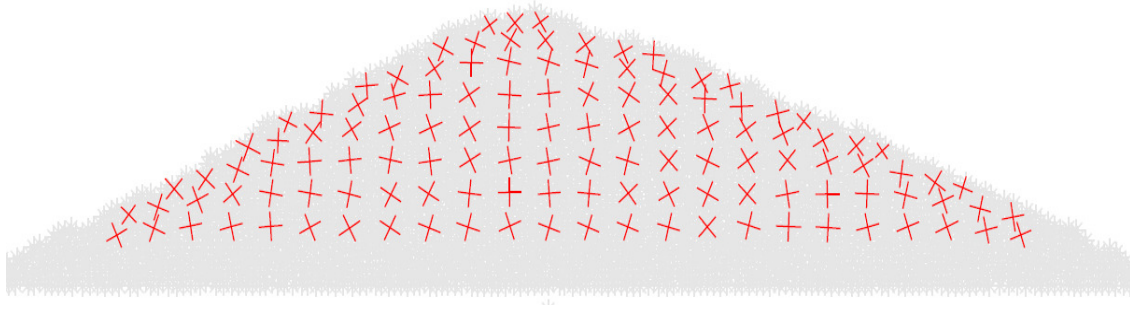


Figure 3.14: Main axis of the inertia tensor inside a sand pile that contains a mixture of roundish particles.

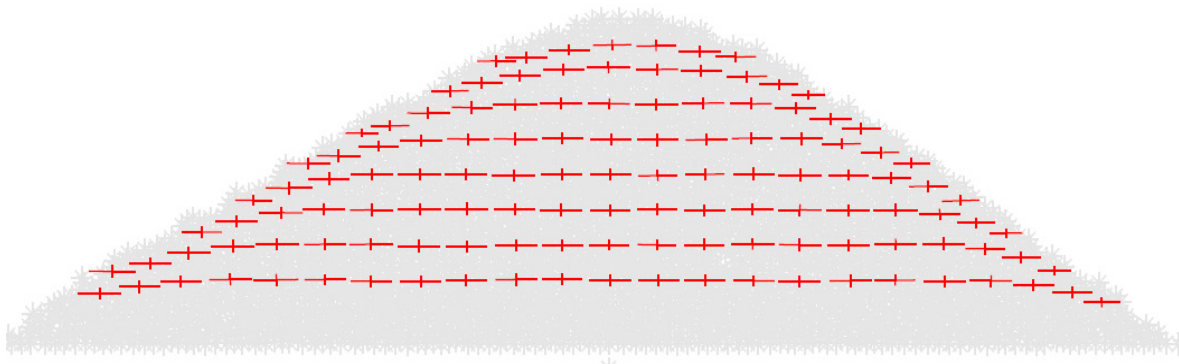


Figure 3.15: Main axis of the inertia tensor inside a sand pile that contains a mixture of elliptic particles.

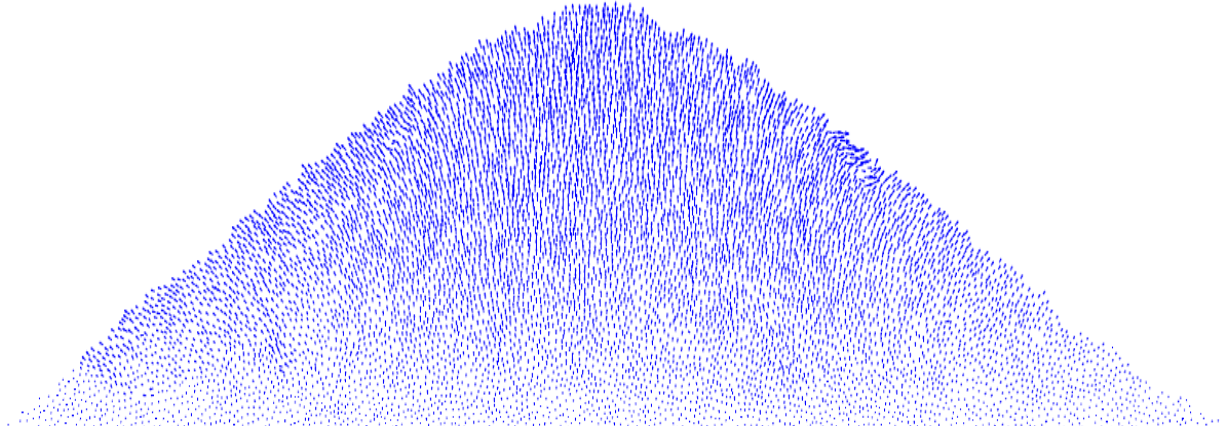


Figure 3.16: Movement of the individual particles of the sand pile constructed from a point source under gravity reduction. Sand pile was relaxed by reducing gravity slowly by about 50%.

3.6 Strain distribution under sand piles

In this section, we focus on the sensitivity of the strain distribution (total strain) to the preparation of sand piles. Before interpreting the results for the strain tensor, first, we present simulation results for the movement of each individual grain inside the sand pile under gravity reduction. The result obtained from the simulation is represented in Fig. 3.16. Each arrow shown in the figure corresponds to the movement of an individual particle. The arrow is drawn from the initial position of the centre of mass (x_i, y_i) of the particle i at the ambient gravity level of a sand pile at $g = 9.81m/s^2$ towards the final point of the centre of mass (x'_i, y'_i) at the new state of the sand pile obtained by reducing gravity slowly by about 50%.

As expected, the range of movement of a particle decreases towards the bottom layers of the sand pile, and increases towards the surface and the tip of the sand pile.

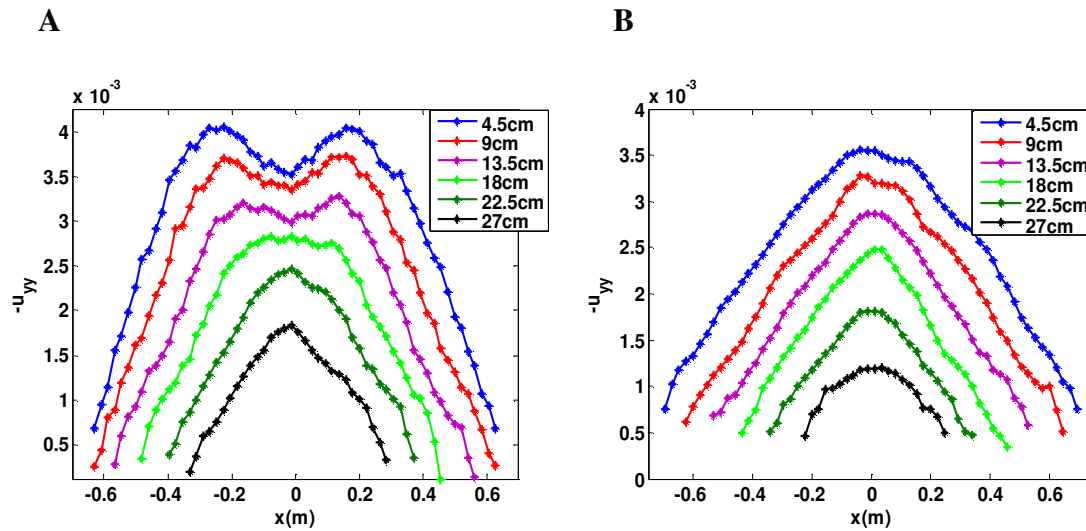


Figure.3.17: Vertical normal strain distribution at different heights of simulated sand pile. **Left:** sand piles constructed from a point source (Average of 11 sand piles and height of the pile is 33.5 cm), **Right:** sand piles poured from a line source (Average of 11 sand piles and height of the pile is 31.5 cm).

The vertical normal strain tensor component obtained from DEM simulations is displayed in Fig. 3.17 for two types of sand piles that were constructed using the two different pouring protocols. The averaged strain tensor was evaluated throughout the sand pile; we represent it via a plot of tensor components as a function of the lateral coordinate x of the pile for layers of given heights y_1, y_2, \dots, y_n .

We give this component of the strain tensor to obtain a qualitative picture, although the foregoing discussion in Section 2.6.2 shows that it is not a rigorously determined quantity. While it has the correct scaling with gravity level, vertical and horizontal strains are of course coupled, so the errors produced by the method in the horizontal direction will also affect the vertical direction. The topmost curve in the graph shows the strain tensor result at the bottom layer of the corresponding sand pile, whereas the bottom curve corresponds to the top layer. Heights are given as function of the total height of the pile to its apex. An interesting feature of the vertical normal strain tensor for various heights is that the vertical normal strain changes with the layer position in the sand piles like the stress tensor. The vertical normal strain shows a dip (Fig. 3.17.A) near the centre of the piles that are poured from a point source. It can be seen that the strain dip appears not only at the bottom layer but also exists up to the certain height inside the sand pile. On the other hand, the vertical normal strain increases towards the centre and towards the bottom layer of sand piles poured from a line source, i.e., a strain dip does not occur in sand piles constructed from a line source, see in figure 3.17.B.

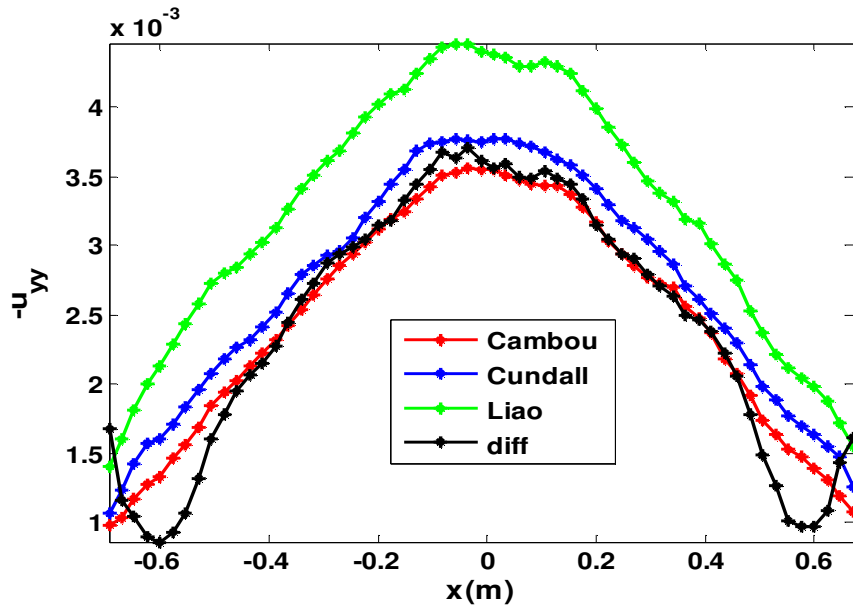


Figure 3.18: Vertical normal strain tensor at the bottom layer of the sand pile constructed from a line source obtained using four different approaches.

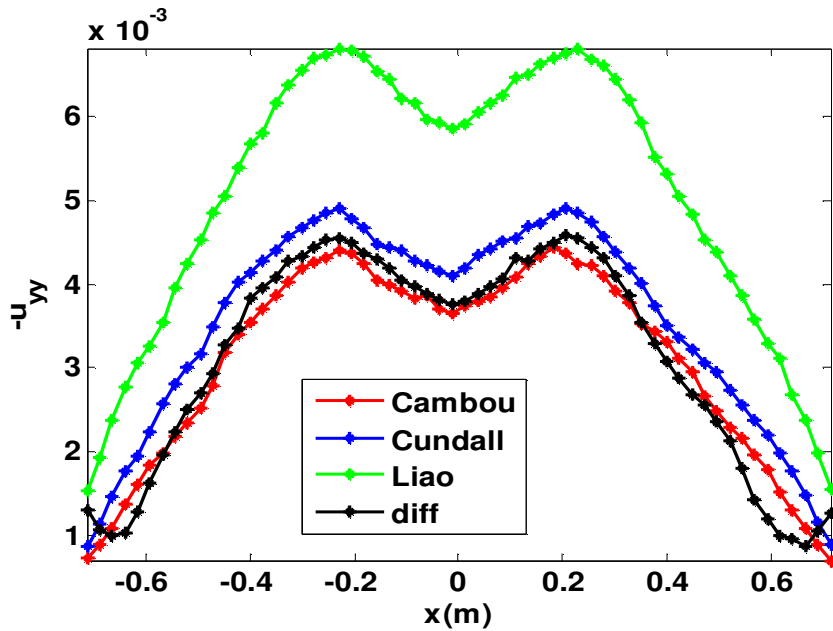


Figure 3.19: Vertical normal strain tensor at the bottom layer of the sand pile constructed from a point source obtained using four different approaches.

3.6.1 Comparison of strain tensor

Here, we are interested in determining the strains (total strain) using four different versions of strain tensors (three best-fit strains and derivative strain) using the equations (2.57), (2.66), (2.73), and (2.76) by numerical investigation, and to compare the results for the vertical normal strain tensor both qualitatively and quantitatively with each other. The numerical simulation results were obtained using our code. The results of the average (negative) vertical normal strain at the bottom layer of the sand pile constructed from a line source are illustrated in Fig. 3.18. All the strain tensors were measured via imposing 10% of reduction of gravity from the actual state of the gravity level.

For the case of a line source, we have averaged results over seven sand piles in order to reduce fluctuations. We observe from Fig. 3.18 that the best-fit strains of Cambou et al. and Cundall et al. are close to each other with a deviation of few percent, while the best fit strain of Liao et al significantly differs from the Cambou strain and Cundall strain, the deviation went up to 30-40%. The reason for this large deviation may be the inclusion of particle rotations in the calculation of the Liao strain, instead of consideration of only the translation of the particle centre. Presumably, the Liao strain might be useful in theories employing micro-polar continua and involving couple stresses in addition to force stresses. Then micro rotation effects may partially compensate for the excess strains of Liao et al. As long as we assume a symmetric stress tensor, the other strain definitions are more useful.

On the other hand, the vertical normal (negative) strain obtained using the differentiation method shows a different behaviour than the other strains especially in the vicinity of the surface of the sand pile, but, shows a similar behaviour towards the centre of the sand pile. It is in good agreement quantitatively with the best-fit strains of Cambou et al. and Cundall et al. Clearly, numerical differentiation should be avoided whenever possible and the deviations near the extremities of the sand pile are artifacts of the procedure.

Furthermore, we compared the results of the four types of strains quantitatively for sand piles constructed from a point source. Fig. 3.19 gives the simulation results of average negative vertical normal strains at the bottom layer of the point source sand pile. For the point source case, we averaged the strains over seven sand piles each. All four methods produce a strain dip under piles constructed from a point source, as expected. Again, quantitative comparison indicates strong deviations for the Liao strain, which should not be used in our context, and exhibits the deficiencies of the differentiation method.

3.7 Properties of the fabric tensor

In this section, we determine various properties of the fabric tensor inside a sand pile created from a point source. The fabric tensor is symmetric by definition and therefore normally consists of three independent components in two dimensions. These may be expressed in a largely coordinate independent way using tensor invariants and geometrical quantities.

As the first of these quantities, we choose the trace of the fabric tensor defining the average contact density of the sand pile. It is also known as the volumetric part of the fabric and given by $tr(F) = F_{\max} + F_{\min}$, where F_{\max} and F_{\min} are the major and minor eigenvalues of the fabric tensor, respectively. In Fig. 3.20.A, the trace of the averaged fabric tensor is plotted at different heights inside the sand pile. It can be seen from the figure that the mean number of contacts decreases near the surface of the sand pile and increases with increasing distance from the surface to the centre of the sand pile. Since we have measured the density to increase towards the centre of the pile in the case of a pile poured from a point source, this means that the number of contacts is higher where the density is maximum.

As a second independent quantity determining the fabric tensor we may choose the fabric deviator. It is defined as $F_D = F_{\max} - F_{\min}$ and is a measure of the degree of anisotropy in the contact network of the granular assembly. The deviatoric fraction of the fabric tensor $F_D / tr(F)$ is plotted in Fig. 3.20.B for different heights inside the sand pile. From the figure, it is observed that the deviatoric fraction behaves differently from the trace of the fabric tensor, as it decreases towards the centre and increases towards the free surface of the pile. This means that the fabric is more isotropic near the centre of the sand pile and more anisotropic in the outer part. The fabric anisotropy is between 0.05 and 0.15.

The angle of the orientation of the major eigenvector of fabric tensor may serve as the third independent quantity defining the fabric tensor. The orientation of the major eigenvector with respect to the horizontal axis is given in Fig. 3.20.C at different heights inside the sand pile. It changes from -40° (left) to $+40^\circ$ (right).

The orientation of three macroscopic tensors stress, strain and fabric are plotted in Fig. 3.20.D only for the first two bottom layers of the pile. No meaning should be attributed to the deviation of the strain tensor from the behaviour of the stress tensor, since the xx and xy components of the former cannot be determined reliably. It can be seen, however, that the orientations are different also for the fabric and stress tensors, which means that these macroscopic tensors are not collinear. Most likely this limits the utility of a description of granular piles in terms of isotropic elasticity. Nevertheless, we shall consider such a description in the following to explore these limitations in some detail.

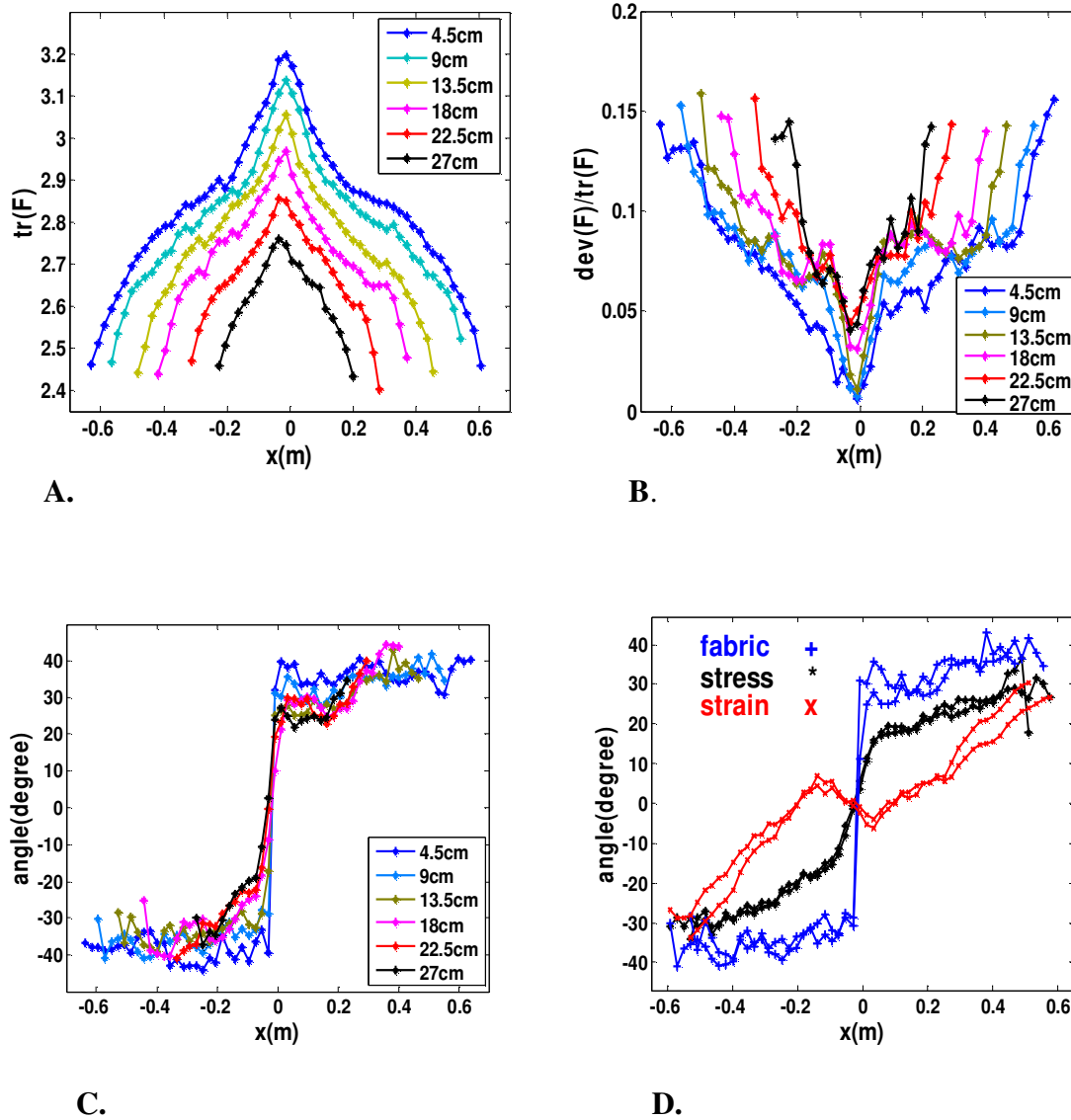


Figure 3.20.A-D: Simulation results of the different properties of the averaged fabric tensor for the sand pile created by the point source. (A) Trace of the fabric tensor, (B) deviatoric fraction, (C) orientation of fabric versus lateral position in the sand pile, and (D) orientation of fabric, stress and strain plotted only for the first two bottom layers of the sand pile. Average over eleven sand piles (height of the pile is 31.5 cm).

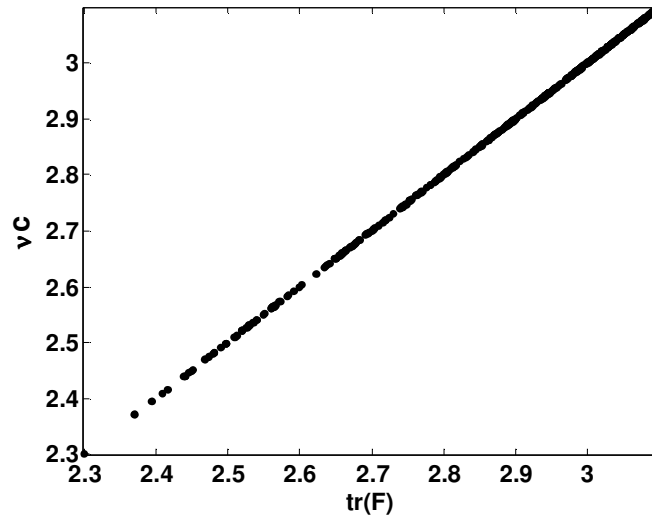
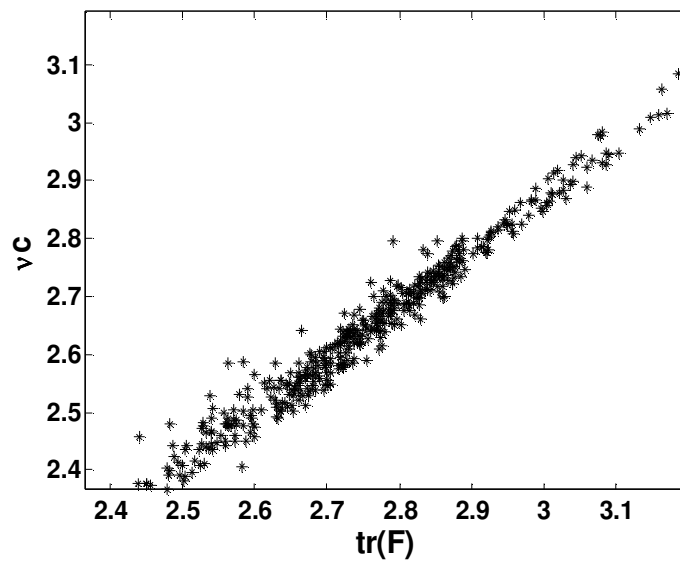
A**B**

Figure 3.21: Product of the volume fraction and mean coordination number plotted as a function of the trace of the averaged fabric tensor. **A:** for piles consisting of mono-disperse mixture of particles, **B:** for piles consisting of poly-disperse mixture of particles.

In the next step, we determine the correlation between trace of the fabric tensor and product of the volume fraction ν and the mean coordination number c .

We plot the product of the volume fraction and mean coordination number of a sand pile constructed from a point source as a function of the trace of the fabric tensor in Fig. 3.21. The top panel of the figure shows the result for a mono-disperse arrangement of particles, whereas the bottom panel shows the same for a poly-disperse mixture of the particles. In the first case, all the data points collapse on a single straight line, which means that the averaged fabric tensor is linearly proportional to the product of the volume fraction and mean coordination number. Moreover, the proportionality constant is one, i.e.,

$$\text{tr}(\langle F \rangle) \cong \nu c. \quad (3.1)$$

This is to be expected from the definition of the fabric tensor. Remember that for a single particle $\text{tr}(F) = c^P$ (equation 2.103).

On the other hand, for a poly-disperse systems the trace of the averaged fabric tensor is not linearly proportional to the product of the volume fraction and mean coordination number: i.e.

$$\text{tr}(\langle F \rangle) \neq \nu c. \quad (3.2)$$

This is not unexpected either, because for poly-disperse particles the local volume fraction differ and we have $\nu c \neq \langle \nu c^P \rangle$, meaning that volume fraction and contact number are not statistically independent.

For poly-disperse granular materials, Luding et al. [127] introduced a dimensionless (scalar) factor, the so-called ‘correction factor’ which is only dependent on the particle size probability distribution function in order to predict a macroscopic material property based on a microscopic property of the granular materials. According to Luding et al, the trace of the fabric tensor can be factorised into three contributions: (1) the volume fraction of the granular assemblies (2) the mean coordination number (3) a correction factor g_2 . We can write the trace of the averaged fabric tensor for a poly-disperse granular system as in a mathematical expression:

$$\text{tr}(\langle F \rangle) \cong \nu c g_2. \quad (3.3)$$

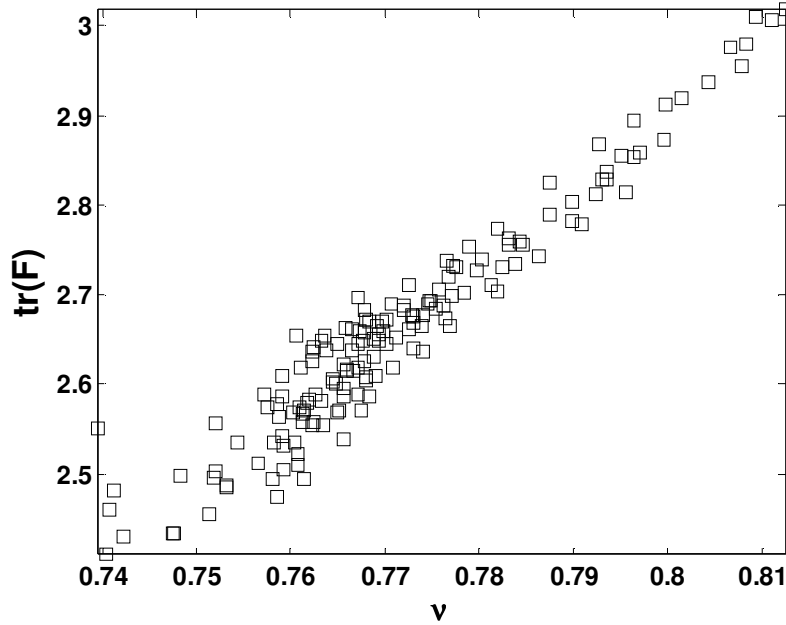


Figure 3.22: Trace of the fabric tensor plotted as a function of the volume fraction for a sand pile constructed from a point source.

The detailed analytical derivation of the correction factor is described in ref. [127]. We have determined the correction factor g_2 simply from our DEM numerical simulation results by taking the ratio between $tr(\langle F \rangle)$ and vc , i.e.

$$g_2 = \frac{tr(\langle F \rangle)}{vc}. \quad (3.4)$$

From the above equation (3.4), we find the correction factor is $g_2 = 1.045$ for a sand pile consisting of poly-dispersity mixture of the particles with a degree of poly-dispersity of 30%. We have not verified the theoretical prediction for g_2 with our numerical measurement.

We plot in Fig. 3.22, the trace of the fabric tensor against the volume fraction of a sand pile constructed from a point source. The behaviour is roughly linear, meaning that the contact number density is proportional to the volume fraction of the sand pile. In conclusion, we have a lower pressure in the central region of the sand pile constructed from a point source than in the region around, the density is locally maximum and the contact-number-density shows same behaviour.

3.8 Distribution of stress and strain invariants

In this section, we are interested in determining the relationship between the invariants of the incremental stress tensor and the incremental strain tensor for a pile that would allow us to obtain elasto-plastic behaviour of a sand pile. The incremental stress was obtained by simply evaluating the stress tensor at two different gravity levels and taking the difference. The incremental strain was obtained by determining the position changes at the particle centres when gravity was changed from one level to the other and by using these as displacement vectors for the calculation of a best-fit strain (see Section 2.6.2).

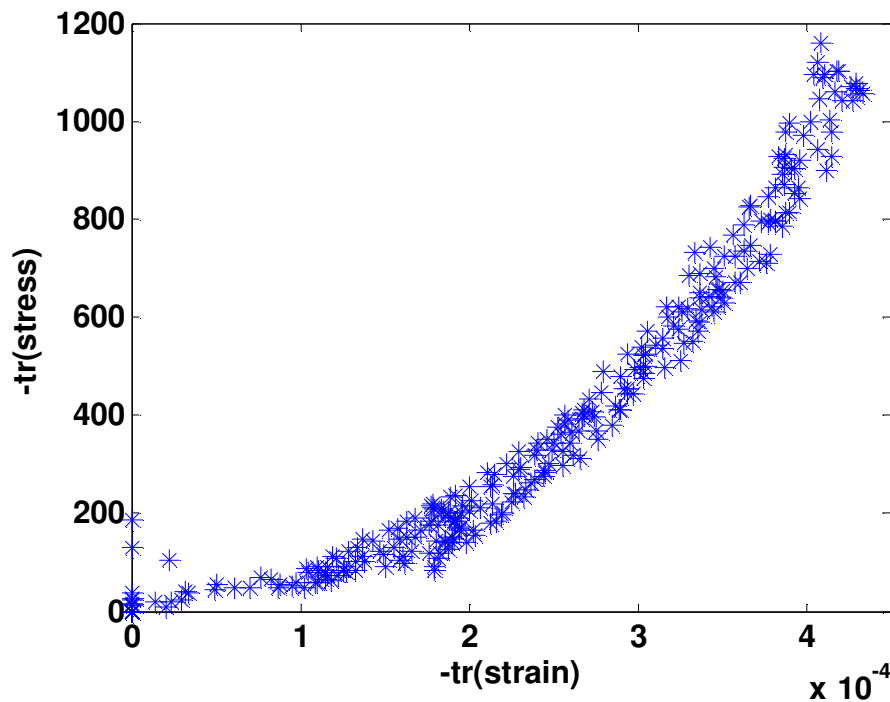


Figure.3.23: Correlation between trace of the incremental stress tensor and trace of the incremental strain tensor.

Cantelaube, and Goddard [2], in fact, one of the probably too simple assumptions of the elasto-plastic model [2] is that the compatibility relation of linear elasticity holds right up to the yield loci. Because we have measured stresses and strains everywhere in the sand pile, we can check this more or less directly.

We plot in Fig. 3.23 the trace of the (negative) incremental stress tensor as a function of the trace of the (negative) incremental strain tensor. The graph shows that the behaviour is nonlinear. The flat part of the graph corresponds to the points that are close to the surface of the sand pile. The slope of this graph is the differential bulk modulus; we

observe that it decreases smoothly near the surface which means that there is a smooth transition from elastic to plastic behaviour (if any) rather than a discontinuous one. What is interesting about this graph is that we have very (roughly) linear elastic behaviour for large strains and stresses and nonlinear behaviour announcing the transition to plastic behaviour for smaller strains, contrary to what one sees in solid state mechanics, where the plastic behaviour is a consequence of large loads. Of course, this is due to the non-cohesive nature of the granular medium. Under compressive external load the pile behaves mostly elastic, but when this load becomes small or negligible, the lack of attractive interaction between the particles makes itself felt, the sand starts act like an isotatic network, which is almost flexible, and hence plastic.

Similar behaviour was observed in the analytical approach [2] for sand piles obtained by Didwania, Cantelaube, and Goddard as they assumed linear elastic behaviour near the centre and plastic behaviour closer to the surface of the sand pile.

3.9 Coordination number for different changes in gravitation

The average coordination numbers of the sand pile are determined for different values of loading by either increasing or decreasing gravity from the ambient gravity level. The average coordination number c , in our definition, corresponds to the mean number of contacts per particle within a volume element V .

$$c = \frac{1}{N} \sum_{p \in V} n^p, \quad (3.5)$$

where n^p denote the number of contacts of the particle p and N is number of particles that lie within the averaging volume element V whose centres of mass lie inside it.

Fig. 3.24 displays the simulation results for the probability distribution of the average coordination number for a sand pile with different changes of gravitational acceleration. From the figure we find that the mean coordination number changes with a change in gravity, albeit slightly. For 90% reduction of gravity, the coordination number is about 8% smaller than the coordination number at ambient gravity, whereas it is higher by about 4%, if we increase the gravity by the same amount of 90% from the ambient gravity level. Not surprisingly, the average contact number of the particles decreases for reduction of gravity and increases for enhancement of gravity.

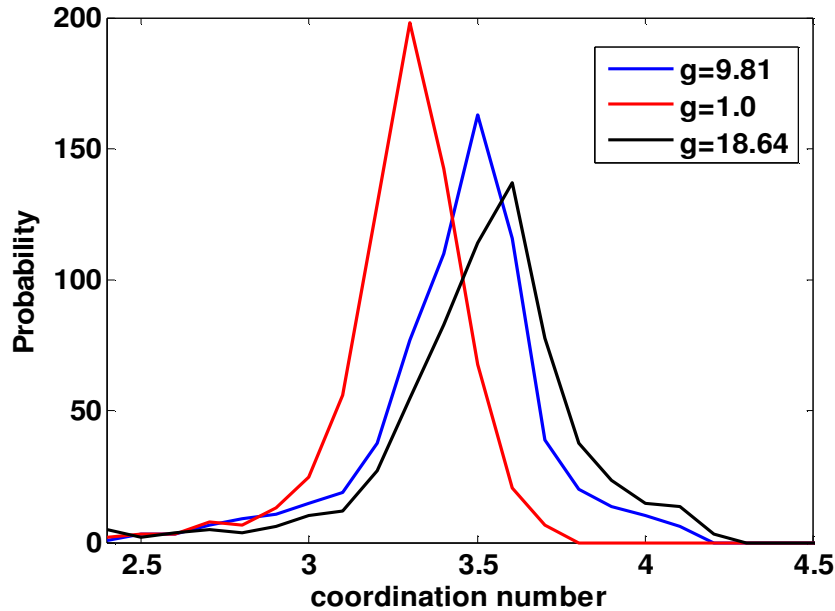


Figure 3.24: Probability distribution of the average coordination number for a sand pile poured from a point source with different changes in gravity. The blue curve represents the probability distribution of the average coordination number for a sand pile at the gravity level of $g = 9.81$, whereas red and black curves corresponds to $g = 1$, and to $g = 18.62$, respectively.

3.10 Determination of elastic constants

In this section, we present simulation results of the effective material properties of sand piles constructed from a point source. By performing discrete element method simulations we obtain macroscopic strain tensors from microscopic displacements of the individual grains in a two-dimensional sand pile. Computing stresses in addition, we can estimate local elastic constants assuming Hooke's law. Generally speaking, if we find almost constant values of elastic constants throughout the sand piles, linear elasticity may be considered a good approximation. If we get, on the other hand, strongly varying elastic constants, then we can say that linear elasticity is not going to work for the pile as a whole. Moreover, this computation serves as a consistency check for theoretical assumptions such as the rigid-particle hypothesis. If our calculation produced elastic constants of the same order of magnitude as the Young's modulus that we assign to the particles to allow an overlap for force calculation, then the idea that the sand pile has a macroscopic elastic behavior different from that of its microscopic constituents would not be valid be-

cause the elastic constants of the pile would go to infinity with those of the grains. This idea can work only, if the sand pile admits a finite elastic response in spite of the rigidity of the grains, which means that the measured elastic coefficients of the sand pile should be significantly smaller in the simulation than those assigned to the particles.

Under the assumption that the material is locally isotropic, we can characterize its elastic constants using only two coefficients, for example Young's modulus and Poisson's ratio. The relation between stress tensor and strain tensor reads

$$\sigma_{ik} = \frac{E}{1+\nu} \left(u_{ik} + \frac{\nu}{1-2\nu} u_{ll} \delta_{ik} \right). \quad (3.6)$$

Written out in components for the two dimensional case this becomes

$$\sigma_{xx} = \frac{E}{(1+\nu)(1-2\nu)} ((1-\nu)u_{xx} + \nu u_{yy}), \quad (3.7)$$

$$\sigma_{yy} = \frac{E}{(1+\nu)(1-2\nu)} ((1-\nu)u_{yy} + \nu u_{xx}), \quad (3.8)$$

$$\sigma_{xy} = \frac{E}{1+\nu} u_{xy}. \quad (3.9)$$

In our case, the unknown quantities are E and ν .

Equations (3.7) and (3.8) allow us to obtain simple expressions for the trace and the first normal stress difference

$$\sigma_{xx} + \sigma_{yy} = \frac{E}{(1+\nu)(1-2\nu)} (u_{xx} + u_{yy}), \quad (3.10)$$

$$\sigma_{xx} - \sigma_{yy} = \frac{E}{1+\nu} (u_{xx} - u_{yy}). \quad (3.11)$$

The next step is to determine the best approximation for E and ν satisfying all three equations (3.9) (3.10) & (3.11) as closely as possible. This is a minimization problem for given fields σ_{ij} and u_{ij} , which may be cast as follows. Set

$$f(\nu, E) = [(1+\nu)(1-2\nu)(\sigma_{xx} + \sigma_{yy}) - E(u_{xx} + u_{yy})]^2 + [(1+\nu)(\sigma_{xx} - \sigma_{yy}) - E(u_{xx} - u_{yy})]^2 + [(1+\nu)\sigma_{xy} - Eu_{xy}]^2, \quad (3.12)$$

and minimize this expression with respect to E and ν . That is, we set

$$\frac{\partial f}{\partial E} = 0, \quad \frac{\partial f}{\partial \nu} = 0,$$

and these two equations should be solved for E and ν in principle. It is found that they constitute a nonlinear system that cannot be solved analytically (though a numerical solution should not be too difficult). A simpler approach is to use two different elastic constants, also well-known, namely the bulk modulus K and the shear modulus G , which are related to Young's modulus and the Poisson number via the following equations:

$$K = \frac{E}{2(1+\nu)(1-2\nu)}, \quad (3.13)$$

$$G = \frac{E}{2(1+\nu)}, \quad (3.14)$$

which allows to rewrite the above three equation in terms of G and K , to obtain

$$\begin{aligned} \sigma_{xx} + \sigma_{yy} &= 2K(u_{xx} + u_{yy}), \\ \sigma_{xx} - \sigma_{yy} &= 2G(u_{xx} - u_{yy}), \\ \sigma_{xy} &= 2Gu_{xy}. \end{aligned}$$

Then we minimize the expression

$$g(G, K) = [(\sigma_{xx} + \sigma_{yy}) - 2K(u_{xx} + u_{yy})]^2 + [(\sigma_{xx} - \sigma_{yy}) - 2G(u_{xx} - u_{yy})]^2 + 4[\sigma_{xy} - 2Gu_{xy}]^2 \quad (3.15)$$

with respect to G and K , i.e., we set

$$\frac{\partial g}{\partial G} = 0, \quad \frac{\partial g}{\partial K} = 0.$$

Solving the simplified equations for K and G we obtain

$$K = 0.5 * \frac{(\sigma_{xx} + \sigma_{yy})}{(u_{xx} + u_{yy})}, \quad (3.16)$$

$$G = 0.5 * \frac{(\sigma_{xx} - \sigma_{yy})(u_{xx} - u_{yy}) + 4\sigma_{xy}u_{xy}}{(u_{xx} - u_{yy})^2 + 4u_{xy}u_{xy}}. \quad (3.17)$$

Note that this calculation works the same way with incremental stresses and strains, so we can determine elastic constants even though we cannot obtain the absolute strain tensor. Once K and G have been determined, we can calculate E and ν as follows,

$$\nu = 0.5 \left(1 - \frac{G}{K} \right), \quad (3.18)$$

$$E = 3G - \frac{G^2}{K}. \quad (3.19)$$

The effective material properties as obtained in simulations of sand piles that were constructed from a point source are shown in Fig. 3.25.A-D. We measured the elastic constants at different heights inside the sand pile. The topmost curve in panels A, B, and C corresponds to the results for the bottom layer, whereas the bottom curve was measured the top layer of the sand piles. For Fig. 3.25.D, the layer to which a curve corresponds may be gathered from the domain of definition of the curve: this is largest for the bottom layer and smallest for the top layer (so the curve with the smallest variation corresponds to the bottom layer). We find that the elastic constants vary with position inside the sand pile. In addition, we see that the elastic constants Young's modulus of elasticity, shear modulus, and bulk modulus increase towards the centre and towards the bottom, and decrease towards the surface with very little fluctuation.

We use a Young's modulus of $E = 10^7 N/m$ for each particle and the scale of the measured elastic modulus of the sand pile is approximately $E = 10^6 N/m$, i.e. one order of magnitude smaller for small load as we reduced gravitation by only 10%. That means, the simulated sand pile is softer around one order of magnitude than its individual particles. The bulk modulus is observed to increase towards the centre, indicating the central core region of the heap is much harder than the region closer to the surface. It can be seen in Fig. 3.25.D that Poisson's ratio behaves differently as it increases towards the surface of the sand pile and decreases towards centre and tip of the sand pile, especially, it fluctuates more near the tip of the sand pile.

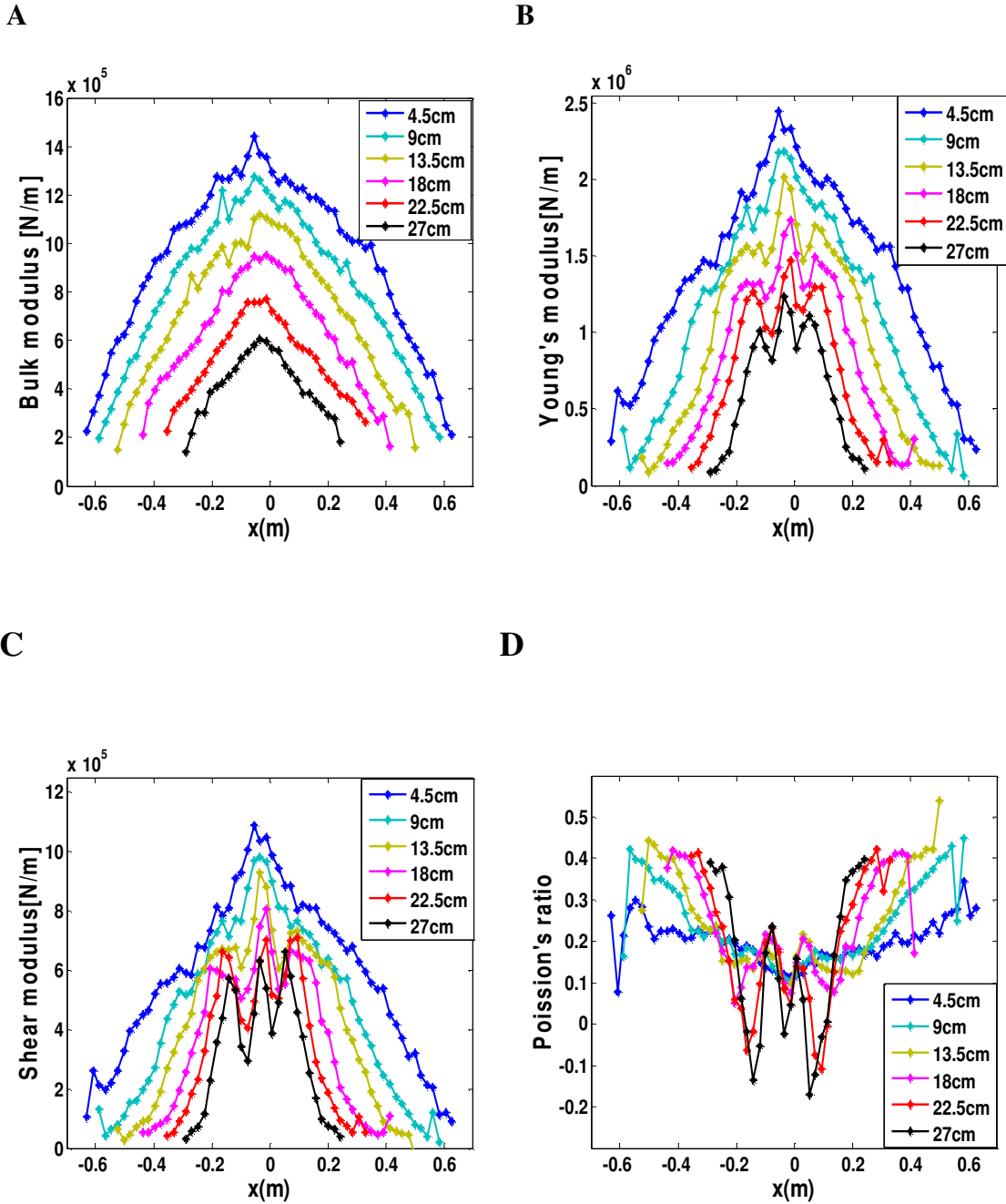


Figure 3.25: Effective material properties from simulation of sand pile poured from a point source. (A) Bulk modulus of elasticity (B) Young's modulus of elasticity, (C) Shear modulus, and (D) Poisson's ratio. Average over eleven sand piles (height of the pile is 33.5 cm).

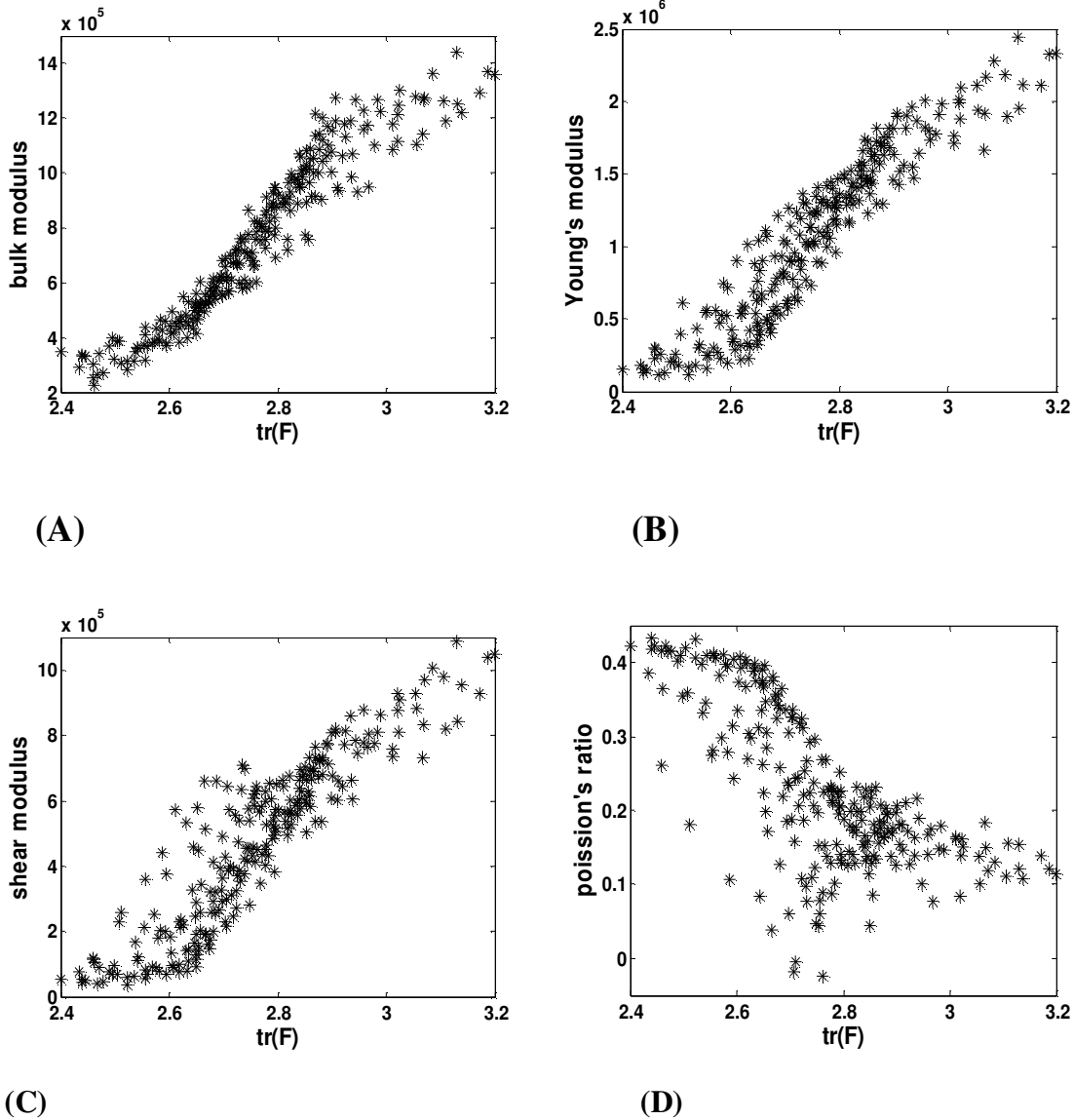


Figure 3.26: Correlation between elastic constants with the trace of the fabric tensor. (A) Bulk modulus of elasticity (B) Young's modulus of elasticity, (C) Shear modulus, and (D) Poisson's ratio, plotted against the trace of the fabric tensor throughout the sand pile.

In Fig. 3.26, we establish a correlation between elastic constants and the trace of the fabric tensor. In Fig. 3.26.A, we plot the bulk modulus of the macroscopic sand piles against the trace of fabric tensor. Obviously, the behaviour is linear to a decent approximation, i.e. the stiffness of the particles is a linear function of the trace of the fabric tensor, i.e. the number of contacts of a particle. Furthermore, Young's modulus and the shear modulus are plotted, respectively, as a function of this coordination number in the Fig. 3.26.B and 3.26.C. The behaviour also is roughly linear for both cases. A similar plot for Poisson's ratio as a function of the fabric is plotted in Fig. 3.26.D. In this case, the behaviour is nonlinear, but a simple linear relationship is not expected.

3.11 Stress distribution for asymmetric sand pile

In Section 3.3, we have represented and discussed numerical results concerning the stress distribution under symmetric sand piles. Up to now, no stresses have been measured for asymmetric sand piles either experimentally or numerically. However, there exists in the literature an elasto-plastic continuum model set up by Didwania, Cantelaube, and Goddard, see in ref. [2] predicting an analytical solution for the stress distribution inside an asymmetric sand pile. In order to determine stresses under an asymmetric sand pile we have performed discrete element method simulation of two-dimensional asymmetric sand piles, and then calculated numerical data to be compared quantitatively with the analytical prediction for the stress tensor.

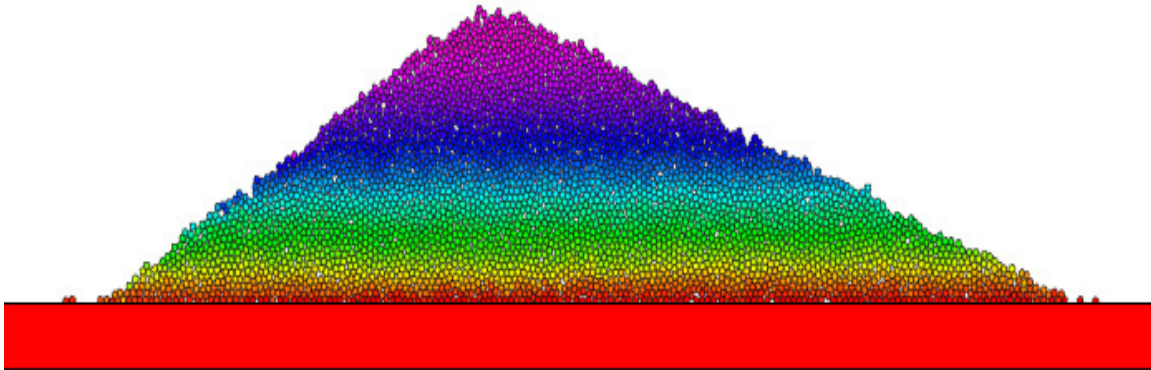


Figure 3.27: Simulated asymmetric sand pile constructed from a line source.

We simulate asymmetric sand piles by constructing them from about of 3800 polygonal particles that are poured from a line source. An example is shown in Fig. 3.27. Particles used were soft round shaped with a fixed number of corners (seven) for individual simulations and the degree of poly-dispersity was 10%. The procedure for constructing an asymmetric sand pile from a line source is based on a similar line of thought as the construction of the symmetric sand pile, but instead of depositing a new layer onto an already present one symmetrically we deposit it in an asymmetric way, shifting the centre of the line source in each deposition step by a constant amount. The average angle of repose obtained for seven sand piles was 31° for the left-hand side of the pile and 22° for the right-hand side of the pile.

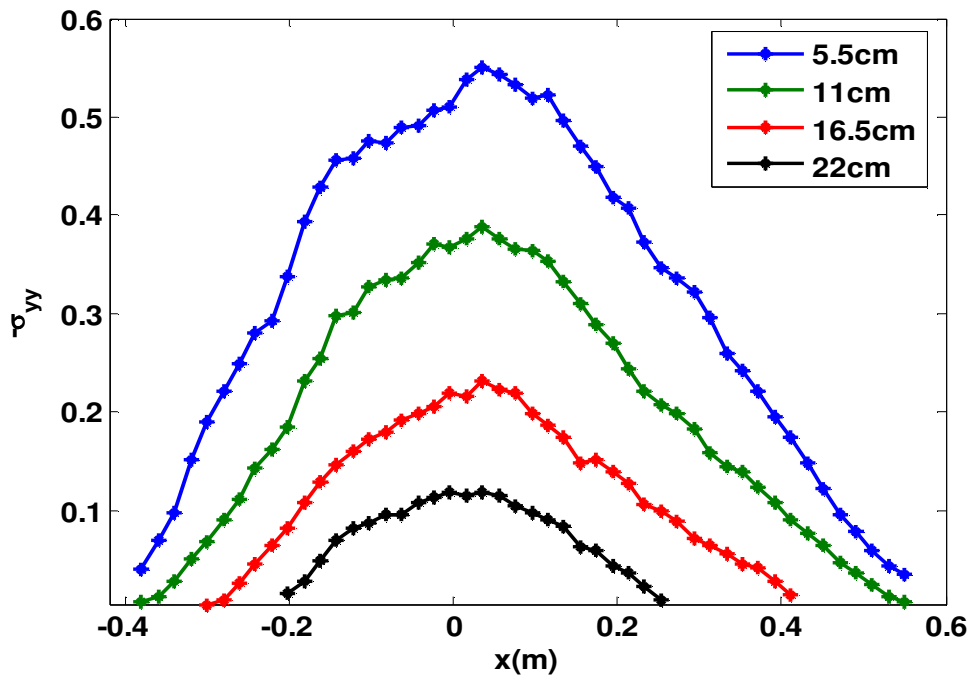


Figure 3.28: Simulation result for the vertical normal stress distribution (normalized) at various heights inside a two-dimensional asymmetric sand heap constructed from a line source. Height of the pile is 24.5 cm.

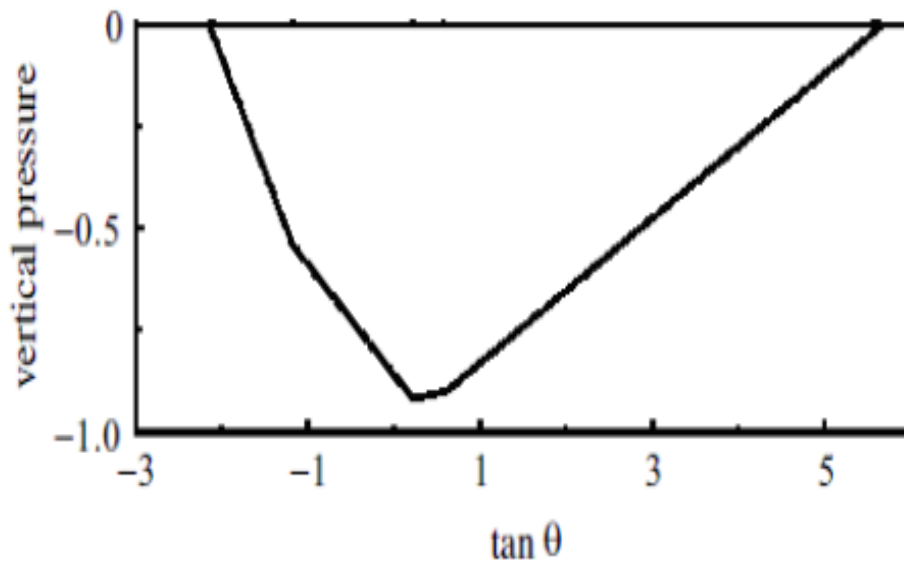


Figure 3.29: Theoretical prediction of the vertical normal stress distribution at the bottom of a two dimensional asymmetric sand heap, exhibiting a plateau behaviour below the apex of the heap.

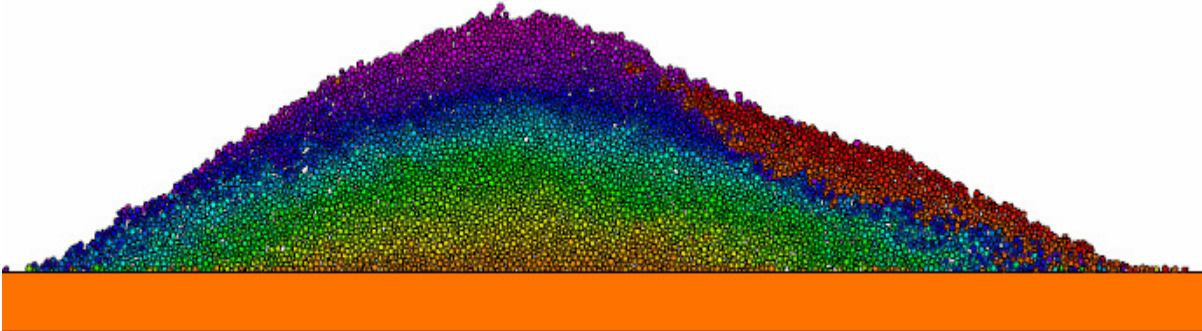


Figure 3.30: Simulated asymmetric sand pile constructed from a point source.

Fig. 3.28 reveals the simulation results for the averaged normalized (negative) vertical normal stress tensor along horizontal cuts at different heights of an asymmetric sand pile constructed from a line source. In the figure, the blue curve represents the results at the bottom layer of the corresponding sand pile, whereas the black curve corresponds to the top layer. From the figure, we find an asymmetric pressure distribution under an asymmetric sand pile, as expected and a plateau distribution below the apex of the pile (peaked shape behaviour). No experimental results exist in the literature to compare our numerical simulation results,

Next, we compare our simulation results with the available analytical prediction of the stress solution for an asymmetric sand pile obtained by Didwania, Cantelaube, and Goddard [2]. It is given in Fig. 3.29. Comparing the numerical simulation result for the stress distribution at the bottom layer of the pile (blue curve) with that of the analytical solution shows that the behavior is qualitatively similar.

Furthermore, we were able to construct an asymmetric sand pile from the point source. One of the simulated sand piles is shown in Fig. 3.30. It consists of 3864 polygonal particles with each particle having seven corners. We used a poly-disperse mixture of round particles with a degree of poly-dispersity of about 25%. The procedure for constructing an asymmetric sand pile from a point source is essentially the same as that of the construction of a symmetric sand pile, but instead of using a fixed height point source (the funnel), we move the funnel slowly horizontally towards the right hand side. In order to suppress the fluctuations of the result of stress tensor for single sand pile, we have taken average over six sand piles. The average angle of repose for the left-hand side

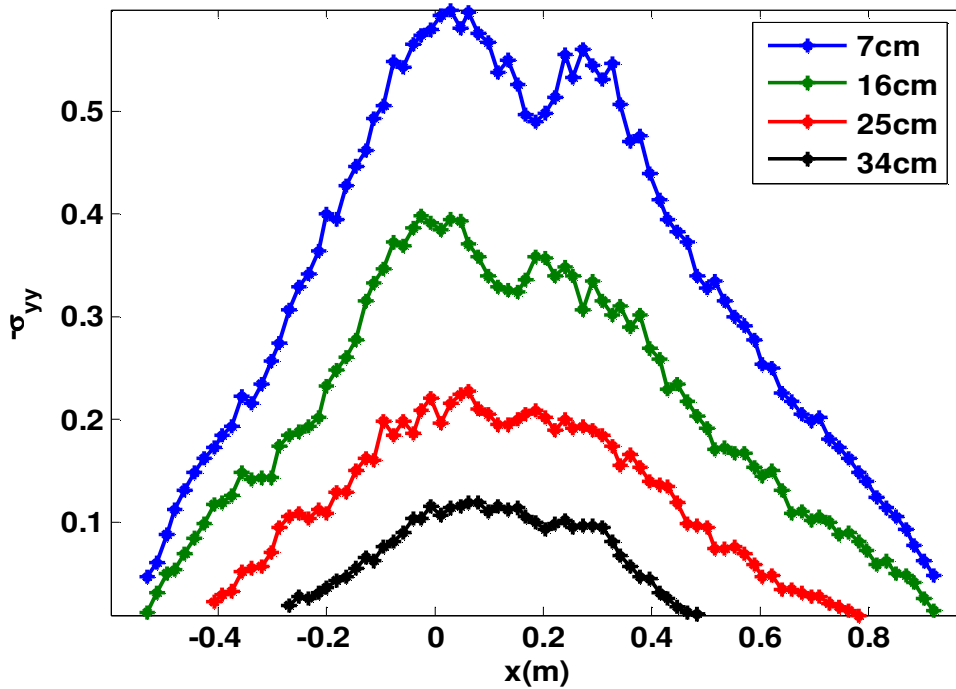


Figure 3.31: Numerical results for the vertical normal stress distribution (normalized) at various heights inside a two-dimensional asymmetric sand heap constructed from a point source. Height of the pile is 38 cm.

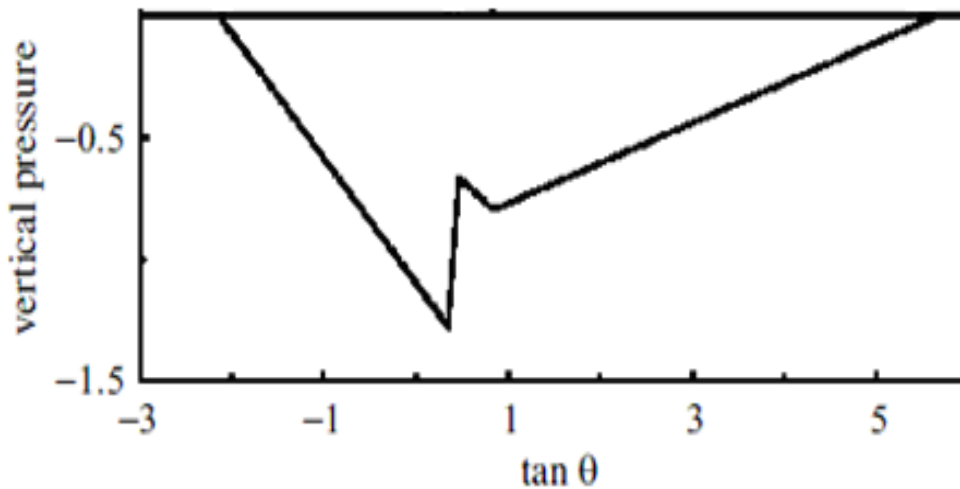


Figure 3.32: Theoretical prediction of vertical normal stress distribution at the bottom of a two-dimensional asymmetric sand heap. There is a dip below or slightly to the right of the apex of the heap.

of the sand pile obtained for seven sand piles was 28° and it was 21° for the right-hand side of the sand pile.

We present in Fig. 3.31 the numerical simulation results of the averaged normalized (negative) vertical normal stress tensor on horizontal cuts at different heights of an asymmetric sand pile constructed from a point source. We observe that there is an asymmetric pressure distribution below the apex of the pile, and a dip exists in the stress profile. In Fig. 3.32 we have an analytical solution [2] for the stress distribution at the bottom of the asymmetric sand pile, which demonstrates that the numerical simulation results for the stress distribution at the bottom of pile are in good agreement with those of the analytical prediction of the normal stress.

4

Comparison between simulation and analytic theory

4.1 Analytical approaches for sand piles

The next natural step is to compare our simulation results with analytic descriptions purporting to predict the macroscopic behaviour of a sand pile, in order to either validate these descriptions or to show where they fail. There are many macroscopic approaches (continuum models) in the literature including incipient failure everywhere (IFE) [128], Bouchaud-Cates-Claudin (BCC) [129], fixed principal axes (FPA) [13], the family of orientated stress-linearity (OSL) [1] and finally an elasto-plastic model [2] based on an analytic description for describing the stress distribution under a sand pile. However, we have to check amongst those models [128, 129, 13, 1-2], that can predict a stress dip in the centre of a sand pile, in order to compare with our simulation results.

The IFE model suggested that, the sand pile is everywhere at the point of Coulomb failure (point of slip failure). However, while incipient failure is certainly true at the surface of the sand pile, it is not likely to hold in the central region of the sand pile. This model provides either a stress maximum or plateau at the centre. On the other hand, the closure relation proposed by BCC suggested that the horizontal and vertical normal components of stresses are proportional to each other; that means, the ratio of horizontal to vertical normal stress is constant everywhere in the sand pile, this will lead to predict a stress plateau, rather than a dip at the centre of the sand pile. This analytical conclusion turns out to be incorrect since the experimental investigation on the sand pile [14, 15,

130, 12] show that a dip in the stress profile can be found under the tip of the pile. Since the IFE and BCC models fail to account for the stress dip below the tip of the sand pile, we therefore do not compare our simulation results with these two analytical models.

In contrast to BCC and IFE models, models like FPA, OSL, and elasto-plastic continuum models can predict a stress dip in the centre of the sand piles. The closure relation of the FPA model can be derived more intuitively by assuming that the principal axes of the stress tensor take the fixed directions $\pm\psi$ on both sides of the central axis of the sand pile, where $\psi = (\pi - 2\phi)/4$, hence the name of the model is FPA. ϕ is the angle of repose of the sand pile. The orientation of the principal axis of the stress tensor is displayed in figure 4.1. The fixed principal axes model is a special case of the OSL model, to be described in Section 4.4. Moreover, the FPA model leads to a pronounced dip in the pressure distribution under the tip of the sand pile. However, the conclusion of FPA model does not correspond well to the simulations- the orientation of the stress tensor is not constant throughout the sand pile, as was verified by Alexander Schinner in [103]. But the FPA model provides analytical results for the stress tensor that seem to be in very good agreement with the experimental results in three dimensional sandpiles, see ref. [13].

There are two competing macroscopic approaches, whose closure relation might be useful in practice and which we will therefore investigate more closely. One of these is the OSL model which has been constituted by Wittmer, Cates, and Claudin [1] and which leads to globally hyperbolic equations for stresses in a sand pile. The second model is the so-called elasto-plastic continuum model proposed by F. Cantelaube and G. Goddard. The model describes the sand pile as an elasto-plastic continuum, predicting plastic behaviour near the surface of the sand pile and linear elastic behaviour near its centre. In its most stringent form, it has no adjustable parameters.

In this chapter, we focus on comparing our numerical results with those of the analytical theories as OSL model and elasto-plastic continuum model.

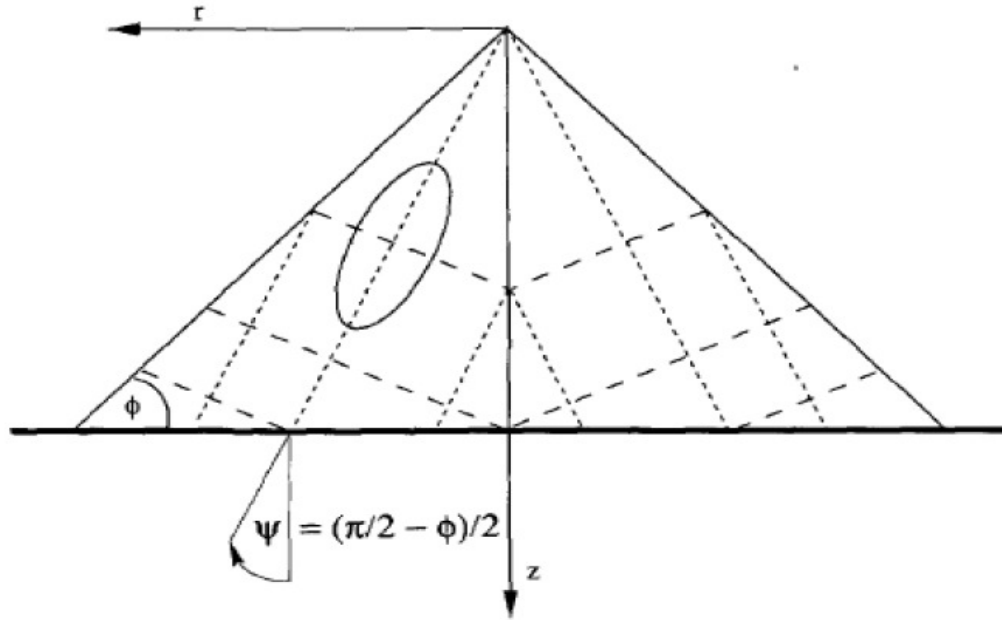


Figure 4.1: Schematic plot of the orientation of the principal axis of the stress tensor in a sand pile, for FPA model [1].

4.2 Basic law of mechanical equilibrium

All analytic approaches for sand pile physics have to respect the basic law of mechanical equilibrium, which in two dimensions reads

$$\begin{aligned} \partial_x \sigma_{xx} + \partial_y \sigma_{xy} &= 0 \\ \partial_x \sigma_{xy} + \partial_y \sigma_{yy} &= -\rho g, \end{aligned} \quad (4.1)$$

where ρ is the density of the sand pile, taken constant in these theories. In our simulation, we have to evaluate this density as the product of the particle density, which is fixed, and the local volume fraction of the sand pile. g is the gravity acceleration.

Moreover, it is generally agreed that the *surface* of a sand pile is in a state of incipient failure, i.e., it corresponds to a slip plane. Using this assumption, one can show that the normal-component free-interface condition $\sigma_{nn} = 0$ leads to the vanishing of *all* stress

components (i.e. $\sigma_{nt} = 0$ and $\sigma_{tt} = 0$). This follows directly from the Mohr-Coulomb yield criterion

$$(\sigma_{xx} - \sigma_{yy})^2 + 4\sigma_{xy}^2 - (\sigma_{xx} + \sigma_{yy})^2 \sin^2 \phi = 0, \quad (4.2)$$

applied in a coordinate system with x parallel to the surface (i.e., replace $x \rightarrow t$, $y \rightarrow n$ in equation 4.2). Herein, ϕ is the internal friction angle (related to the friction coefficient μ via $\tan \phi = \mu$). The assumption of incipient failure provides stress boundary conditions at the surface of the sand pile.

Because the two field equations are insufficient to determine the three independent stress components σ_{xx} , σ_{xy} , and σ_{yy} , a third equation, a so-called closure relation, is needed in order to close the system. In ordinary elasticity, this is provided by constitutive relation connecting stresses and strains.

Usually, the literature states that for sand piles displacement fields are not available, which is true experimentally and also for the macroscopic analysis, as it does not have access to the microscopic particle displacements. Moreover, it is argued that for rigid particles these displacements are not meaningful. Both rigidity and Coulomb friction contribute to static indeterminacy of the pile.

A closure relation between the stress components is then sought for and postulated, to remove this static indeterminacy. Different approaches differ in their postulates concerning this ‘‘constitutive’’ relation. A common assumption of several theories is *radial stress field scaling* (RSF), which seems to be verified in experiments and is essentially based on the idea, that the stress fields of geometrically similar piles should be the same up to a scale factor. Mathematically, this reads

$$\sigma_{ij} = \rho g y s_{ij} \left(\frac{x}{y \cot \phi} \right). \quad (4.3)$$

One can then reduce the mechanical equilibrium equations (4.1) to ordinary differential equations, once a closure relation has been found. In three dimensions, several closure relations are needed – the expression for the divergence of the stress tensor yields only three equations, whereas the stress tensor has six independent components.

We first give a short description in the following section for the elasto-plastic continuum model, and show a comparison of results between simulation and theory. Then in the subsequent section, the OSL model is analyzed briefly.

4.3 Elasto-plastic continuum model

In this approach [2], the authors assumed two types of behaviour in the sand pile, depending on the location of the point considered. Near the surface of the sand pile, plastic behaviour is to be expected, and the closure relation is simply given by Mohr's yield criterion, Eq. (4.2). On the other hand, near the center of the pile, they assume that there is linearly elastic behaviour. The absence of measurable displacements is not a problem, as one can derive within linear elasticity stress compatibility relations, from which the elastic moduli scale out, so the limit $E \rightarrow \infty$ can be easily taken. In two dimensions, there is just one such relationship. It takes the form

$$\sigma_{xx,yy} + \sigma_{yy,xx} - 2\sigma_{xy,xy} = 0, \quad (4.4)$$

and if it is imposed, rigid-body indeterminacy is removed.

Moreover, it is assumed for simplicity that one of the two types of behaviour is realized at any point of the pile, i.e. that there is no transition region in which, for example, non linear elastic behaviour would apply. Whenever a plastic region touches an elastic one, there are boundary conditions, requiring continuity of stresses but allowing discontinuous derivatives. When two elastic regions touch each other with nonmatching stress derivative, an infinitely thin layer of a yield region is assumed between them, along which equation (4.2) holds.

Cantelaube et al. assume RSF scaling as well. They obtain solutions which in the outer plastic domain obey the field equations (4.1) and (4.2), which FPA does near the sand pile surface, too, but strongly differ from FPA behaviour in the elastic core. For symmetric sand wedges, the shape of the inner domain is that of an isosceles triangle with a steeper base angle ($\hat{\beta}$) or a smaller tip angle. They find three discrete solutions, of which one has a pressure minimum, as shown in figure 4.2. Once the angle of repose ϕ of the pile is fixed, the theory contains no free parameters.

One can derive the stress solutions separately for the elastic domain and for the plastic domain by assuming a general linear ansatz, which is as follows

$$\begin{aligned} \sigma_{xx} &= Ax + By, \\ \sigma_{yy} &= Cx + Dy, \\ \sigma_{xy} &= Ex + Fy. \end{aligned} \quad (4.5)$$

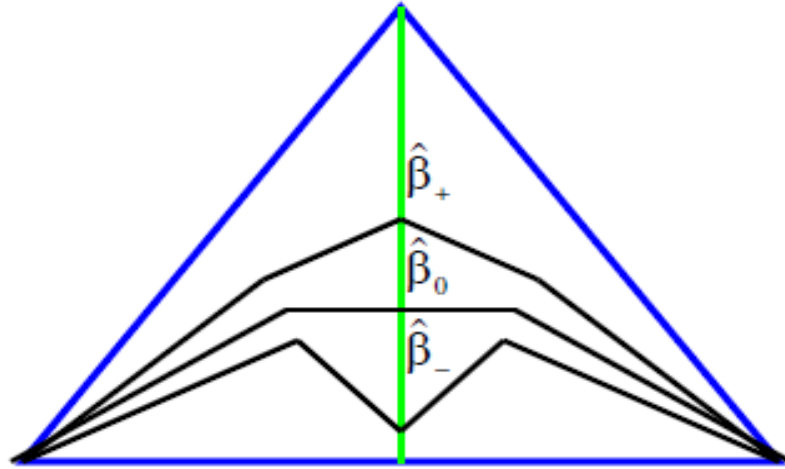


Figure 4.2: Schematic drawing of the pressure profile in a symmetric sand pile. One of the solutions shows a pressure minimum in the centre.

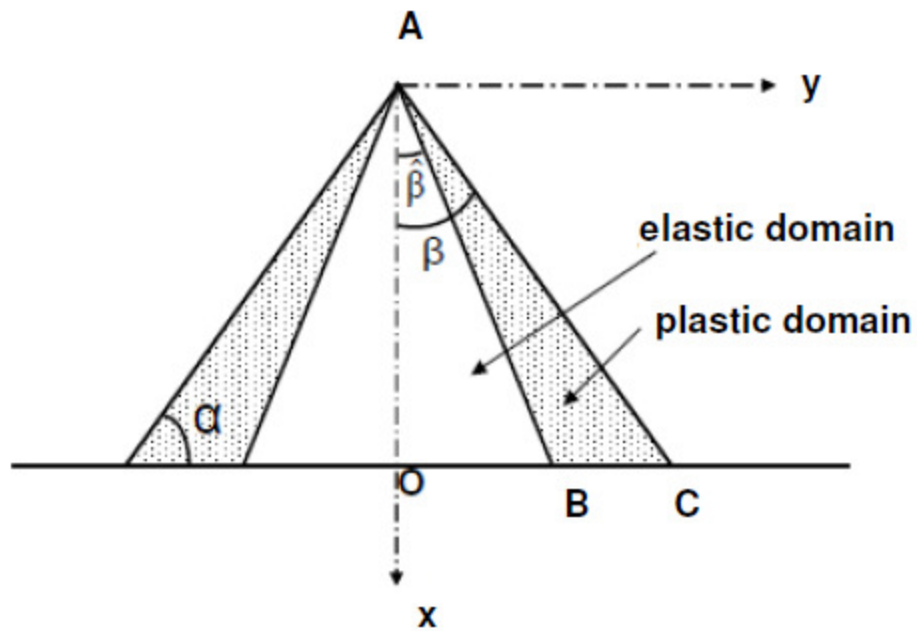


Figure 4.3: Schematic plot of the elasto-plastic model of a symmetric sand pile, where the region AOB represents an elastic domain and the region ABC is a plastic domain.

and by matching the solutions at the domain boundaries. In the elastic domain, the ansatz is seen to automatically satisfy the compatibility relations (4.4).

The orientation of the Cartesian coordinates (x, y) is depicted in figure 4.3, and $A, B, C, D, E,$ and F are six coefficients to be determined.

Solution for the plastic domain:

Inserting the stress components from equation (4.5) into the mechanical equilibrium equation (4.1), now the linear expression (4.5) becomes

$$\begin{aligned}\sigma_{xx} &= Ax + By, \\ \sigma_{yy} &= Cx + Dy, \\ \sigma_{xy} &= -Dx - (1 + A)y.\end{aligned}\tag{4.6}$$

It is noted that the stress components are required to vanish at the free surface $y = \tan \beta x$,

$$\text{i.e., } \sigma_{xx} = \sigma_{xy} = \sigma_{yy} = 0 \text{ for } y = \tan \beta x.\tag{4.7}$$

In the next step, using the values of the components of the stress tensor at the free surface as given in equation (4.7) and subsequently, applying the Mohr-Coulomb yield criterion closure equation (4.3), one can derive the solution for the plastic domain $\beta = (\pi/2 - \phi)$: which is given by the following expressions

$$\begin{aligned}\sigma_{xx} &= a_{11} \left[\frac{|x|}{\tan \beta} - y \right], \\ \sigma_{yy} &= a_{22} \left[\frac{|x|}{\tan \beta} - y \right], \\ \sigma_{xy} &= \pm a_{12} \left[\frac{|x|}{\tan \beta} - y \right],\end{aligned}\tag{4.8}$$

where the parameters a_{11}, a_{12} and a_{22} are given by

$$\begin{aligned}a_{11} &= 1 + \cos^2 \beta, \\ a_{22} &= \sin^2 \beta, \\ a_{12} &= \frac{1}{2} \sin 2\beta.\end{aligned}\tag{4.9}$$

Solution for the elastic domain:

According to this model, one can assume that the stress components $\sigma_{xx}, \sigma_{xy}, \sigma_{yy}$ are continuous along the line $y = \tan \hat{\beta}x$, which means that the plastic solution, Eq. (4.8), must match with the elastic one given by equation (4.6). This yields boundary conditions:

$$\begin{aligned} Ax + By &= a_{11} \left(\frac{\tan \hat{\beta}}{\tan \beta} - 1 \right) x, \\ Cx + Dy &= a_{22} \left(\frac{\tan \hat{\beta}}{\tan \beta} - 1 \right) x, \\ -Dx - (1 + A)y &= a_{12} \left(\frac{\tan \hat{\beta}}{\tan \beta} - 1 \right) x. \end{aligned} \quad (4.10)$$

Equation (4.10) gives us three equations for the four parameters A, B, C, D . So we can reduce the solutions to a single free parameter. This parameter is then fixed by continuity at the line $x = 0$ with or without a yield line imposed there.

$$\begin{aligned} \sigma_{xx} &= (a_2 - 1)y, \\ \sigma_{yy} &= (a_1 - 1)y + b_1 |x|, \\ \sigma_{xy} &= -a_1 x, \end{aligned} \quad (4.11)$$

where the elastic parameters a_1, b_1 and a_2 are as follows

$$\begin{aligned} a_1 &= -\cos \beta \sin \beta \left(\frac{1}{\tan \beta} - \frac{1}{\tan \hat{\beta}} \right), \\ b_1 &= \frac{1}{\tan \beta} + \left(\cos^2 \beta + \cos \beta \frac{\sin \beta}{\tan \hat{\beta}} \right) \left(\frac{1}{\tan \beta} - \frac{1}{\tan \hat{\beta}} \right), \\ a_2 &= 1 + \sin^2 \beta \left(\frac{\tan \hat{\beta}}{\tan \beta} - 1 \right). \end{aligned} \quad (4.12)$$

Here $\hat{\beta}$ is still a free parameter.

Imposing either continuity of the components of the stress tensor and their derivatives or only continuity of the components and validity of (4.2) along $x = 0$, one can determine the angle $\hat{\beta}$ that separates the elastic and plastic boundary from one of the following relations:

$$\begin{aligned} \tan \hat{\beta} &= \frac{\sin \beta}{(1 - \cos \beta)^2} \left[\sqrt{1 + (1 - \cos \beta)^2} - 1 \right] && (\hat{\beta}_-) \\ \tan \hat{\beta} &= \frac{\sin \beta}{(1 + \cos \beta)^2} \left[\sqrt{1 + (1 + \cos \beta)^2} + 1 \right] && (\hat{\beta}_+) \\ \tan \hat{\beta} &= \frac{\sin \beta}{\sqrt{1 + \cos^2 \beta}} && (\hat{\beta}_\circ) \end{aligned} \quad (4.13)$$

which provides us with the three possible solutions, sketched in Fig.4.2.

In order to check the validity of prediction of the theory, we determine a best fit of the parameters of the analytical stress expressions (4.8) and (4.11) to the numerical simulation data of sand piles constructed from a point source using a least-square fit. We obtain the fitted solution for the elastic domain for an average over nine sand piles.

$$\begin{aligned} a_1 &= 0.34, \\ a_2 &= 0.49, \\ b_1 &= -0.2. \end{aligned} \quad (4.14)$$

where as the solution for the plastic domain is given by

$$\begin{aligned} a_{11} &= 1.23, \\ a_{22} &= 0.78, \\ a_{12} &= 0.38. \end{aligned} \quad (4.15)$$

The theory predicts that the sum of the parameters a_{11} and a_{22} from Eq. (4.9) must be equal to 2, a relationship that may serve as a consistency check. This is well satisfied as one can see in (4.15). If we consider the elasto-plastic approach as a theory with a fit parameter, the agreement with the simulations is quite satisfactory, as we shall see now.

The figure 4.4 compares the stress distributions from the numerics with those of the theory for the sand pile constructed from a point source. On the same plot, we present horizontal, vertical normal stress and shear stress at the bottom layer of the sand pile. The solid lines represent theoretical results and data points with lines numerical results. The comparison shows very good agreement with our numerical data.

However, for symmetric sand piles the theory does not contain any free parameters. In particular, it predicts the angle $\hat{\beta}$, which for $\phi = 28^\circ$, the angle of repose in our simulations from a point source, should be 22° for the solution producing a dip, but the fits shows good agreement only if the tip angle of the triangle delimiting the elastic domain is equal to (twice) 35° . Indeed, a pressure minimum can be produced this way, but the angle separating the plastic and the elastic domains does not agree well with the angle calculated from the theory. So as a theory with a free parameter the Cantelaube approach appears to work well, but its calculation of the relative sizes of the elastic and plastic domains does not agree well. This means that some of its assumptions must be incorrect.

Similarly, we determine a best fit of the parameters of the analytical stress expressions (4.8) and (4.11) to the numerical data for the sand pile constructed from a line source and we obtain the fitted solution for the elastic domain for an average over six sand piles.

$$\begin{aligned} a_1 &= 0.15, \\ a_2 &= 0.64, \\ b_1 &= 0.27. \end{aligned} \tag{4.16}$$

where as the solution for the plastic domain reads

$$\begin{aligned} a_{11} &= 1.20, \\ a_{22} &= 0.79, \\ a_{12} &= 0.39. \end{aligned} \tag{4.17}$$

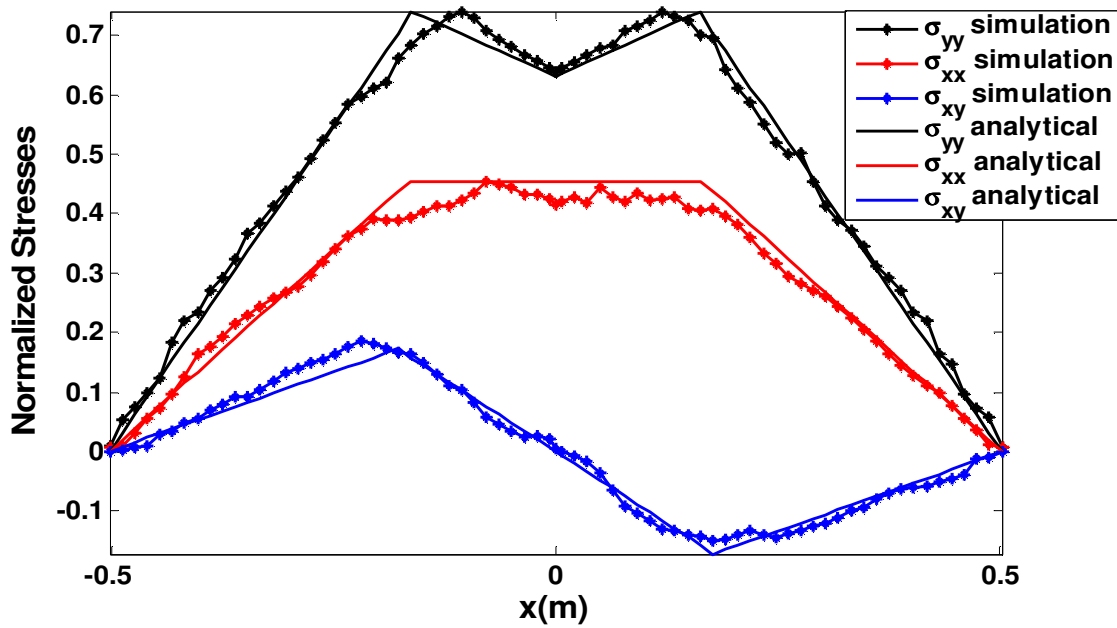


Figure 4.4: Comparison of simulation data with the analytic theory for sand piles that are constructed from a point source.

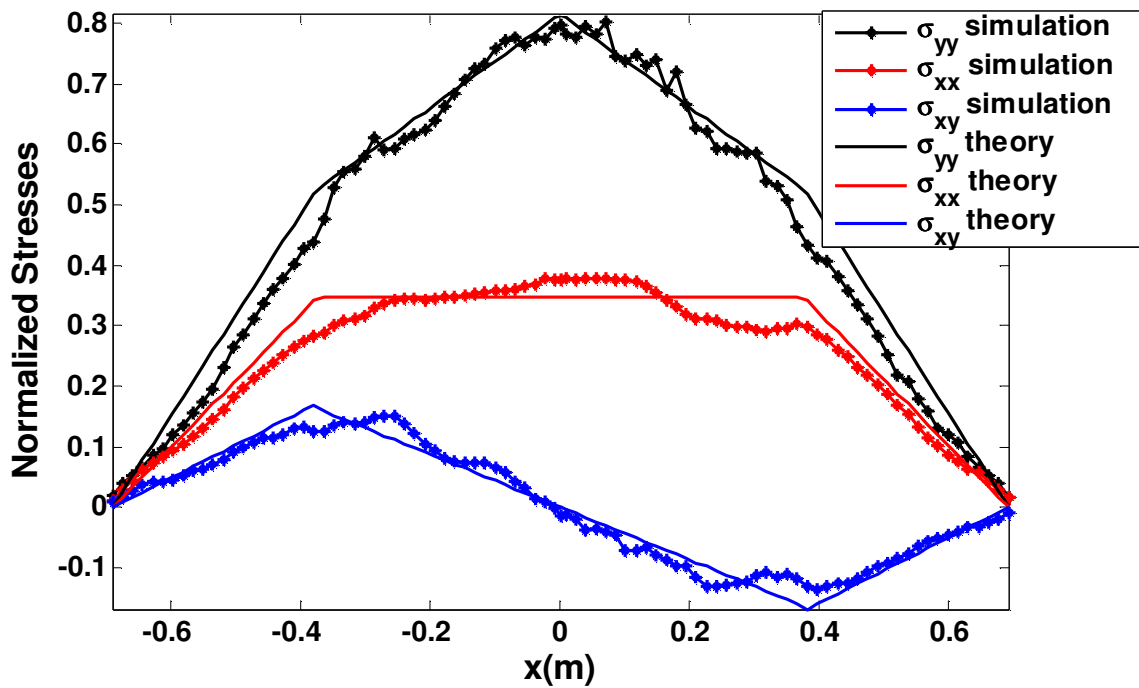


Figure 4.5: Comparison of simulation data with the analytic theory for sand piles that are constructed from a line source.

In this case, the sum of two parameters a_{11} and a_{22} is approximately equal to 2 as well, as one can see in (4.17). The comparison of results between the simulation and those of the analytical theory for sand piles constructed from a line source is represented in figure 4.5. On the same plot we present horizontal, vertical normal stress and shear stress at the bottom layer of the sand pile. Solid lines represent theoretical results and data points with lines numerical results. As can be seen in the figure, our simulation results are in very good agreement with the theory.

In this case, the solution produces a plateau at the centre, appropriately describing sand piles constructed from a line source. The best fit shows good agreement for the angle $\hat{\beta} = 49^\circ$, and the angle calculated from the theory, from equation (4.13), is also 49° , for the angle of repose of the simulated sand pile $\phi = 26^\circ$, which is very good agreement. So the Cantelaube approach appears to work well for the symmetric sand pile constructed from a line source, even without free parameters.

In conclusion, the elasto-plastic continuum model seems capable of both predicting the stress minimum at the centre of the sand pile constructed from a point source and predicting a stress plateau for a line source sand pile. However, the angle which separates the elasto-plastic boundary does not agree well with the angle calculated from the theory for a point source sand pile, displaying a pressure dip.

A reason why the theory does not work as well for the solution that is discontinuous at the centre of the pile is that its assumption of a yield line along the axis of the pile is not really satisfied. This can be seen from Fig. 4.6, where we evaluated the expression on the left-hand side of Eq. (4.2) as a function of the lateral sand pile coordinate for several heights in the sand pile, which should become zero in the plastic regions. Clearly, it approaches zero far from the center of the pile ($x = 0$), so the existence of plastic regions near the surface of the pile can be confirmed (though not their triangular shape), but there is little indication of singular behaviour of the expression near the center of the pile. For the plateau solution, there is no such singular behaviour even in the theory, which may explain why it works so well.

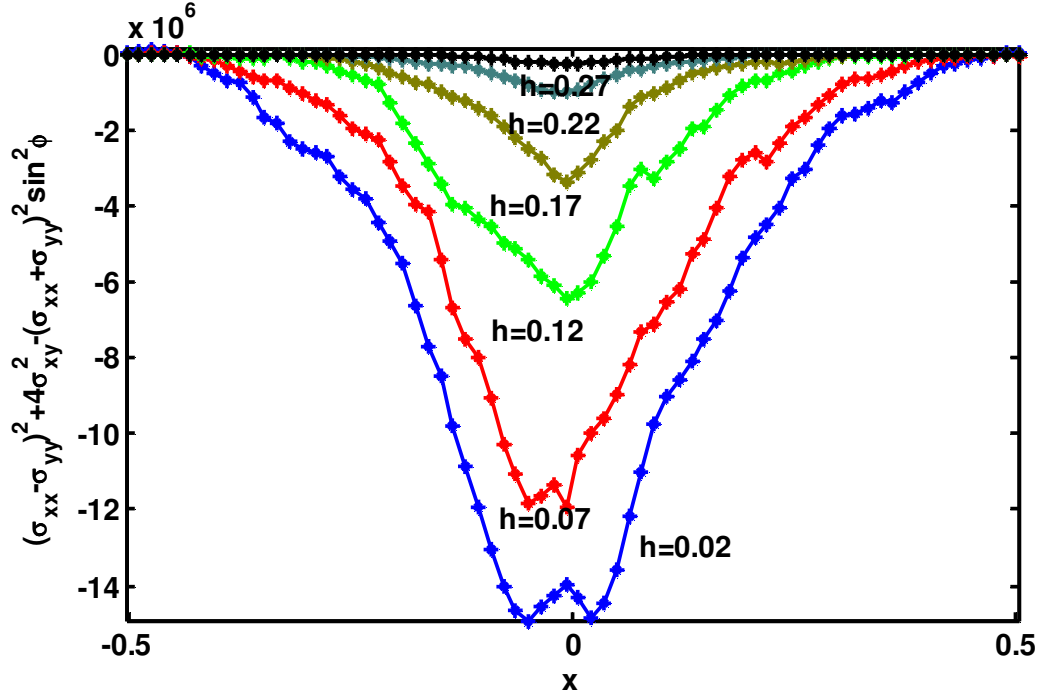


Figure 4.6: The Coulomb-Mohr expression (4.2) evaluated for different heights in the sand pile, averaged over five sand piles constructed from a point source. On the plot, the blue curve shows the results at the bottom layer, whereas the black curve corresponds to the highest layer of the sand pile.

4.4 Orientated stress linearity model

In this section, we study another continuum model for the stress tensor, the oriented stress linearity (OSL) model, proposed by Wittmer et al. [1] that created a lot of stir in the 90s. Unlike the elasto-plastic continuum model, the OSL model contains an adjustable parameter, leading to a continuous family of closure relations of the form

$$\sigma_{nn} = K \sigma_{mm}, \quad (4.18)$$

where K is a constant, σ_{nn} and σ_{mm} are the principal stress components along two orthogonal directions n and m , oriented at a prescribed fixed angle, the parameter of the family, with respect to the basic xy coordinate system. The OSL model has a linear relation between the normal components of the stress tensor like the BCC model. The most

interesting of these OSL models as it seemed to be justifiable more easily as a natural form incorporating the construction history of the sand pile, was the so-called *fixed-principal axis* model (FPA). It is given by $K = 1$ and the angle of the coordinate axis, along which σ_{nn} is to be measured, being equal to $\tau = (\pi - \phi)/2$.

In a tilted coordinates system (m, n) , with inclined angle τ to the vertical, the stress components are:

$$\begin{aligned}\sigma_{nn} &= \cos^2(\tau)\sigma_{xx} + \sin^2(\tau)\sigma_{yy} - 2\sin(\tau)\cos(\tau)\sigma_{xy} \operatorname{sign}(x) \\ \sigma_{mm} &= \sin^2(\tau)\sigma_{xx} + \cos^2(\tau)\sigma_{yy} + 2\sin(\tau)\cos(\tau)\sigma_{xy} \operatorname{sign}(x) \\ \sigma_{mn} &= -\sin(\tau)\cos(\tau)(\sigma_{yy} - \sigma_{xx}) + (\cos^2(\tau) - \sin^2(\tau))\sigma_{xy} \operatorname{sign}(x),\end{aligned}\tag{4.19}$$

with σ_{nn} and σ_{mm} denote the horizontal and normal component of the stress tensor, respectively.

Part of the debate about the model came from the fact, that with a closure relation such as (4.18), the field equations for the stress tensor became hyperbolic throughout the volume of the whole sand pile, corresponding to isostaticity.

The constitutive equations proposed by Wittmer et al. depend on quantities including the scaling variable, components of the stress tensor on the free surface, that means, the individual components of the stress tensor have to vanish at the free surface, and the limiting value of ratio between horizontal stress and vertical stress, which is fixed when the free surface is approached and also limiting value of ratio between shear stress and vertical stress that becomes fixed when the free surface is approached.

The scaling variable $S = \frac{x}{cy} = \frac{x \tan \phi}{y}$ is unity on the free surface and becomes zero at the centre of the sand pile, where ϕ is the internal friction angle (angle of repose) of the sand pile, as shown in figure 4.7.

According to the IFS (incipient failure at the surface) boundary condition, the components of the stress tensor at the free surface must be equal to zero:

$$\sigma_{xx}(S=1) = \sigma_{yy}(S=1) = \sigma_{xy}(S=1) = 0,\tag{4.20}$$

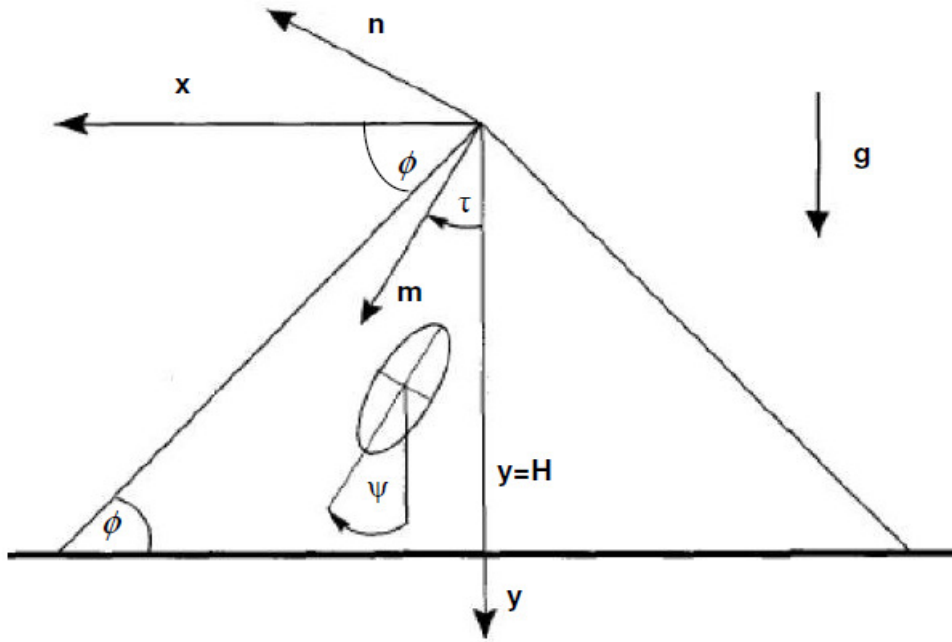


Figure 4.7: OSL Coordinates systems of the two-dimensional sand pile [1].

and in addition, since the surface of the sand pile is a slip plane, the components of the stress tensor not only vanish at the surface, but also their ratio is fixed when the surface is approached. One has the conditions:

$$\lim_{S \rightarrow 1} \frac{\sigma_{xx}(S)}{\sigma_{yy}(S)} = \eta_0, \quad (4.21)$$

$$\lim_{S \rightarrow 1} \frac{\sigma_{xy}(S)}{\sigma_{yy}(S)} = \tan(\phi),$$

$$\text{with } \eta_0 = \frac{1}{1 + 2 \tan^2 \phi}.$$

The basic constitutive equation for the OSL model is a connection between the individual components of the stress tensor.

$$\frac{\sigma_{xx}}{\sigma_{yy}} = \eta + \mu \operatorname{sign}(x) \frac{\sigma_{xy}}{\sigma_{yy}}. \quad (4.22)$$

Moreover, the parameters η and μ satisfy:

$$\eta = \frac{K - \tan^2 \tau}{1 - K \tan^2 \tau} \quad \text{and} \quad \mu = \frac{2(K + 1) \tan^2 \tau}{1 - K \tan^2 \tau}. \quad (4.23)$$

Note that consistency of the OSL model requires the following relationship between in two parameters:

$$\eta = \eta_0(1 - \mu \tan \phi) = \frac{1}{1 + 2 \tan^2 \phi} (1 - \mu \tan \phi), \quad (4.24)$$

where ϕ is the angle of repose of the sand pile. Whether the OSL model may describe numerical data consistently, can be decided immediately after the evaluation of η and μ . Because the parameters η and μ in the OSL model are not independent, the model is a one-parameter family, not a two-parameter one.

There are two special cases for the orientated stress linearity (OSL) model. Parameters $\eta = \eta_0 = \frac{1}{1 + 2 \tan^2 \phi}$ and $\mu = 0$ corresponds to the BCC model, whereas $\eta = 1$ and $\mu = -2 \tan \phi$ correspond to the FPA model.

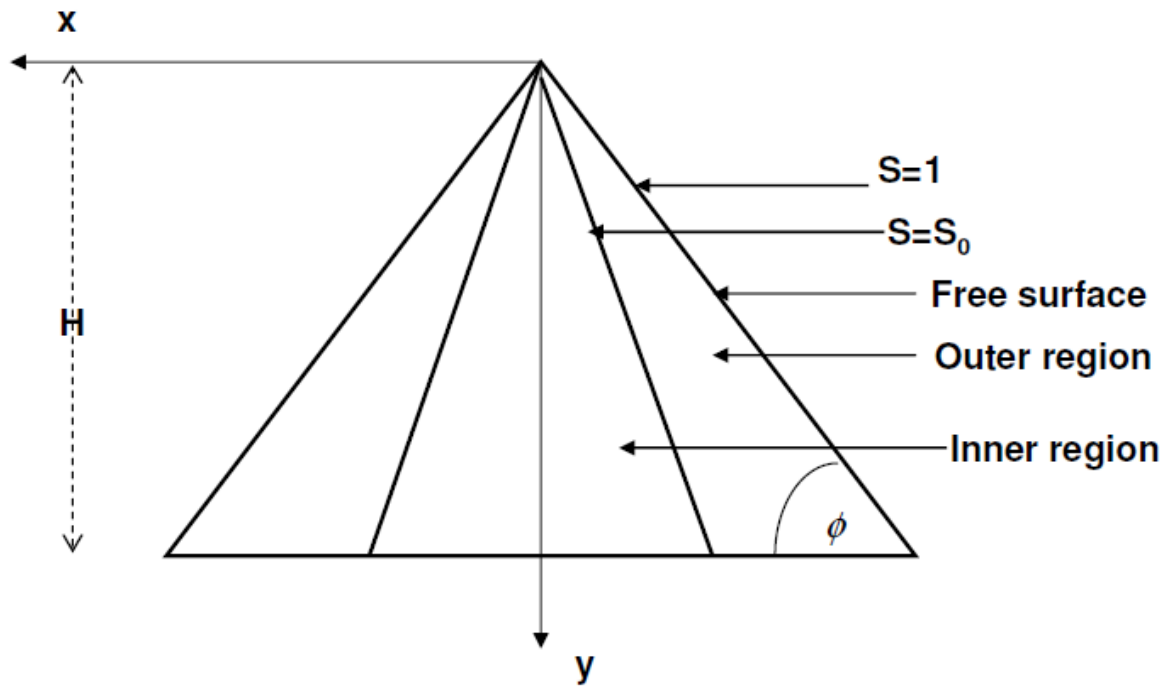


Figure 4.8: Schematic plot of the symmetrical sand pile, the scaling variable S is unity at the free surface, inner and outer region meet at the boundary $S=S_0$ and H is the height of the sand pile.

One can derive the stress solutions for the OSL model by inserting the OSL constitutive relation (4.22) into the stress mechanical equilibrium equation (4.1), which yields

$$\begin{aligned}\partial_x(\eta\sigma_{yy} + \mu \operatorname{sign}(x)\sigma_{xy}) + \partial_y\sigma_{xy} &= 0 \\ \partial_x\sigma_{xy} + \partial_y\sigma_{yy} &= g.\end{aligned}\tag{4.25}$$

Equation (4.25) can be rewritten (in each of the domains $x > 0$ and $x < 0$) as a wave equation of the form

$$(\partial_y - c_1\partial_x)(\partial_y - c_2\partial_x)\sigma_{ij} = 0,\tag{4.26}$$

where c_1 and c_2 , respectively, denote the positive and negative roots,

$$c_1 = \frac{1}{2}(\mu + \sqrt{\mu^2 + 4\eta}) \quad \text{and} \quad c_2 = \frac{1}{2}(\mu - \sqrt{\mu^2 + 4\eta}).\tag{4.27}$$

In the next step, by assuming radial stress field scaling and applying IFS boundary conditions, equations (4.20) and (4.21), one can simplify equation (4.25), which yields the stress expression in the outer region, meeting the inner region at ($S = S_0 = \frac{c_1}{c}$), see figure 4.8.

The stress solution in the outer region is

$$\begin{aligned}s_{yy} &= s^*(c - \mu)(1 - S), \\ s_{xx} &= s^*\eta c(1 - S), \\ s_{xy} &= \operatorname{sign}(x)s^*\mu(1 - S),\end{aligned}\tag{4.28}$$

where s^* is a constant, $s^* = \frac{c}{c^2 - \mu c - \eta}$.

On the other hand, the stress solution in the inner region ($0 \leq S \leq \frac{c_1}{c}$) is:

$$\begin{aligned}
 s_{yy} &= s^* \frac{(c-c_1)}{c_1} (c_1 - \mu S), \\
 s_{xx} &= s^* \eta c_1 \frac{(c-c_1)}{c_1}, \\
 s_{xy} &= \text{sign}(x) s^* \eta S \left(\frac{c-c_1}{c_1} \right).
 \end{aligned}
 \tag{4.29}$$

In the next step, in order to complement the analytical results of the OSL model, we find a best fit parameter of the OSL closure relation (4.22) with our simulation data for sand piles constructed from a point source and we obtain the fitted solution of the parameters η and μ for an average over nine sand piles.

$$\begin{aligned}
 \mu &= -0.31, \\
 \eta &= 0.74.
 \end{aligned}
 \tag{4.30}$$

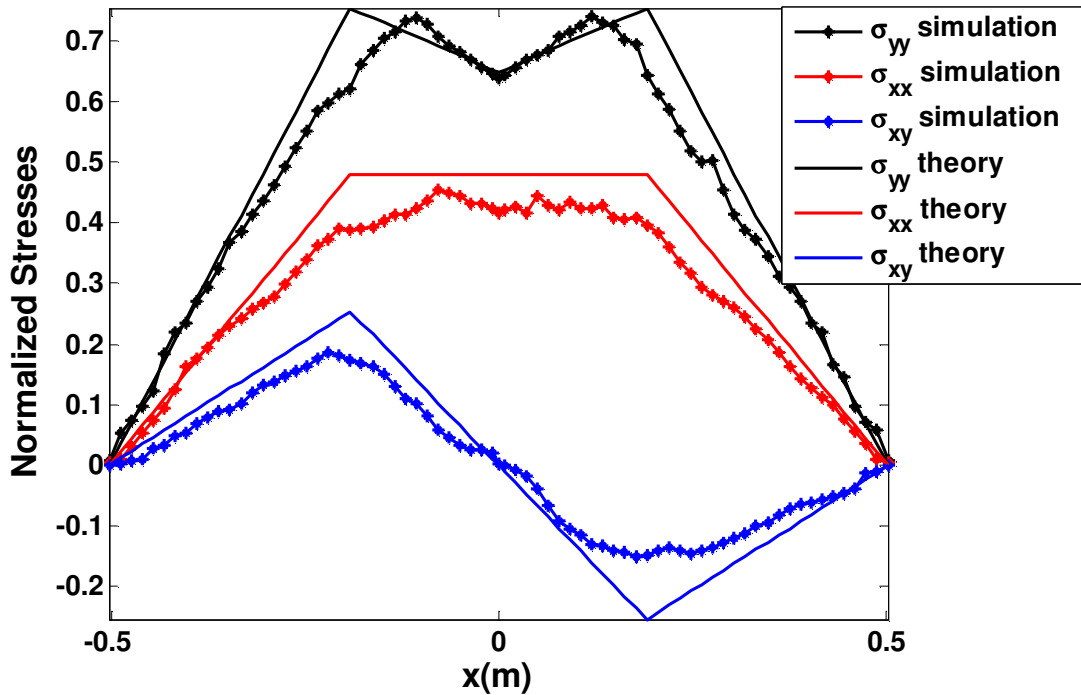


Figure 4.9: Fit of the components of the (negative) stress tensor predicted by the OSL model to the point source simulations, the components of the stress tensor are plotted for the bottom layer of the sand pile.

For a given angle of repose $\phi = 28^\circ$ one can now check the consistency condition (4.24) using the fitted solution (4.30). We have checked and confirmed that the fitted solution satisfy the consistency equation of the OSL model.

Once we have the solution for the parameters η and μ , then it is easy to determine the proportionality coefficient K using the following expression:

$$K = \left(1 + 2 \frac{(1-\eta)^2}{\mu^2 + 4\eta}\right) \pm \sqrt{\left(1 + 2 \frac{(1-\eta)^2}{\mu^2 + 4\eta}\right)^2 - 1}. \quad (4.31)$$

Inserting the fitted solution $\mu = -0.31$ and $\eta = 0.74$ in (4.31), we find $K = 1.345$.

For a given angle of repose, there is a relationship between the two parameters K and τ , given in the following expression, so this is essentially a one-parameter fit.

$$\tau = \tan^{-1} \sqrt{\frac{K - \eta}{1 - \eta K}}. \quad (4.32)$$

We find the angle $\tau = 85^\circ$.

Comparison results between simulation and the theory are presented in figure 4.9. It can be seen that, the simulation results are in very good agreement with the analytical theory for the fitted parameters $\mu = -0.31$ and $\eta = 0.74$.

5

Stress response of a static rectangular layer of a granular material

We studied and analyzed the stress distribution under a sand pile in chapter three. To a certain extent, even more interesting than studying the stress tensor under a granular heap is to determine the stress response to a force perturbation for a rectangular layer of granular materials. In a real system, the packings of granular materials usually do not exist in an ordered state. Therefore, determining the vertical normal stress response function to an applied overloads acting on a single grain at the top surface of the granular assembly has been one of the problematic phenomena of granular materials in physics community. In the last few years, many researchers have been involved in studying this phenomenon both experimentally in refs. [131-135] and theoretically [136-138].

The stress response to a point force under assemblies of grains displays some puzzling properties. In some cases, it shows wave-like propagation underneath the point where the force is applied and in others the response is elastic (isotropic elasticity). What is observed depends strongly on the packing structure of the granular assembly. For packings with strong spatial order, the stress response has a double-peak shape underneath the point where the force is applied, which corresponds to wave-like behaviour describable by hyperbolic continuum equations [1, 13,137,139], whereas when the amount of disorder increases, meaning that the packing has large contact disorder, then there is a single peak, hinting at an elastic-like response, describable by elliptic continuum equations. In the theory of elasticity [140], the shape of the stress response reveals a single central peak. The width of the response increases with the height of the system below the point of application of the external overload.

Both cases have been observed in experimental models set up by Junfei Geng et al. [131] using photo-elastic polymer material. Hence two rectangular systems consisting of the same material may have different stress responses to a point force, depending on the way they were arranged.

Moreover, the coefficient of static friction plays an important role in the stress response of a rectangular system. When the static friction coefficient is very small, the stress response to an external overload may have a double-peaked shape. On the other hand, if it is very large, the double peak shape may be present but much less pronounced, as has been observed experimentally in ref. [133] for rectangular packings with different friction coefficients.

We focus on investigating numerically the mechanical properties of a static granular assembly, especially, to check how the granular material responds to an applied overloads acting on a single grain at the top surface of the granular assembly. We determine the stress response for a rectangular system of granular material with different amounts of disorder, particle packed in a regular rectangular lattice with different frictional properties, and different values of the applied vertical force. This study has been done by use of a DEM numerical simulation generating granular packings with different packing order consisting of soft convex polygonal particles. The simulation was performed in two-dimensional systems.

This chapter is organised as follows. In the first Section 5.1, we first describe some details of the simulation geometry constructed from round particles. In Section 5.2, we show the angular distribution of the contact forces for different packings. We then present simulation results for the stress response of two dimension rectangular layers of particles for various packing orders in Section 5.3, including a qualitative comparison with experimental results. The stress response for different values of static friction and different values of the applied external overload is discussed in Section 5.4. Next, Section 5.5 is devoted to the calculation of the stress response for poly-disperse system with smooth bottom as well as rough bottom. Comparison is made with existing experimental results. Then we perform a quantitative comparison between simulation data for the stress response and isotropic elasticity prediction of stress response in Section 5.6. In the last Section 5.7 of this chapter, the calculation of the macroscopically averaged strain response function inside granular aggregate will be presented.

5.1 Simulation geometry

In order to complement the experimental data, we have performed extensive numerical simulations of various grain packings by layer wise deposition of particles. To construct packings of varying degrees of spatial order, we simulated four different types of samples by constructing them from mono-disperse, bi-disperse, irregular pentagons as well as poly-disperse mixtures of roundish particles. We used soft particles with convex shape for our simulation system. For the mono-disperse distribution, we used mixtures of round particles with a diameter of 0.9 cm. In a bi-disperse system, we used mixtures of two round particle types with diameters of 0.9 cm and 0.7 cm, respectively. The pentagons had the same side length of 0.9 cm and for the poly-disperse distribution, the radius of the particles was distributed uniformly between 0.36 cm and 0.54 cm.

Particles were deposited into a rectangular system in a layer-wise manner under gravity either on a rough bottom or a smooth bottom. The simulated rectangular system consists of several thousand round particles. A snapshot of the simulated rectangular layers that consists of a mono-disperse mixture of round particles is shown in Fig. 5.1, where the particles have been deposited on a smooth bottom, arranged on a triangular lattice, each particle has six nearest neighbours.

The aspect ratio of the rectangular layers of the granular material is about approximately 1:4 (64 particles wide and 16 deep) for the mono-disperse packing, we also consider the same aspect ratio for the remaining packings. This size of the aspect ratio is usually needed in order to study the response function appropriately. It is to be noted that the number of particles (number of layers) of each packing is not necessarily same, but we choose the aspect ratio of each packing to be the same in this work.

Once the assembly is ready, we apply an overload (using a piston) to a single grain at the top surface of the system. This force is vertically downward. The arrangement is displayed in Fig. 5.2 for a smooth bottom, and in Fig. 5.3 for a rough bottom. The external overload (point force) is very small enough so as to not cause any rearrangement of the layer structure, which means that no contacts are either created or broken during overloading. We have checked that the overloading does not lead to any rearrangements of the packing. While applying an overload with piston, one should pay attention considering the velocity of the piston. If one chooses a too large velocity, the piston might enter inside the granulate, which will destroy the contact network locally. Therefore, the velocity of the piston must be small in order to avoid such a situation. We have taken a piston velocity of 0.01 m/s , which turned out to be small enough. The parameters which we have used for the simulation of rectangular systems are represented in Table 5.1. Note that the friction coefficient is the same for all the packings as we choose a static friction $\mu_s = 0.5$ for the packing of mono-disperse, bi-disperse and pentagonal system. We note that the thickness of the rectangular layers is 15 cm.

However, the friction coefficient is changed later when we calculate the stress response of mono-disperse packings for different values of friction coefficient, as will be discussed in Section 5.4.

The detailed description of the DEM method and numerical integration scheme has been represented in Chapter two.

Table 5.1. The material properties and the values of parameters used in our simulation are given in the following table.

Name of variable	Symbol	Value
Static friction	μ_s	0.5
Dynamic friction	μ_d	0.5
Material density	ρ	$5 \times 10^3 \text{ kg/m}^2$
Young's modulus	E	10^7 N/m
Damping coefficient	γ	0.75
Time step	Δt	$2 \times 10^{-6} \text{ s}$
Degree of poly-dispersity	Δr	0.3
Size of particle (mono-disperse)	R	0.9 cm
Size of particle (bi-disperse)	(R_{small}, R_{big})	(0.7 cm, 0.9 cm)
Size of particle (pentagons)	R	0.7 cm
Size of particle (poly-disperse)	(R_1, R_2)	(0.36 cm, 0.54 cm)
Velocity of the piston	V	0.01 m/s
Applied external overload	F	300 N
Angle of the application of an overload	θ	90°

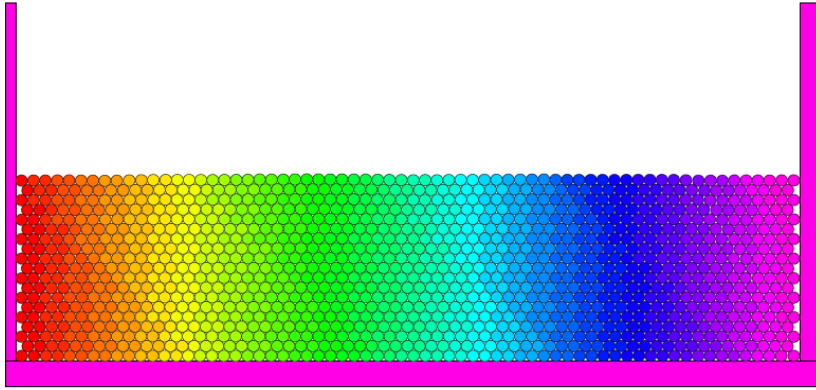


Figure 5.1: Snapshot of a simulated rectangular system that consists of mono-disperse mixture of particles, where the particles placed on a smooth bottom.

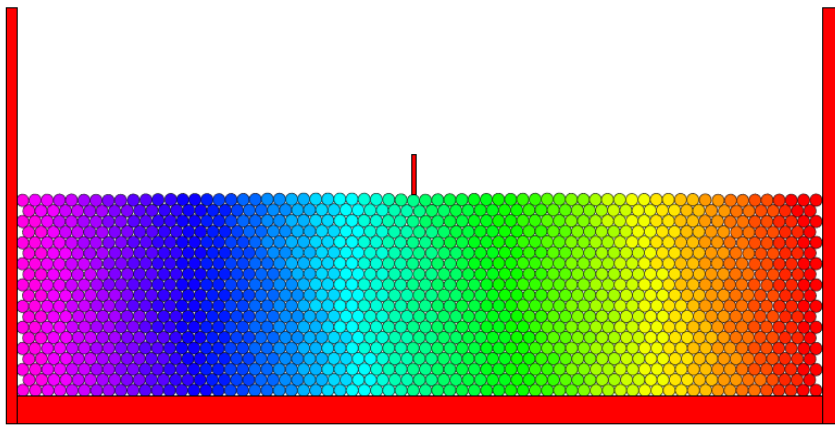


Figure 5.2: Simulated rectangular layer of mono-disperse mixture of particles with smooth bottom with an applied load to a single grain at the top surface of the system.

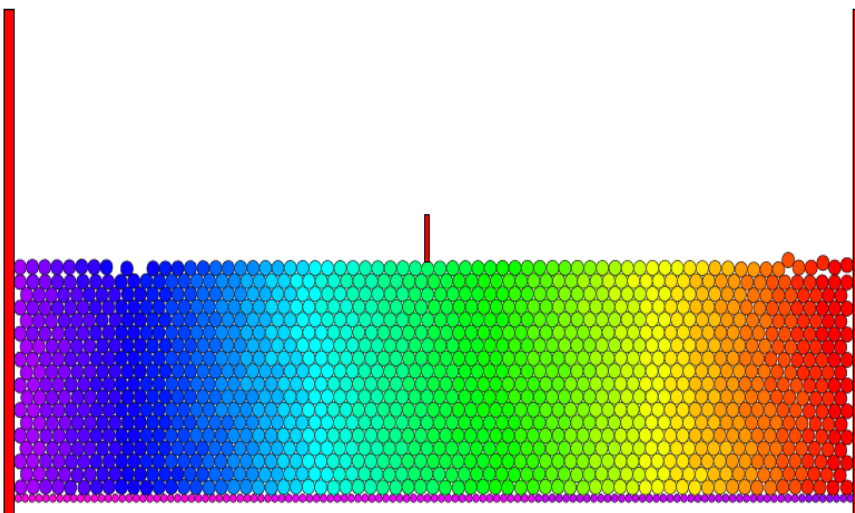


Figure 5.3: Simulated rectangular layer of soft particles with rough bottom.

5.2 Contact force angle distribution

We then carried out a microscopic characterization of the rectangular layers computing the contact force angle distribution. The polar diagrams of the angular distribution of all contact forces for different packings obtained from the simulation are displayed in Fig. 5.4. All angles are measured with respect to the horizontal axis. Ostensibly, the orientations of the contact forces are different for the different packings. The mono-disperse packing is highly ordered, because the forces are mostly oriented along a few fixed directions given by multiples of 60 degree. The contact disorder of the remaining packings is increasing from the bi-disperse packing via the pentagonal to the poly-disperse packing. For poly-disperse packing, the sample is highly disordered, since the angles of the contact force are much closer to an isotropic orientation distribution.

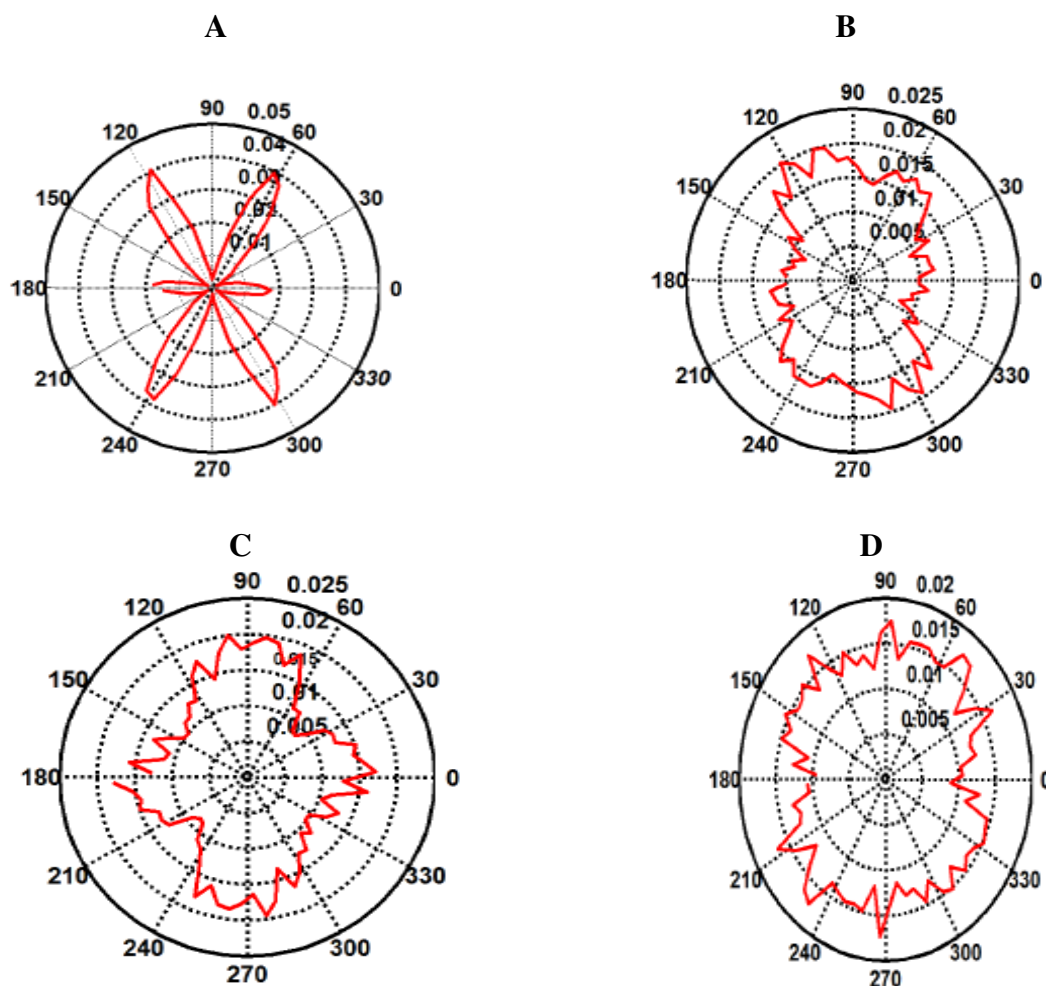


Figure: 5.4 Contact force angle distribution of the particles for the different packings. **A**, for mono-disperse packing. **B**, for bi-disperse packing. **C**, for pentagonal packing. **D**, for poly-disperse packing.

5.3 Simulation results of stress responses for different packings

Once we have the forces and their points of contact, we can determine a formal stress tensor of a single particle, and then it is easy to determine the averaged stress tensor over many particles in a representative volume element. How this stress tensor for single particle and its averaged quantity are determined is explained in detail in Chapter 2. The stress response function is obtained by taking the difference of the stress distribution measured on the rectangular layers with additional external overload and the stress distribution of the same rectangular layers without overload.

$$\sigma_{ij}(x, y) = \sigma'_{ij}(x, y) - \sigma''_{ij}(x, y). \quad (5.1)$$

Here, $\sigma'_{ij}(x, y)$ and $\sigma''_{ij}(x, y)$ are respectively the averaged stress tensor at the point position (x, y) of the layer without external load and with external load. The averages results we have taken over many realizations in order to suppress the fluctuation of the single realization.

On the left-hand side of the Fig. 5.5, we present our simulation results for the average vertical normal stress response at different heights of the sample that contains a mixture of mono-disperse particles. It can be seen that at large distance from the perturbing force, the vertical normal stress response has a double peak underneath the point where it is applied, a behaviour which is predicted by hyperbolic continuum equations such as those from the model of oriented stress linearity (OSL) [1]. For small depths, these two peaks merge into a single broad peak. We compare our simulation results with the available 2D experimental results by Junfei Geng et al. [131] given on the right-hand side of the figure. Experiments were carried out on 2D rectangular systems consisting of mono-disperse, bi-disperse and pentagonal mixtures of particles, particles were cut a photo elastic materials. This comparison shows that the responses are qualitatively similar, but do not agree quantitatively.

In the next figure, Fig. 5.6, we plot the vertical normal stress response for the bi-disperse packing at the same heights of the sample as for the mono-disperse packing. The double peaks are also present for this case, but much less pronounced than for the mono-disperse packing. The Fig. 5.7 shows the simulation results of vertical normal stress response for the sample of pentagonal packing at different heights of the sample. The vertical normal stress response shows no evidence for wave-like stress propagation. It has the form of a bell-shaped curve with a single peak at each layer of the sample and the width of the response increases very slowly with the distance from the perturbation point. Comparison with the experimental results presented on the right hand side of the simulation figure shows that the responses are qualitatively similar.

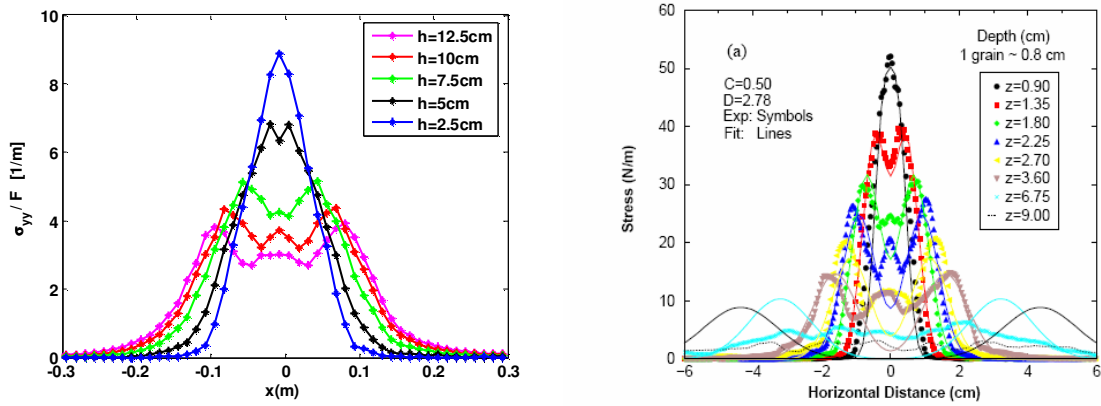


Figure 5.5: Vertical normal stress response at different depths of the system consisting of a mono-disperse assembly of particles.

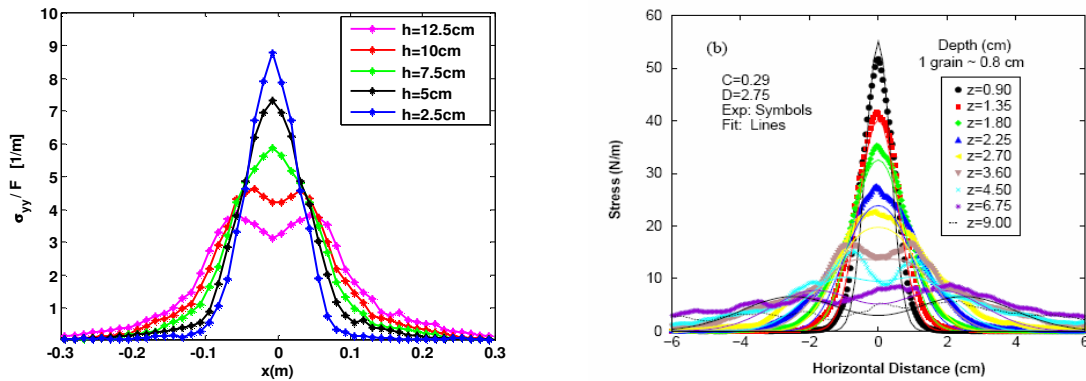


Figure 5.6: Vertical normal stress response at different depths of the system consisting of a bi-disperse mixture of particles.

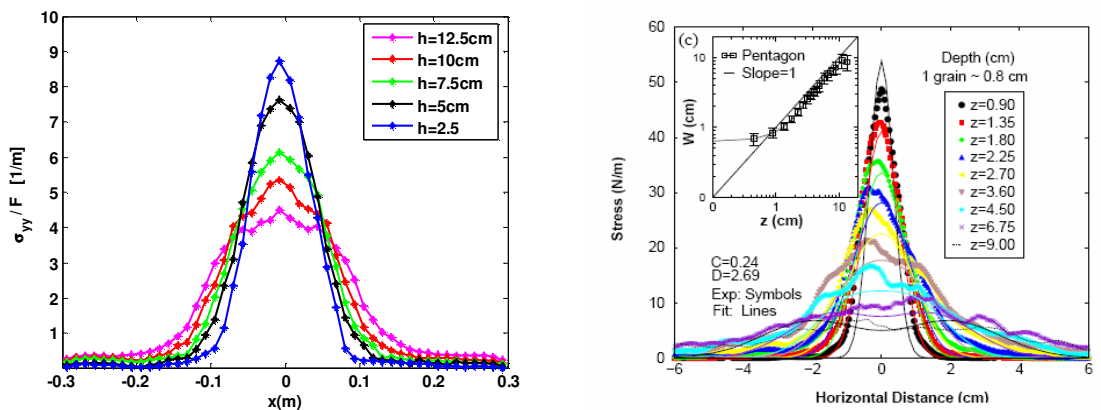


Figure 5.7: Vertical normal stress response at different depths of the system consisting of a mixture of pentagonal particles.

5.4 Stress response for different values of the friction coefficient

In this section, we are interested to determine the averaged vertical normal stress response of a rectangular system packed with mono-disperse particles for different values of coefficient of static friction. We prepare the sample by arranging soft particles of round shape in a layer wise manner, with particles sitting on a rectangular lattice, so that the particles in the same layer are not in contact, see figure 5.8. In this rectangular packing, each particle should have a fixed number of four contacts. Three different rectangular samples are created using the same material and the same simulation parameters except changing only the friction coefficients. Values used are $\mu = 0.3$, $\mu = 0.6$, and $\mu = 0.9$.

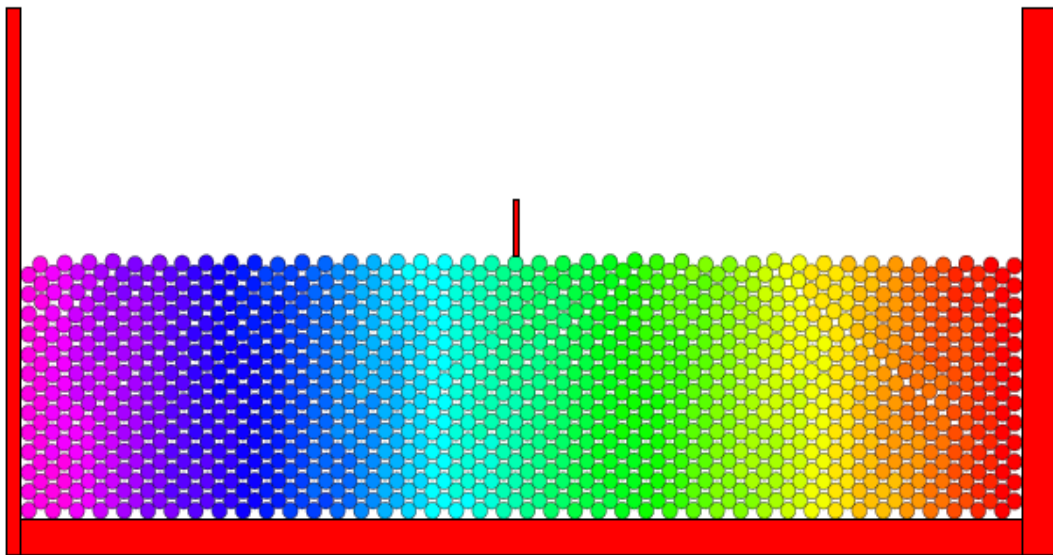


Figure 5.8: Snapshot of simulated rectangular packing from the mono-disperse set of soft particles, where particles are placed on a smooth support.

We then determine the polar diagram of the angular distribution of all contact forces for the rectangular layers packed with particles placed in a rectangular lattice. The results obtained from the simulation are displayed in Fig. 5.9. All angles are measured with respect to the horizontal axis. From the figure, it can be seen that the contact forces are mostly oriented along a few fixed directions given by the angles of 30° , 150° , 210° , and 330° , which is a trivial consequence of the high degree of order systems packed on a rectangular lattice.

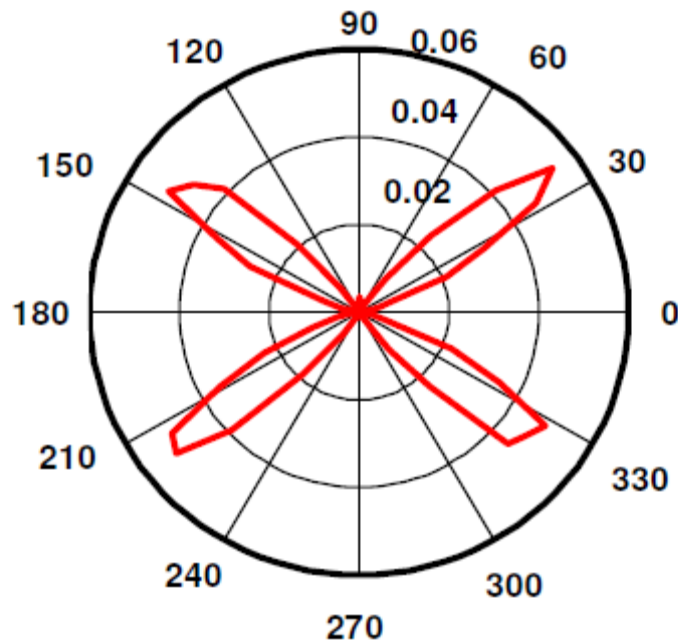
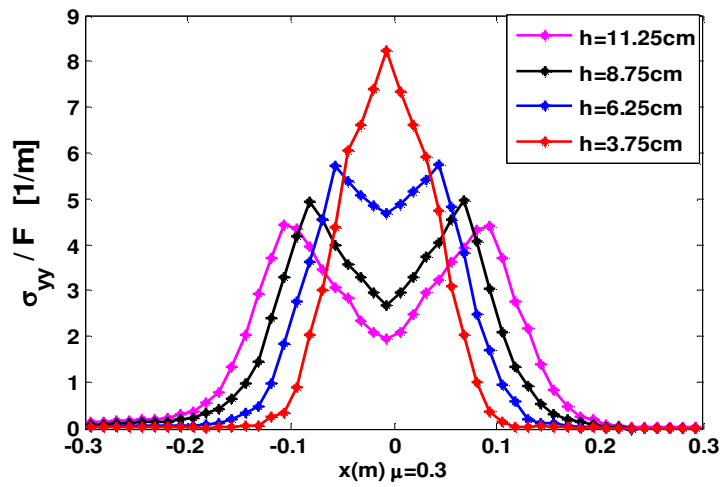


Figure: 5.9 Polar diagram of contact force angle distribution of a rectangular packing with the layer wise deposition of mono-disperse mixture of round particles.

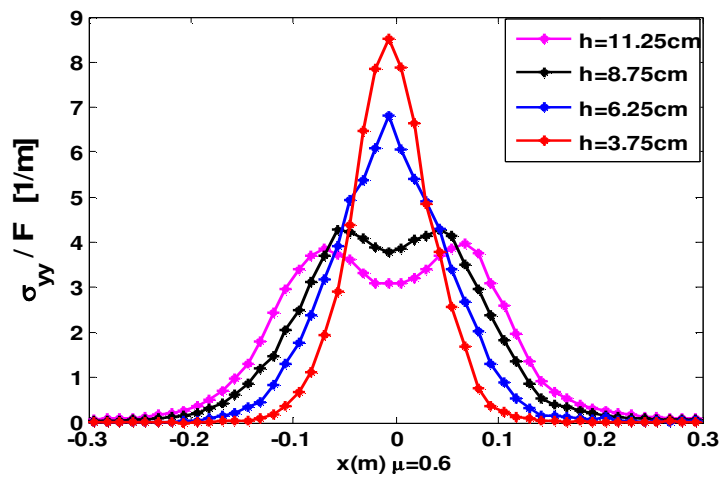
The simulation results for the stress response of a rectangular packing consisting of a mono-disperse arrangement of particles for different coefficients of friction μ is displayed in Fig. 5.10. For small values of friction coefficient, such as $\mu = 0.3$, the response consists of two peaks along the lattice direction as in Fig. 5.10. A, this double peaked shape appears not only at the greatest depth, but also exists up to the certain depth of the sample. Another interesting thing about this graph is that the stress response dip is very large in this case. However, for $\mu = 0.6$, the response consists of double peaked shape up-to certain height of the sample, as shown in Figure 5.10.B, but the response dip is very small compared to the earlier one and merges into a single peak below a given depth from the point of the application of the external overload. For $\mu = 0.9$, the response consists exclusively of a single central peak at each height of the sample as shown in Figure 5.10. C, whose width broadens linearly with depth.

In conclusion, the depth of the crossover between double and single peaked response decreases with increasing μ . That means when μ is very large, the response consists of an exclusively single peaked stress distribution but when μ is very small, there is sliding induced in the system, which increases the anisotropy of the system, this will lead to a transition to a double peaked stress response.

A



B



C

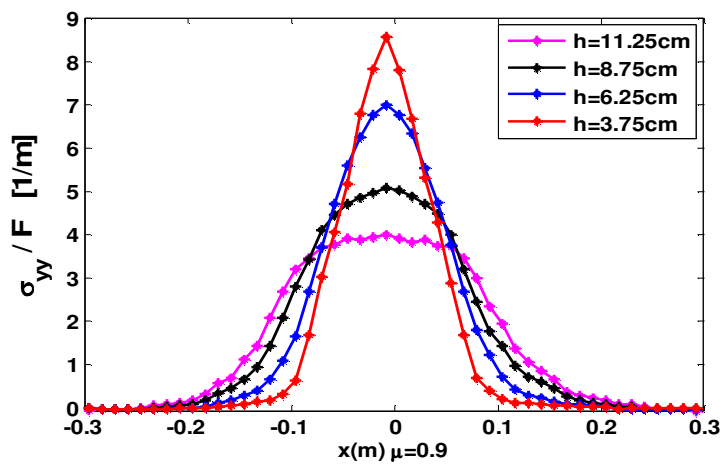


Figure 5.10: Simulation results of vertical normal stress response for different values of friction coefficients. **A**, for $\mu = 0.3$. **B**, for $\mu = 0.6$. **C**, for $\mu = 0.9$.

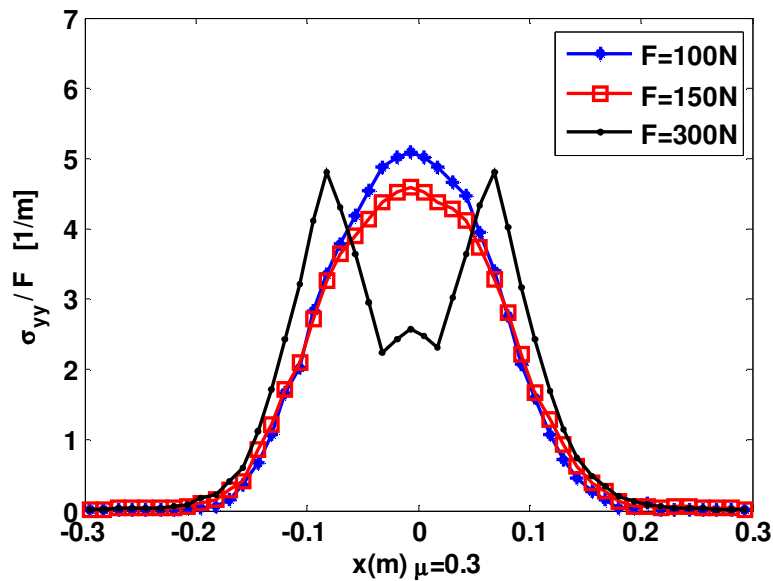


Figure 5.11: Vertical normal stress response for different values of applied overloads at bottom layer of the rectangular layers with static friction coefficient $\mu = 0.3$.

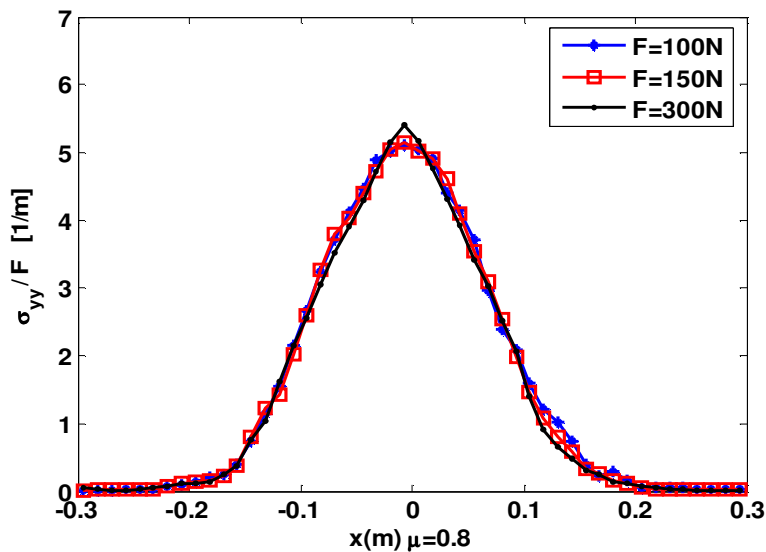


Figure 5.12: Vertical normal stress response for different values of applied overloads at bottom layer of the rectangular layers with static friction coefficient $\mu = 0.8$.

Furthermore, we determine vertical normal stress response for different values of a vertical applied force for the mono-disperse system, with the particle arranged on a hexagonal lattice with different coefficient of static friction. The simulation result is displayed in Fig. 5.11 for the system with static friction co-efficient $\mu = 0.3$ at the bottom layer for different amount of external overload. It can be seen in the figure, there is a

transition from a single peaked to a double peaked structure as the applied overload is increased. On the other hand, when μ is sufficiently large at $\mu = 0.8$, the stress response consists of a single peaked shape for the same amount of external overloading as is shown in figure 5.12. The results may indicate that, for small μ , elastic like stress response occurs for the small applied overload, whereas double peaked response functions are obtained for large applied overload. On the other hand, the response is absolutely proportional to the external force for large μ . One realises that the elasticity is enhanced by static friction coefficient.

5.5 Stress responses for poly-disperse packing

In this section, we focus on determining the stress response for a system containing a poly-disperse mixture of particles, then on simulation results of stress response to be compared with the existing experimental results [134]. For poly-disperse packing, we prepare samples with rough as well as smooth bottoms. In order to prepare a sample with smooth bottom, we used a flat bottom plate with friction on which the particles are dropped, whereas for a rough bottom the “plate” consists of a set of spatially fixed particles. The characteristics (surface asperities) of the ground plate with fixed particles is the same as for the simulated particle.

We find from Fig. 5.4 that the polygonal system shows a higher contact disorder than other packings of granular materials. Results on the vertical normal stress response at different heights of the system containing a poly-disperse mixture of particles with smooth bottom are shown in Fig. 5.13. As can be seen in the figure, the stress response consists of single peak at all height levels investigated. We did not observe two separated bumps as predicted by hyperbolic models in refs. [135-136]. So, it is to be recognised that, for large contact disorder of the packing the vertical normal stress consists of a single peak only, which means the stress response shows a behaviour like elastic like response, a behaviour typically describable with elliptic equations. Moreover, the width of the response increases linearly with the distance from the perturbing force.

We compare our simulation results qualitatively with existing experimental results shown in the right hand side of Fig. 5.13, obtained by G. Reydellet using “aquarium sand” and “Fontainebleau sand” and a poly-dispersity around 50%. Comparison shows that simulation results are in very good agreement with the experimental results.

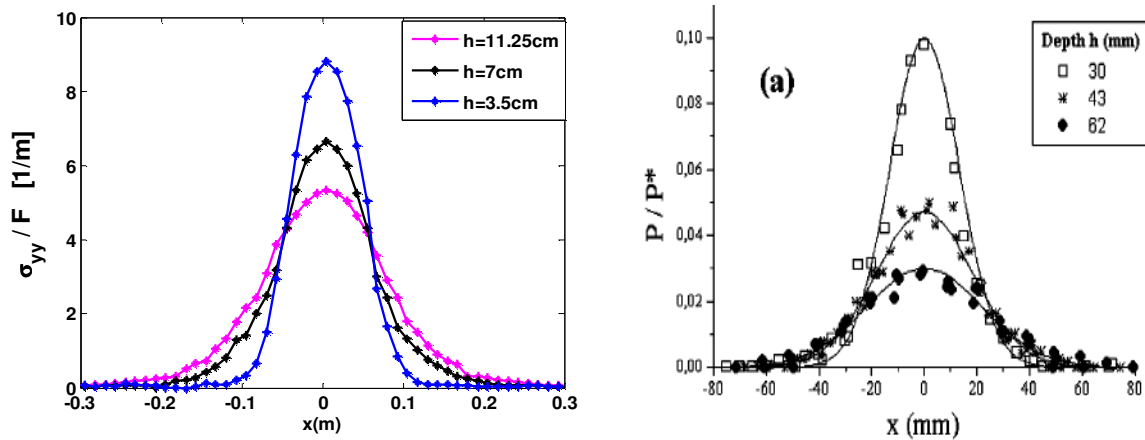


Figure 5.13: Vertical normal stress responses to a point source for a rectangular layer of granular material that contains a poly-disperse mixture of particles. The left side of the figure shows simulation results, where as the right side shows experimental results.

In the next step, we compare the vertical normal stress between the rough and the smooth bottom cases with the same materials. The stress response for the system containing a poly-disperse mixture of particles with rough bottom obtained from the simulation is represented in Fig. 5.14. In this case, the stress response consists of single peak behaviour. We notice that the behaviour of vertical normal stress response does not show much difference between the two systems. The magnitude of the vertical normal stress response is around 7% smaller than the stress response for smooth bottom.

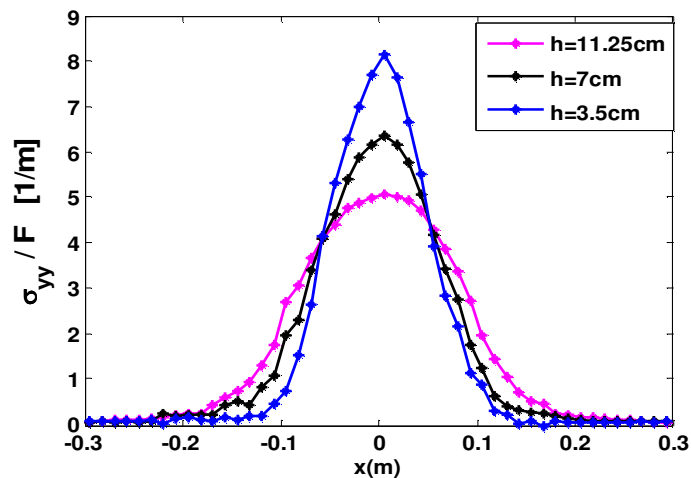


Figure 5.14: Vertical normal stress responses to a point source for a rectangular layer of granular materials with rough bottom that contains poly-disperse mixture of particles.

5.6 Comparison between numerical stress responses and an analytic solution

In the next step, we compare the stress responses from the numeric with an analytic solution in the framework of linear elasticity for a semi-infinite 2D medium (a half plane, $y > 0$). According to Boussinesq and Cerruti [141], an analytic expression for the stress tensor components with a force F applied at a point ($x=0$) on the edge ($y=0$) of the half plane reads:

$$\sigma_{yy} = \frac{2Fy^3}{\pi(x^2 + y^2)^2}, \quad (5.2)$$

$$\sigma_{xx} = \frac{2Fyx^2}{\pi(x^2 + y^2)^2}, \quad (5.3)$$

$$\sigma_{xy} = \frac{2Fy^2x}{\pi(x^2 + y^2)^2}. \quad (5.4)$$

We represent a comparison of the results of the vertical normal stress response of a semi-infinite system at a distance corresponding to that of the bottom layer of our finite system with the responses from the numerics for the rectangular system of a poly-disperse mixture of particles with either a rough or a smooth bottom in Fig. 5.15. The height of the rectangular system is 15 cm. We have taken the averages over twelve realizations.

In figure 5.15, the solid black curve shows the analytic result, whereas the red and blue curves represent the simulation results for a rough bottom and a smooth bottom, respectively. The figure demonstrates that the vertical normal stress responses for the three cases are qualitatively similar. In addition, there is no double peak shape appears underneath the point where the external force is applied. The experimental results of ref. [132] obtained using poly-disperse mixture of 'Fontainebleau' sand grains are represented in Fig. 5.16. It can be seen that our numerical results agree well with the experiments.

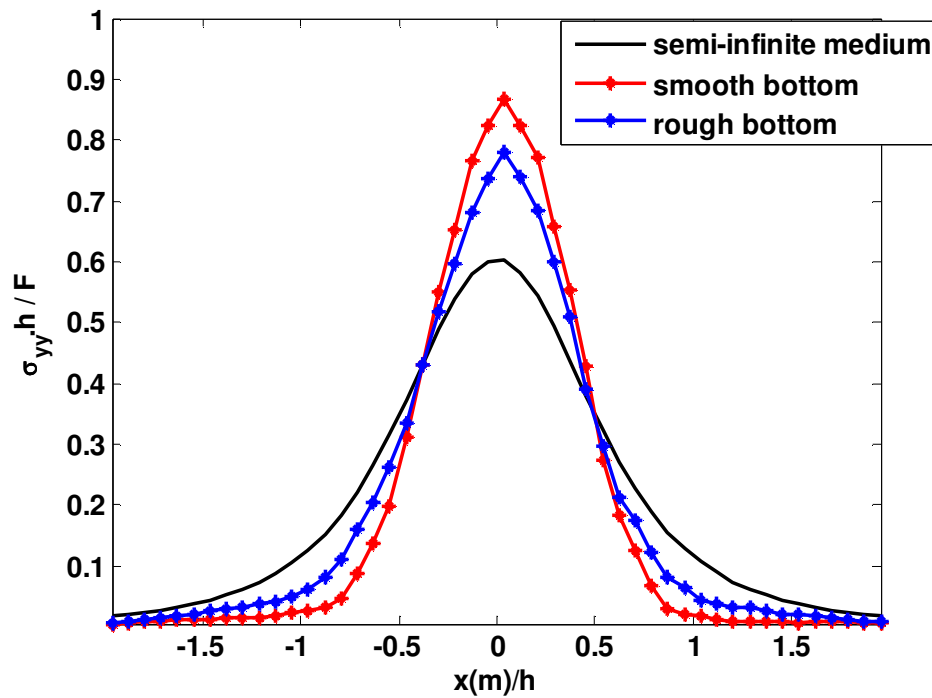


Figure 5.15: Simulation results of horizontal normal stress response of rectangular layer at the bottom layer for two different systems, compared with an analytic solutions.

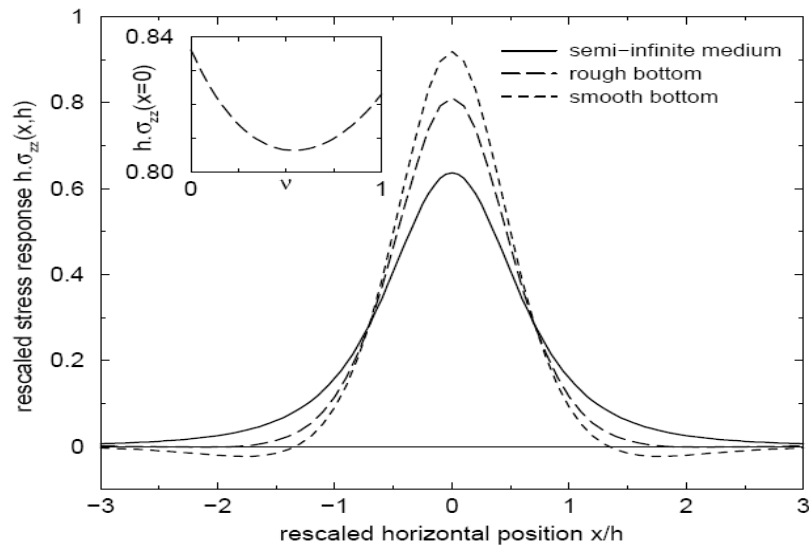


Figure 5.16: Experimental results of vertical normal stress response of rectangular layer at the bottom layer for three different systems.

5.7 Strain response for mono-disperse packing

We used a differentiation method, as explained in Chapter two, to determine the vertical normal strain tensor for the rectangular layers consisting of a mono-disperse arrangement of particles, where the particles have been placed on a hexagonal lattice on a rough bottom. The vertical strain tensor is averaged over many systems in order to avoid the fluctuations of the single system.

In Fig. 5.17, we plot the vertical normal strain responses at different depths of the packing that contains a mono-disperse mixture of particles. The strain response has the form of a bell-shaped curve with a single peak and the width of the response increases with the distance from the perturbation point.

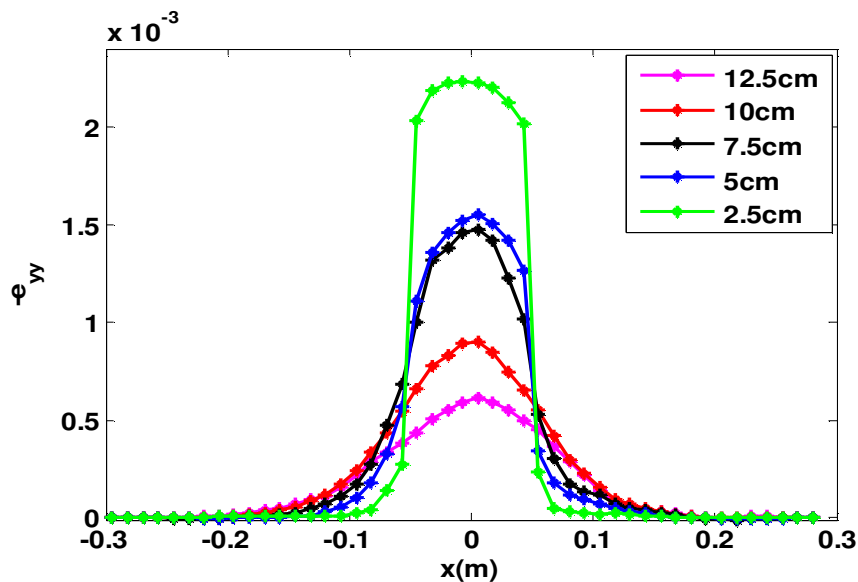


Figure 5.17: Vertical normal strain response for the packing that contains mono-disperse mixture of particles.

5.8 Conclusions

To conclude, we have determined the stress response of 2D granular packings to local force perturbations. We observe that for packings with strong spatial order, the average stress response shows a behaviour corresponding to that of hyperbolic continuum equations like those of the OSL model. As the amount of contact disorder increases, there is no wave-like stress propagation any more, and behaviour emerges that would rather be predicted by elliptic equations. Comparison with the experiments performed in ref. [131]

shows that the vertical normal stress responses for different packings are qualitatively similar to experimental ones.

We observe that both the static friction coefficient and the external overload affect the stress response of rectangular layers of granular materials. In addition, the vertical normal stress response definitively reveals elastic like stress response for system packed with poly-disperse mixture of particles with a rough and a smooth bottom, and agree well qualitatively between two systems.

We compared the analytic vertical and horizontal normal stress solution of an isotropic linearly elastic semi-infinite medium in 2D with our numerical stress responses for both smooth and rough bottoms. We observe that the vertical stress response is qualitatively similar for the three different systems. Comparison with the available experimental results from ref. [132] shows good agreement. We have determined the vertical normal strain response for the mono-disperse packing and find it to display a peak structure different from that of the stress response.

6

Conclusions & outlook

The main aim of this study was to try and contribute to the understanding of mechanical properties of non-cohesive granular materials, especially in the static limit. To achieve this goal we used a discrete element method (DEM), which is essentially a molecular dynamics (MD) approach, to simulate the dynamics of granulates made up from differently shaped particles. Numerical simulations were performed on two-dimensional systems, in which a sand pile was constructed from several thousands of convex polygonal particles with varying shapes, sizes and edge numbers. The particles were poured either from a point source or a line source. Static and dynamic frictions are accounted for in our force law, which enables us to simulate the relaxation of sand piles to their final static state.

As a first step of this work, several microscopic quantities including forces, contact points, contact displacement, and displacement of the particle centres of sand pile were evaluated, with the aim to determine from them averaged macroscopic variables, viz. stress, strain, inertia, density and fabric. To obtain macroscopic quantities from microscopic ones averaging was performed on ‘representative volume elements’ (RVE) in computing the macroscopic variables for a continuum description. A sufficient size for an RVE to yield converged results was determined to contain 100-200 particles,

From our DEM numerical experiment for the model of heaps of granular assemblies we point out here in the following some important conclusions:

We find that force networks exist and strongly fluctuate within the sand pile and that the shape distribution of the particles influences the structure of the force chains. We confirm that the probability distribution of normalized vertical forces exhibits exponential behaviour for (normalized force) $n > 1$. Our numerical results indicate that the probability distribution decays exponentially as has been found previously in the q-model.

Then in the next step, the pressure distribution was evaluated throughout the symmetric sand pile created by pouring materials from a point source or a line source, respectively. For a sand pile constructed from a point source, we find, not unexpectedly, that the pressure is not only minimum at the bottom layer, but also in higher layers of the pile. However, it disappears in layers near the tip of the sand pile.

A similar pressure minimum was not obtained in piles poured from a line source, which demonstrates that the simulation reproduces pressure distributions corresponding to different experimental protocols. Dynamically, the two cases differ by the appearance of avalanches during the build-up of a pile from a point source, and their absence for layer-by-layer deposition. We observed that two sand piles consisting of the same material may have different stress distributions, hence the construction method of an assembly of grains may affect the pressure distribution under it. Comparisons made with the available experimental results obtained by L. Vanel et al. [10], show that our numerical simulation results are qualitatively similar.

The density profile of sand piles was also measured for both types of sand piles. We observe that the middle region of the sand piles constructed from a point source displays higher density than the rest. On the other hand, we did not find much deviation in the density profile for the line source sand pile, density is approximately homogeneously distributed in the central region of the pile.

Moreover, the averaged stress tensors were compared numerically for sand piles consisting of a mixture of roundish particles with sand piles consisting of elliptical particles. We obtained a small dip below the apex of piles that contain a mixture of roundish particles when the pile was constructed by dropping particles from a point source, whereas the stress dip is clearly much larger for the case of elliptic particles. Comparing the magnitude of the stress dip at the bottom layer of the piles, we note that the amplitude of the stress dip is two times larger for the elliptic particles. Therefore, not only the construction history of the sand pile affects the pressure distribution under a sand pile, but also the shape of the particles. Our simulation results are in very good agreement with the recent available experimental sand pile results obtained by I. Zuriguel, T. Mullin & J. M. Rotter [11] both with spherical and non-spherical particles.

A numerical calculation of the strain distribution inside a sand pile interesting, because it is difficult or impossible to determine this quantity in experiments. Knowing this distribution will lead to a better understanding of the processes happening inside a granular assembly. In particular, we showed that it is possible to obtain not only stresses but also incremental displacements in the heap, by judicious use of an adiabatic

relaxation experiment, in which gravity is slowly changed. Hence the full set of variables of the linearized theory of elasticity is available.

To obtain a measure for strain, the sand pile was allowed to relax under reduction of gravity. We define strain with respect to a hypothetical reference state of a pile at zero gravity. This reference state may be approximated using a static pile obtained in a simulation, by slowly changing gravity and following the particle trajectories during the ensuing load change and then extrapolating to zero gravity, as has been discussed in Section 2.6.2. This procedure gives a decent approximation for the vertical strain u_{yy} , but is only qualitative for u_{xx} and u_{xy} . Incremental strains can be measured precisely, because they do not require the definition of a particular reference state. Then it is easy to compute the macroscopic strain tensor by averaging over an RVE. It turns out that the size of the RVE we need for converged strain tensors is the same as for stress tensors.

The averaged strain tensor was evaluated throughout the sand pile, for two types of sand piles that were constructed using two different pouring protocols. We find that the vertical normal strain u_{yy} is not only minimum at the bottom layer, but also in higher layers of the sand piles constructed from a point source. However, the minimum disappears in layers near the tip of the pile. A similar vertical normal strain minimum was not obtained in piles poured from a line source, which demonstrates that the construction history affects the strain distribution under a sand pile.

Additionally, we determined numerically the fabric tensor in order to describe the internal texture of granular assemblies. This will lead to a measure of the degree of the internal anisotropy of the assemblies of grains and provides as with the number density of the particle contacts within the granular system. The fabric tensor was obtained using normalized branch vectors at the contact points of the particle. The trace of the averaged fabric tensor was measured throughout the sand pile, with the result that the number of contacts of the particles increases towards the centre and decreases towards the free surface of the sand pile. Since the density is maximum in the centre for the sand pile constructed from a point source, this means that the number of contacts is higher where the density is maximum, as expected. We observe that the deviatoric fraction of the fabric tensor decreases towards the centre, which means the fabric is more isotropic near the centre of the sand pile and more anisotropic in the outer part.

As an interesting quantity not usually considered in the literature, we determined the elastic constants assuming Hooke's law throughout a sand pile. We then established the correlation between the elastic material constants and the fabric tensor. Elastic constants were determined by using incremental stresses and incremental strains. We found that the elastic constants changed with the relative heights inside the sand pile. In particular, Young's modulus of elasticity, the shear modulus and the bulk modulus increases towards the centre and towards the bottom layer of the sand pile and decreases towards the surface of the pile. The simulated sand pile is softer by about around one order of magnitude than its individual particles indicating that it is meaningful to assign elastic properties to the macroscopic assembly. The bulk modulus is observed to increase

towards the centre, meaning that the central core region of the heap is harder than its surroundings. In addition, we observed that the bulk modulus of the sand pile, i.e. the stiffness of granulate is a linear function of the trace of the fabric.

The stress distribution was measured numerically inside asymmetric sand piles as well that were constructed either from a line source or from a point source procedure. We compared the simulation results with those of available analytical predictions for the stress solution at the bottom of the pile. This comparison shows that the behaviour of stress distributions are qualitatively very similar, giving credence to that analytical work [obtained by Cantelaube et al. [2]].

Another correlation that we measured was the relationship between invariants of the incremental stress tensor and the incremental strain tensor, the observed stress and strain relation behaviour was globally nonlinear due to the position dependence of elastic moduli. While we have linear elastic behavior near the centre of the pile, there is nonlinear behavior announcing the transition to plastic behavior near the surface of the sand piles.

An essential observation is that the macroscopic tensors stress, strain and fabric are not collinear in the granular heap, i.e. their orientations are different. The orientation of the fabric is tilted most, that of the strain tensor is tilted least and thus, simply speaking the material can not be described by a simple elastic model involving only two elastic constants. However, in the case where there is a strong deviation between the local orientation of the fabric and stress tensors, the fabric tensor has almost equal eigen values, rendering a precise determination of its principal axes difficult. Hence, more work needs to be done to determine whether this deviation is significant. In the case of elliptic particles, all three tensors seem to be well aligned with each other.

To optimize our strain calculations, the strain tensor was evaluated by adopting three different types of best-fit methods including Cambou et al. [115], Liao et al. [116], and Cundall et al. [76], and also by simple differentiation of the displacement particle centres. Simulations showed that the strains obtained by Cambou et al., Cundall et al. and the differentiation method give similar results, whereas the strain obtained using Liao et al. exhibits different behaviour. The closeness of the results from three out of the four methods in the centre of a pile suggests consistency of these strain calculations. As discussed in the main text one of the two best-fit methods gives best results, and we decided to employ the Cambou approach in our strain calculations.

Comparison with simple analytic theories [1-2] for the macroscopic mechanical behaviour of a sand pile shows that these theories have certain deficiencies. Radical departures from conventional approaches such as the introduction of almost ad hoc closure relations [1] seem unnecessary, as an equally good or better fit of the data is obtained by a simple elasto-plastic model [2]. Nevertheless, reality is not as simple as these models. One ingredient missing in all the models that use stresses only are density variations in the sand pile, another that might be important as well the fabric tensor. Note however that the Cantelaube model [2] is spectacularly good for sand piles constructed

layer-wise. In these, density variations are absent and the fabric does not seem to play a major role.

Our final investigation concerns the mechanical properties of rectangular layers of assemblies of grains in the static limit. The averaged stress and strain response functions to a point force, determined in this part of the work allow inferences to be drawn on the nature of the continuum equations governing macroscopic behaviour. So they give indirect support to one of the simple models discussed above or the others. This study has been done by use of a DEM numerical simulation generating granular packings with different packing order. To construct packings of varying degrees of spatial order, we simulated three different types of samples by employing mono-disperse and bi-disperse mixtures of particles as well as mixture of pentagonal particles. An external overload was applied to a single grain at the top surface of the rectangular system with a small vertical force.

We then measured the orientation of the contact forces for the different packings. It is observed that, the mono-disperse packing is highly ordered, whereas the contact disorder of the remaining packings is increasing from the bi-disperse packing to the pentagonal packing. Measuring the average vertical normal stress response at different heights of the sample we find that the shape of the vertical normal stress response function depends upon the packing order of the granular aggregate. For packings with strong spatial order, the average stress response shows a behaviour corresponding to that of hyperbolic continuum equations like those of the OSL model. As the amount of contact disorder increases, there is no wave like stress propagation any more and a behaviour emerges that would rather be predicted by elliptic equations. Comparison with the experiments performed in ref. [131] using photo elastic material shows that the vertical normal stress responses for different packings are qualitatively similar to experimental ones, which is another confirmation of consistency of our approach.

Moreover, we compared the analytic vertical normal stress solution of an isotropic linearly elastic semi-infinite medium in 2D with our numerical stress responses for both smooth and rough bottoms. We observe that the vertical stress response is qualitatively similar for two different systems and the analytic solution.

The coefficient of static friction and the external overload play an important role on the stress response of rectangular layers of granular assemblies. When the external overload is increased, the vertical normal stress response becomes flatter and progressively two peaks appear. For small overloads, the response exclusively consists of a single peak, and its shape is essentially independent of the overload. When static friction is sufficiently large, the response is always single peaked. This turns out to be yet another consequence of friction as when static friction is small, sliding occurs in the system and leads to a crossover to a two peaked response.

In addition, we evaluated the averaged strain response of rectangular layers that consisted of mono-disperse mixtures of round particles to a local force perturbation, with particles placed on a hexagonal lattice. The vertical normal strain was determined at different

heights of the system. We find the strain response to consist of exclusively single peaked underneath the point where the external force is applied. The vertical normal strain response has the form of a bell-shaped curve with a single peak and the width of the response increases with the distance from the perturbation point for mono-disperse packing displays a peak structure different from that of the stress response. This result demonstrates failure of isotropic elasticity in that rather singular, because ordered system.

Outlook

Despite the fact that we have determined individual microscopic and averaged macroscopic quantities inside a sand pile and made comparison with existing experimental results and analytical theories, there are still many open questions.

Simulation results of stress and strain tensor may serve for a determination of nonlinear stress-strain relationships for sand piles. Moreover, the constitutive relations proposed for the sand pile model so far are in terms of the stress tensor only and it would be interesting to develop better constitutive relations using not only the stress strain tensor, but also the density and or the fabric tensor to get a set of fully working continuum equations.

Furthermore, comparison has been made between simulation and analytical theories for the stress distributions under a symmetric sand pile. We hope that our simulation results for the stress distribution of an asymmetric sand pile will stimulate both creation of theories and comparison with the few existing analytical predictions for asymmetric sand piles.

References

- [1] Wittmer, J. P., Cates, M. E., Claudin, P.: Stress propagation and arching in static sand piles. *J. Phys. I France* **7**, 39 -80, 1997.
- [2] Didwania, A. K., Cantelaube, F., Goddard, J. D.: Static multiplicity of stress states in granular heaps. *Proc. R. Soc. Lond. A* **456**, 2569-2588, 2000.
- [3] Lade, P. V., Prabucki, M.-J.: Softening and preshearing effects in sand. *Soils and Found., Jap. Geotechn. Soc.* **35**, 93-104, 1995.
- [4] Gudehus, G.: A comprehensive constitutive equation for granular materials. *Soils and Found., Jap. Geotech. Soc.* **36**, 1-12, 1996.
- [5] Eggers, J., Riecke, H.: Continuum description of vibrated sand. *Phys. Rev. E*, **59**, 4476-4483, 1999.
- [6] Csahok, Z., Misbah, C., Rioual, F., Valance, A.: Dynamics of aeolian sand ripples. *Eur. Phys. J. E* **3**, 71-86, 2000.
- [7] J. Smid, P.V. Xuan, and J. Thyn: Effect of filling method on the packing distribution of a catalyst bed: *Chem. Eng. Technol.* **16**, 114, 1993.
- [8] D. Picard, L.P. Terzulli, C. Lesaffre, V. Mineau: Packing density of a poly-dispersed granular material. *Powder and grains*, Kishino(ed.), Swets and Zeitlinger, Lisse, ISBN 90 2656 826 9, 15-16, 2001.
- [9] H.A. Janseen: Versuche über Getreidedruck in Silozellen. *Zeitschr. d. Vereines deutscher Ingenieure*, **39**, 1045-1049, 1895.
- [10] Vanel, L., Howell, D., Clark, D., Behringer, R.P., Clement, E.: Memories in sand: Experimental tests of construction history on stress distributions under sand piles, *Phys. Rev. E*, **60**, R5040, 1999.
- [11] I. Zuriguel, T. Mullin, and J.M. Rotter: Effect of particle shape on the stress dip under a sand pile, *Physical Review Letters* **98**, 028001, 2007.
- [12] R. Brockbank, J.M. Huntely, and R. Ball: Contact force distribution beneath a three-dimensional granular pile. *J. Phys. II (France)* **7**, 1521-1532, 1997.

- [13] Wittmer, J. P., Cates, M. E., Claudin, P. and J.-P. Bouchaud: An explanation for the stress minimum in sand piles. *Nature*, 382, 336-338, 1996.
- [14] Smid, J. and Novosad, J.: Pressure distribution under heaped bulk solids. *Proc. Powtech, Conf., Ind. Chem. Eng. Symposium Series*, 63, D3/V/1-12, 1981.
- [15] Cantelaube, F. & Goddard, J. D.: Elastoplastic arching in 2D granular heaps. *Powders and Grains, Proc. third int. Conf. Durham, NC, USA, 18-23 May 1997*, R. P. Behringer and J. T. Jenkins(eds.), pp. 231-234. Rotterdam: Balkema.
- [16] Zuriguel, I. and Mullin, T.: The role of particle shape on the stress distribution in a sand pile. *Proc. R. Soc. A*, 464, 99-116, 2008.
- [17] T. Jotaki and R. Moriyama. On the bottom pressure distribution of the bulk materials piled with the angle of repose *Journal of the society of powder Technology, Japan*16 (4): pp. 184-191, 1979.
- [18] Matuttis, H. G.: Simulation of the pressure distribution under a two dimensional heap of Polygonal particles. *Granular Matter* 1, 83-91, 1998.
- [19] Matuttis, H. G., Luding, S., and Herrmann, H. J.: Discrete element simulations of dense packings and heaps made of spherical and non-spherical particles. *Powder Technol.* 109, 208-292, 2000.
- [20] Luding, S.: Stress distribution in static two-dimensional granular model media in the absence of friction. *Phys. Rev. E*, 55, 4720-4729, 1997.
- [21] Liffman, K., Chan, D. Y. C. & Hughes, B. D.: On the stress depressions under a sand pile. *Powder Technol.* 78, 263-271, 1994.
- [22] Liffman, K., Nguyen, M., Metcalfe, G., & Cleary, P.: Forces in piles of granular material: an analytic and 3D DEM study, *Granular Matter* 3, 165-176, 2001.
- [23] Liffman, K., Nguyen, M., & Cleary, P.: Stresses in sand piles: Second Int. Conference on CFD in the minerals and process industries, CSIRO, Melbourne, Australia, 1999.
- [24] Li, Y. J., Xu, Y. & Thornton, C.: A comparison of discrete element simulations and experiments for 'sand piles' composed of spherical particles. *Powder Technol.* 160, 219-228, 2005.
- [25] Zhao, Y. C., Xu, B. H., Zou, R. P., Yu, A. B., and Zulli, P.: Stress distribution in a sand pile formed on a deflected base. *Advanced powder Technol.*, Vol.14, No.4, pp. 401-410, 2003.

- [26] Hemmingsoon, J., Herrmann, H. J. & Roux, S.: Vectorial cellular automaton for the stress in granular media. *J. Phys. I France* 7, 291-302.
- [27] Liu, C.-h., Nagel, S. R., Schecter, D. A., Coppersmith, S. N., Majumdar, S., Narayan, O. & Witten, T.: Force fluctuations in beads packs. *Science* 269, 513-515, 1995.
- [28] Coppersmith, S. N., Liu, C.-h., Majumdar, S., Narayan, O. & Witten, T. A.: Model for force Fluctuations in bead packs. *Phys. Rev. E*, 53, 4673-4685, 1996.
- [29] Nguyen, M. L., and Coppersmith, S. N.: Properties of layer-by-layer vector stochastic models of force fluctuations in granular materials. *Phys. Rev. E*, 59, 5870, 1996.
- [30] J. E. S. Socolar: Average stresses and force fluctuations in noncohesive granular materials. *Phys. Rev. E* 57, 3204, 1998.
- [31] M.G. Sexton, J.E.S. Socolar, and D. G. Schaeffer: Force distribution in a scalar model for non-cohesive granular material. *Phys. Rev. E* 60, 2, 1999.
- [32] F. Radjai, M. Jean, J. J. Moreau, and S. Roux: Force distributions in dense two-dimensional granular systems. *Phys. Rev. Lett.* 77, 2, pp. 274-277, 1996.
- [33] F. Radjai, D. E. Wolf, M. Jean, and J. J. Moreau: Bimodal character of stress transmission in granular packings. *Phys. Rev. Lett.* 80, 1, pp. 61-64, 1998.
- [34] C. Thornton and S. J. Antony: Quasi-static deformation of particulate media. *Philos. Trans. Royal Society London, Ser. A* **356**, 2763-2782, 1998.
- [35] D. M. Mueth, H. M. Jaeger, and S. R. Nagel: Force distribution in a granular medium. *Phys. Rev. E* 57, 3164, 1998.
- [36] Narayan, O.: Vector lattice model for stresses in granular materials. Arxiv: Cond-Mat/0004399V1, 2000.
- [37] Moukarzel, C. F.: Isostatic phase transition and instability in stiff granular materials. *Phys. Rev. Lett.* **81**, 1634-1637, 1998.
- [38] Roux, J. N.: Geometric origin of mechanical properties of granular materials. *Phys. Rev. E* 61, 6802-6836, 2000.
- [39] Unger, T.: Characterization of static and dynamic structures in granular materials. PhD thesis, Budapest University, 2004.

- [40] A. S. J. Suiker, R. de Borst and C. S. Chang, Micro-mechanically based higher-order continuum models for granular materials. In: D. Kolymbas (eds.), *Constitutive modelling of granular materials*. Berlin: Springer, pp. 249-274, 2000.
- [41] A. S. J. Suiker, R. de Borst and C. S. Chang: Micro-mechanical modelling of granular material. Part 1: Derivation of a second-gradient micro-polar constitutive theory. *Acta Mech.* 149, 161-180, 2001.
- [42] A. S. J. Suiker, R. de Borst and C. S. Chang: Micro-mechanical modelling of granular material. Part 2: Plane wave propagation in finite media. *Acta Mech.* 149, 181-200, 2001.
- [43] R. J. Bathurst and L. Rothenberg: Micromechanical aspects of isotropic granular assemblies with linear contact interactions. *J. Appl. Mech.* 55, 17-23, 1988.
- [44] C. S. Chang, Micromechanical modelling of constitutive relations for granular material. In: M. Satake and J. T. Jenkins (eds.), *Micromechanics Granular Materials*. Amsterdam: Elsevier Science Publishers B. V. pp. 271-279, 1988.
- [45] J. T. Jenkins, Volume change in small strain axisymmetric deformations of a granular material. In: M. Satake and J. T. Jenkins (eds.), *Micromechanics of Granular Materials*. Amsterdam: Elsevier Science Publishers B.V., pp. 245- 252, 1988.
- [46] E. Pasternak and H. B. Mühlhaus: Cosserat continuum modelling of granulates materials. In: S. Valliappan and N. Khalili (eds.), *Computational Mechanics – New Frontiers for New Millennium*. Amsterdam: Elsevier Science, pp. 1189-1194, 2001.
- [47] E. Pasternak and H.-B. Mühlhaus, Large deformation Cosserat continuum modeling of granulate materials. In: L. Zhang, L. Tong and J. Gal (eds.), *Applied Mechanics. Progress and Application. ACAM 2002. The Third Australasian Congress on Applied Mechanics New Jersey, London, Singapore: World Scientific*, pp. 389-396, 2002.
- [48] Abu-Zaid S., G. Ahmadi: Analysis of rapid shear flows of granular materials by a kinetic model including frictional losses, *Powder Technology*, vol. 77, pp.7-17, 1993.
- [49] Johnson P. C., Jackson R., Frictional-collisional constitutive relations for granular materials, with application relations to plane shearing, *Journal of Fluid Mechanics*, vol.176, pp. 67-93, 1987.
- [50] Savage, S. B: Streaming motions in a bed of vibrationally fluidized dry granular material, *Journal of Fluid Mechanics*, vol. 194, pp. 457-478, 1988.

- [51] Barker G. C.: Computer simulations of granular materials, in *Granular Matter*, ed. By A. Mechta, Springer-Verlag, pp. 35-83.
- [52] E. B. Pitman and D. G. Schaeffer, *Comm. Pure Appl. Math.* 40, 421, 1987.
- [53] D. G. Schaeffer, *J. Differential Equations* 66, 19, 1987.
- [54] J. J. Moreau, in *Non-smooth mechanics and applications*, eds. J. J. Moreau and P. D. Panayiotopoulos, CSIM Courses and Lectures 302, Springer-Verlag, Wien, New York, pp. 1, 1988.
- [55] F. Radjai and L. Brendel: Non-smoothness, indeterminacy, and friction in two-dimensional arrays of rigid particles. *Physical review E*, 54(1), 861-873, 1996.
- [56] F. Radjai, M. Jean, J.-J. Moreau, and S. Roux. Force distribution in dense two-dimensional granular systems. *Physical Review Letters*, 77(2), 274-277, 1996.
- [57] T. Unger and J. Kertesz. The contact dynamics method for granular media. *AIP conference proceedings*, 661(1), 116-138, 2003.
- [58] J. J. Moreau, *Eur. J. Mech. A-Solids*, 13, 93-114, 1994.
- [59] Chopard, B., Droz, M.: *Cellular automata modeling of physical systems*. Cambridge University Press, 1998.
- [60] Zhao, J. G.: *Lattice Boltzman Methods*, Springer Verlag, 2004.
- [61] Frisch, U., Hasslacher, B., Pomeau, Y.: Lattice-gas automata for the Navier-stokes equation. *Phys. Rev. Lett.* 56, 1505-1508, 1986.
- [62] Caram, H., Hong, D. C.: Random-walk approach to granular flows. *Phys. Rev. Lett.* 67, 828- 831, 1991.
- [63] Fitt, A. D., Wilmort, P.: Cellular-automaton model for segregation of two-species granular flow. *Phys. Rev. A* 45 (4), 2383, 1992.
- [64] Hemmingson, J., Herrmann, H. J., Roux, S.: Vectorial cellular automaton for the stresses in granular media. *J. Physique* 1(7), 291-302, 1997.
- [65] Katsura, N., Shimosaka, A., Shirakawa, Y., Hidaka, J.: Simulation for flow behaviour of vibrating granular materials using cellular automata. *Powders and grains* (ed. Kishino), Swets and Zeitlinger, Lisse, pp. 525-528, 2001.
- [66] Goles, E., Gonzales, G., Herrmann, H., Martienez, S.: Simple lattice model with inertia for sand piles, *Granular Matter* 1, 137-140, 1998.

- [67] Murakami, A., Sakaguchi, H., Takasuka, T., Fuji, H.: Study of micro topology and its evolution in granular material using a cellular automata model. *Powders and Grains* (ed. Kishino), Swets and Zeitlinger, Lisse, pp. 33-36, 2001.
- [68] Baxter, G. W., Behringer, R. P., Fagert, T., Johnson, G. A.: Pattern formation and time dependence in flowing sand. In: Joseph, D.D., Schaeffer, D.G. (eds.), *Two phase flows and waves*. Springer Verlag, New York, pp. 1-29, 1990.
- [69] Baxter, G. W., Behringer, R. P.: Cellular automaton models for the flow of granular materials. *Physica D* 51, 465-471, 1991.
- [70] Deserable, D., Martienez, J.: Using a cellular automaton for the simulation of flow of granular materials. In: Thornton (ed.) *Powder and Grains* Balkema, 1993, pp. 345-350.
- [71] Peng, G., Herrmann, H. J.: Density waves of granular flow in a pipe using lattice gas automata. *Phys. Rev. E* 49, 1796-1799, 1994.
- [72] Kozicki, J., Tejchman, J.: Simulations of granular flows in silos with a cellular automata Model. *The international Journal of Storing, Handling and processing powder (Powder Handling and processing)*; 13 (3), 267-275, 2001.
- [73] Kozicki, J., Tejchman, J.: Application of a cellular automaton to simulations of granular flow in silos, *Granular Matter* 7, 45-54, 2005.
- [74] S. Vollmar and H. J. Herrmann, *Physica A* 215, 411, 1995.
- [75] J. J. Alonso and H. J. Herrmann, *Phys. Rev. Lett.* 76, 4911, 1996.
- [76] Cundall, P. A., Strack, O. D. L.: A discrete numerical model for granular assemblies. *Géotechnique* 29, 47 -65, 1979.
- [77] B. D. Lubachevsky, *J. Comput. Phys.* 94, 255, 1991.
- [78] S. McNamara and W. R. Young, *Phys. Fluids A* 4, 496, 1992.
- [79] S. McNamara and W. R. Young, *Phys. Fluids A* 5, 34, 1993.
- [80] B. Bernu and R. Mazighi, *J. Phys. A* 23, 5745, 1990.
- [81] E. Clement, S. Luding, A. Blumen, J. Rajchenbach, and J. Duran, *Int. J. Mod. Phys. B* 7, 1807, 1993.
- [82] S. Luding, E. Clement, A. Blumen, J. Rajchenbach, and J. Duran, *Phys. Rev. E* 49, 1634, 1994.

- [83] M. P. Allen and D. J. Tildesley: *Computer simulation of liquids*, Oxford University Press, Oxford, 1987.
- [84] Luding, S.: Collisions and contacts between two particles. In: Herrmann, H. J.; Hovi, J. P., Luding, S. (eds): *Dry granular media*, Dordrecht: Kluwer Academic Publishers, 1998.
- [85] Luding, S.: *Die Physik Kohäsionsloser granularer Medien*. Habilitationsschrift, Universität Stuttgart, (eingereicht) Juli 1997.
- [86] S. Luding and S. McNamara: How to handle the inelastic collapse of a dissipative hard sphere gas with the TC model. *Granular Matter*, 1(3), 113-128, 1998.cond- mat/9810009.
- [87] S. McNamara and W. R. Young: Dynamics of a freely evolving, two-dimensional granular medium. *Phys. Rev. E*, 53(5), 5089-5100, 1996.
- [88] Campbell, C. S., Brennen, C. E.: Chute flows of granular materials: some Computer Simulations, *J Appl. Mech.*, 52, S. 172-178, 1985.
- [89] Campbell, C. S., Brennen, C. E.: Computer simulation of granular shear flows: *J Fluid Mech.*, 151, S. 167-188, 1985.
- [90] Campbell, C. S., Brennen, C. E.: Computer simulation of shear flows of granular material. In: Jenkins, J.; satake, M. (eds.): *Studies in Applied Mechanics 7, Mechanics of granular Material- New models and constitutive relations*, Amsterdam: Elsevier, S. 313-326, 1983.
- [91] Campbell, C. S.: Boundary interactions for two-dimensional granular flows: asymmetric stress couple stress. In: Jenkins, J.; satake, M. (eds): *Studies in Applied Mechanics 20, Micromechanics of granular Material*, Amsterdam: Elsevier, S.163-174, 1988.
- [92] Campbell, C. S.: Computer simulation of rapid granular flows. *Proc. of the 10th U. S. National Congress on Applied Mechanics*, S. 327-338, 1987.
- [93] Campbell, C. S. and Gong, A.: The stress tensor in a two-dimensional granular shear flows. *J Fluid Mech.*, 164, S. 107-125, 1986.
- [94] M. D. Shattuck, C. Bizon, P. B. Umbanhowar, J. B. Swift, and H. L. Swinney. Pattern formation in vertically vibrated granular layers: Experiments and simulation. In H.J. Herrmann, J.-P. Hovi, and S. Luding editors, *Physics of dry granular media*, volume 350 of Series E: *Applied Sciences*, pages 613-618. Nato ASI, Kluwer Academic Publishers, September 1997.

- [95] Simulation of two-dimensional arrays of beads under external vibrations: Scaling behaviour, *Physical Review E*, Volume 50, Number 4, 1994.
- [96] Taguchi Y-H.: New origin of a convective motion: Elastically induced convection in granular materials, *Physical Review Letters*, vol. 69, No. 9, pp. 1367-1370.
- [97] Verlet, L.: Computer experiments on classical fluids. I. Thermo dynamical properties of Lennard-Jones molecules. *Phys. Rev.* 159, 98-103, 1967.
- [98] Swope, W. C., Andersen, H.C., Berens, P. H., and Wilson, K. R.: A computer simulation method for the calculation of equilibrium constants for the formation of physical cluster of molecules: application to small water clusters. *J. Chem. Phys.* 76, 637-649, 1982.
- [99] Aoki K. M., T. Akiyama: Simulation studies of pressure and density wave propagations in vertically vibrated beds of granules, *Physical Review E*, Vol.52, No.3, pp. 111-121.
- [100] Gear, C. W.: *Numerical Initial Value Problems in Ordinary Differential Equations*. Prentice Hall, 1971.
- [101] H. G. Matuttis, S. Luding, and H. J. Herrmann. Discrete element simulation of dense packings and heap made of spherical and non-spherical particles. *Powder Technology*, 109, 278-292, 2000.
- [102] Lee J., H. J. Herrmann. Angle of repose and angle of marginal stability: molecular dynamics of granular particles. *J. Phys. A*, Vol.26, pp. 373-383.
- [103] Schinner, A.: *Ein Simulationssystem für granulare Aufschüttungen aus Teilchen variabler form*. PhD thesis, Univ. Magdeburg, 2001.
- [104] Schäfer. J., S. Dippel and D. E. Wolf: Force schemes in simulations of granular materials. *J. Physique I* 6, 5-20, 1996.
- [105] H. Hertz. Über die Berührung fester elastischer Körper. *J. für die reine u. angew. Math.*, 92:136, 1882.
- [106] M. Coulomb, *Theories des Machines Simples*. *Academies des Sciences*, 10:166, 1781.
- [107] Alexander V. Potapov and Charles S. Campbell: A fast model for the simulation of non-round particles. *Granular Matter* 1, 9-14, 1998.
- [108] Alexander Schinner: Fast algorithms for the simulation of polygonal particles. *Granular matter* 2, 35-43, 1999.

- [109] Cundall, P. A.; Strack, O. D. L.: Modeling of microscopic mechanisms in granular material. In: Jenkins, J.; Satake, M. (eds.): Studies in Applied mechanics 7, Mechanics of granular Materials- New Models and Constitutive relations, Elsevier, 1983, S. 137-151.
- [110] Kruyt, N. P. and L. Rothenburg: Micromechanical definition of the strain tensor for granular materials. ASME journal of Applied Mechanics 118, 706-711, 1996.
- [111] Katalin Bagi: Stress and strain in granular assemblies, Mechanics of Materials, 22, pp. 165-177, 1996.
- [112] Christoffersen, J., Mehrabadi, M. M., Nemat-Nasser, S.: A micromechanical description of granular material behaviour. Journal of Applied Mechanics, 48, 339, 1981.
- [113] Lätzel, M., Stefan Luding, Herrmann, H. J.: Macroscopic material properties from quasi-static, microscopic simulations of a two-dimensional shear-cell. Granular Matter 2, 123-135. Cond-mat/0003180.
- [114] M. Satake. Three-dimensional discrete mechanics of granular materials. In N. A. Fleck and A. C. E. Cocks, editors, IUTAM symposium on mechanics of granular and porous materials, Pages 193-202, Kluwer Academic Publishers, 1997.
- [115] Cambou, B., Chaze, M., Dedecker, F.: Change of scale in granular materials. Eur. J. Mech. A/Solids 19, 999-1014, 2000.
- [116] Liao, C. L., Chang, T. P., Young, D. H., Chang, C. S.: Stress-strain relationship for granular materials based on the hypothesis of best fit. Int. J. Solids Struct. 34, pp. 4087- 4100, 1997.
- [117] Goddard, J. D.: Continuum modeling of granular assemblies. Physics of Dry Granular media. Eds.: H. J. Herrmann, J. P. Hovi and S. Luding, Kluwer Academic Publishers, Dordrecht, pp. 1-24, 1998.
- [118] S. C. Cowin: A simple theory of instantaneously induced anisotropy. Micro-mechanics of granular materials. Eds.: J. T. Jenkins and M. Satake, Elsevier, Amsterdam, pp. 71-80, 1988.
- [119] Sadd, M. H., Gao, J., Shukla, A.: Numerical analysis of wave propagation through assemblies of elliptical particles. Comput. Geotech. 20 (3/4), 323-344, 1997.

- [120] Goddard, J. D.: Micro-structural origins of continuum stress fields- a brief history and some unresolved issue. In: Dekee, D., Kaloni, P. N. (Eds.) Recent developments in structured continua. Pitman research notes in Mathematics No. 143, Longman. J. Wiley, New York, p. 179.
- [121] Mehrabadi, M. M., Nemat-Nasser, S., Shodja, H. M., Subhash, G.: Some basic theoretical and experimental results on micromechanics of granular flow. In: micromech. Granular Media. Elsevier, Amsterdam, 1988.
- [122] Chang, C. S.: Micromechanical modeling of constitutive relations for granular media. In: Micromech. Granular media. Elsevier, Amsterdam, 1988.
- [123] Thornton, C., Randall, C. W.: Applications of theoretical contact mechanics to solid particle system simulation. In. Micromech. Granular media. Elsevier, Amsterdam, 1988.
- [124] Raphael Blumenfeld: Stress in isostatic granular systems and emergence of force Chains, Physical Review letters, volume 93, Number 10, 2004.
- [125] D. H Troppe and B. C. Burman, Geotechnique 30, 137, 1980.
- [126] Dietrich E. Wolf: Modelling and computer simulation of granular media. K. H. Hoffmann, M. Schreiber, editors, Computational Physics, Springer, pp. 64-95. 1996.
- [127] Mahyar Madadi, Olivier Tsoungui, Marc Lätzel, Stefan Luding: On the fabric tensor of poly-disperse granular materials in 2D, International Journal of Solids and Structures 41, 2563- 2580, 2004.
- [128] R. M. Nedderman, Static and dynamics of granular materials (Cambridge University Press, Cambridge, 1992.
- [129] J.-P. Bouchaud, M. E. Cates and P. Claudin: Stress distribution in Granular media and nonlinear wave equation: J. Phys. I, France 5, 639-656, 1995.
- [130] Atman, A. P. F., Brunet, P., Geng, J., Redydellet, G., Claudin, P., Behringer, R. P. and Clement, E.: From the stress response function (back) to the sand pile dip. Eur. Phys. J. E 17, 93-100.
- [131] Footprints in sand: The response of a granular material to local perturbations. Jufei Geng, D. Howell, E. Longhi, and R. P. Behringer, G. Reydellet, L. Vanel, and E. Clement, and S. Luding, Physical Review Letters 87, 035506, 2001.
- [132] Dan Serero, Guillaume Reydellet, Philippe Claudin, and Eric Clement, Dov Levine: Stress response function of a granular layer: quantitative comparison between experiments and isotropic elasticity. Eur. Phys. J. E 6, 169-179, 2001.

- [133] Junfei Geng, G. Reydellet, E. Clement, R. P. Behringer: Green's function measurements of force transmission in 2D granular materials. *Physica D* 182, 274-303, 2003.
- [134] G. Reydellet and Eric Clement: Green's function probe of a static Granular pilling: *Physical Review Letters*, 86, 3308, 2001.
- [135] Goldenberg, C., Goldhirsch, I.: Force chains, Micro-elasticity, and Macro elasticity. *Phys. Rev. Lett.* 89, 084302, 2002.
- [136] P. Claudin, J.-P. Bouchaud, M. E. Cates, and J. Wittmer: Models of stress fluctuations in granular media. *Phys. Rev. E* 57, (4), pp. 4441, 1998.
- [137] Bouchaud, J.-P., Claudin, P, Levine, D., Otto, M.: Force chain splitting in granular materials: A mechanism for large-scale pseudo-elastic behaviour. *Eur. Phys. J. E* 4, 451-457, 2001.
- [138] J. E. S. Socolar, D. G. Schaeffer, P. Claudin: Directed force chain networks and stress response in static granular materials. *Eur. Phys. J. E* 7, 353-370, 2002.
- [139] Tkachenko, A. V. and Witten, T. A.: Stress propagation through frictionless granular Material. *Phys. Rev. E* 60, 687-696, 1999.
- [140] Landau, L. and Lifshitz, E., *Elasticity Theory*, Pergamon Press, New York, 1986.
- [141] K. L. Johnson, *Contact Dynamics*, Cambridge University Press, Cambridge, England, 1985.

Curriculum Vitae

Personal Details:

Name	Pradip Kumar Roul
Sex	Male
Marital status	Married
Date of birth	01.05.1978
Place of birth	Balasore
Nationality	Indian

Education and Employment:

1990-1993	High Schoolings, Gandibed High School, Orissa, India.
1993-1995	Intermediate of Science (I.Sc.) in Mathematics, Physics, Chemistry Khaira College, Khaira, Orissa, India.
1996-1999	Bachelor of Science (B.Sc.) in Mathematics, Physics, Chemistry U. N. College, Utkal University, Bhubaneswar, India.
1999-2001	Master of Science (M.Sc.) in Applied Mathematics Ravenshaw University, Orissa, India.
2005-2009	Ph.D graduation (DFG scholarship) within the Graduiertenkolleg, "GK 828" Faculty of Mathematics, Otto-von-Guericke-University, Magdeburg, Germany.
Since 01.06.2009	Postdoctoral Research Assistant at the Institute of Numerical Mathematics, Duisburg-Essen University, Duisburg, Germany.

Academic Honours:

- Qualified Graduate Aptitude Test in Engineering (GATE)-2004.
- Qualified Junior Research Fellowship (JRF) in Mathematical Sciences-2005
- Qualified eligibility for Lectureship-National Eligibility Test (NET)-2005.
- German Research Foundation (DFG) Graduiertenkolleg Scholarship-(2005-2008).